Université Louis Pasteur (Strasbourg I)

Thèse

soutenue le : 10 juin 2008
pour l'obtention du titre de

Docteur de l'Université Louis Pasteur
Spécialité : Physique de la matière condensée et des matériaux

par

Samir ABDELOUAHED

Electronic and magnetic properties of Gd based materials beyond the local density approximation

devant le jury

Prof.	Mebarek Alouani	*Directeur de Thèse*
Dr.	Christine Boeglin	*Rapporteur Interne*
Dr.	Andrei Postnikov	*Rapporteur Externe*
Dr.	Leonid Sandratskii	*Rapporteur Externe*

Institut de Physique et Chimie des Matériaux de Strasbourg

Contents

Chapter 1

Résumé

Comprendre les propriétés électroniques, et par conséquent structurales et magnétiques des terres rares est un enjeu majeur en physique de la matière condensée. Le succès des méthodes dites ab-initio basées sur la fonctionnelle de la densité (DFT), à reproduire et expliquer les propriétés physiques des matériaux, reflète leur efficacité et justifie leur utilisation intensive. Ces méthodes permettent en particulier de comprendre la physique des métaux de transition. En effet, les méthodes de calcul de la structure électronique dans l'approximation locale de la densité (LDA) se sont avérées efficaces pour déterminer les propriétés de l'état fondamental, telles que le paramètre de maille, le moment magnétique intrinsèque, ou le couplage magnétique (ferromagnétique ou antiferromagnétique). Par contre, cette approximation a été inadéquate pour décrire la structure électronique des semiconducteurs et des isolants. En effet, les résultats théoriques diffèrent des résultats expérimentaux pour les semiconducteurs et les isolants, puisque les bandes interdites sont sous-estimées de 50 à 100% par rapport aux bandes interdites obtenues à partir des expériences de spectroscopie optique [1]. A titre d'exemple, cette dernière approximation confère au germanium des propriétés métalliques alors qu'il est un semiconducteur. Cet échec est dû au fait que les fortes corrélations électroniques sont mal représentées dans cette approximation.

L'approximation du gradient généralisé (GGA), qui exprime le potentiel d'échange et de corrélation, non seulement en fonction de la densité de charge, mais également en fonction de son gradient, a permis une meilleure représentation de l'interaction d'échange-corrélation. Cette approximation est en général supérieure à la LDA et a permis, entre autre, de bien décrire l'état fondamental magnétique du fer [2]. En effet, la GGA, en accord avec l'expérience, prédisait la structure cubique centrée comme étant la structure crystalline de l'état de base ferromagnétique du fer, alors que la LDA favorisait un réseau cubique à faces centrées (fcc) et un état non-magnétique. Bien que l'approximation GGA ait été souvent meilleure que la LDA, les bandes interdites en général et les isolants de Mott en particulier, restent toujours mal décrits par cette approximation. Il est vrai que la GGA ait permis une meilleure description des systèmes avec différents types de densités électroniques, mais cette approximation prédisait un caractère métallique pour des composés qui se sont avérés expérimentalement isolants.

La sous-estimation des interactions coulombiennes intra-atomiques par les potentiels GGA ou LDA est la cause directe de la défaillance de ces méthodes ab-initio. C'est en s'inspirant du modèle d'Hubbard [3, 4, 5, 6] qu'on aura réussi à représenter l'interaction coulombienne intra-atomique dans le cadre du formalisme de la DFT. Ces nouvelles méthodes sont dites LDA(GGA)+U [7] et doivent leur succès à la bonne description de la structure électronique des isolants de Mott [8, 9, 10, 11]. Désormais, nous disposons d'une

approche qui nous permettra de bien décrire le caractère local et corrélé des matériaux, grâce à la bonne description de l'interaction coulombienne intra-site. L'idée fondatrice de cette méthode consiste à séparer le potentiel électronique en deux parties. Une partie d'électrons délocalisés qu'on peut correctement et facilement décrire avec le potentiel GGA ou LDA, et une partie d'électrons localisés (les électrons d des métaux de transition ou les électrons f des terres rare) pour laquelle l'interaction intra-atomique électron-électron est introduite selon la théorie champ moyen de Hartree-Fock.

Ce n'est pas par hasard que cette méthode ait permis une meilleure compréhension de la physique des systèmes à électrons fortement corrélés, mais grâce à l'efficacité du traitement des électrons. En effet, traiter seulement les électrons délocalisés par un potentiel GGA ou LDA et les électrons localisés par un potentiel LDA(GGA)+U permettrait d'éviter le double comptage des interactions électroniques et de soustraire l'auto-interaction (SI) entre les électrons localisés. Il a été montré que cette dernière auto-interaction contribuait énormément au potentiel total des matéraux à électrons localisés [12]. A ce sujet nous pouvons rappeler que les systèmes à électrons $4f$ tels que les terres rares possèdent aussi la propriété d'électrons localisés ($4f$) bien qu'ils soient métalliques. En effet, les électrons $4f$ des terre rares ont un aspect commun avec les électrons $3d$ des isolants de Mott, sauf que dans le cas de ces isolants c'est l'oxygène qui renforce la localité des électrons $3d$, alors que dans le cas des terres rares c'est une localité intrinsèque des orbitales f.

Nous pouvons par conséquent nous attendre à ce que le traitement des électrons $4f$ par la méthode LDA(GGA)+U (de la même manière que les électrons $3d$ dans les isolants) nous permette d'aborder correctement la structure électronique des terres rares. Si on fait appel au schéma de Stoner [13], concernant le magnétisme, nous pouvons facilement comprendre que c'est la localité des électrons $4f$ qui confère aux terres rares la propriété des matériaux fortement magnétiques. C'est par exemple le cas du gadolinium (Gd) massif pour lequel on a un moment magnétique de l'ordre de 7 μ_B grâce à la couche $4f$ qui est à moitié remplie. Ces matériaux peuvent par conséquent être de bons candidats pour des applications industrielles telles que les aimants permanents ou les systèmes d'enregistrements magnétiques. Cependant, la compréhension des mécanismes qui gèrent la structure électronique de ce type de matériaux, reste loin d'être acquise. Même dans l'état pur, les matériaux magnétiques $4f$ sont plus difficiles à aborder que les matériaux magnétiques $3d$ des métaux de transition (Fe,Co,Ni). C'est la nature des électrons $4f$ fortement localisés et corrélés qui rend ces matériaux difficiles à décrire à l'aide des méthodes de calcul de la structure électronique.

La complexité de ce type de matériaux réside dans la coexistence d'électrons fortement localisés et d'électrons non localisés. Les calculs de structure électronique effectués par Singh [14] avaient montré que, bien que les orbitales $4f$ soient suffisamment localisées, elles contribuent à l'établissement des liaisons chimiques. Grâce à ses propriétés magnétiques intéressantes le Gd est le plus étudié de nos jours. De nombreuses questions font toujours le sujet d'un grand débat et ne cessent d'interpeller la communauté scientifique. Les bandes $4f$ s'adaptent-elles avec les autres bandes, vont-elles s'hybrider avec, ou conservent-elles leur caractère local? (voir papier I ainsi que les papiers cités). Qu'en est-il de l'anisotropie magnétique, ressemble-t-elle à celle d'un métal de transition? S'agit-il d'un magnétisme de Stoner pour lequel chauffer le système permettrait de *libérer* les moments magnétiques du couplage fort qui les maintient parallèles [15, 16] ou plutôt d'un magnétisme de Heisenberg [17] où le moment magnétique porté par chaque site *survivra* même à des températures plus grandes? L'implication de ces différents aspects de la structure électronique dans la représentation du magnétisme du Gd a fait de ce mag-

nétisme, le plus étudié des terres rares.

C'est dans ce contexte que le projet de ma thèse de doctorat avait été entrepris. Pendent ces dernières décennies, les méthodes de calcul de la structure électronique sont de plus en plus utilisées, surtout pour étudier les matériaux magnétiques. La méthode *ab-initio* que nous avons utilisée tout au long de notre étude repose sur la technique de linéarisation des ondes planes augmentées à potentiel total (FLAPW) [18, 19]. Cette base de fonctions d'ondes est parmi les plus précises. Contrairement aux autres bases utilisant l'approximation des sphères atomiques (ASA) où le potentiel est approximé par une constante dans la région inter-atomique, la méthode FLAPW calcule correctement le potentiel dans la région inter- et intra-atomique. Le cristal est divisé en deux régions, une région dite muffin-tin et une région interstitielle. A chaque itération du cycle self-consistent la densité de charge et le potentiel sont calculés de la même manière dans ces deux régions. Le potentiel ainsi calculé est sensible à la moindre variation de la densité de charge et devrait donc proprement décrire la physique sous-jacente. C'est ce qui a motivé notre utilisation de cette méthode, pour aborder la structure électronique du gadolinium ainsi que certains de ses composés.

Malgré la grande température de Curie du gadolinium (de l'ordre de 295 K), l'importance de la corrélation électronique sur sa stabilité et sur son état magnétique a été le sujet d'une controverse durant la dernière décennie. Étant donné les progrès qu'ont connu les techniques des rayons X telles que le dichroïsme circulaire magnétique des rayons X (XMCD), et les nombreuses investigations expérimentales qui ont été menées pour sonder le magnétisme des différents matériaux, il nous a paru utile d'implémenter le calcul du XMCD dans le code ab-initio de la méthode FLAPW. L'un des points forts de cette technique est que la section efficace d'absorption qu'on mesure pour calculer le XMCD[1], possède deux propriétés sélectives :

- la sélectivité de l'atome sondé : les seuils d'absorption ont des énergies qui sont caractéristiques pour chaque élément,

- la sélectivité des états finaux : grâce aux règles de sélection dipolaires, des états finaux avec des symétries différentes peuvent être sondés en choisissant l'état initial.

Notre démarche consisterait, d'une part à raffiner les calculs des spectres de dichroïsme magnétique circulaire, et en particulier à obtenir un accord quantitatif entre les spectres théoriques et les spectres expérimentaux, et d'autre part à comprendre le rôle des électrons non localisés dans le magnétisme, dont on sait qu'ils sont à l'origine des interactions à longue portée. Par exemple, l'ordre magnétique dans les aimants permanents les plus puissants connus à ce jour ($SmCo_5$, $Nd_2Fe_{14}B$) est dû à l'interaction des électrons $5d$ de la terre-rare avec les électrons $3d$ du métal de transition.

Dans un premier temps, nous avons cherché à améliorer l'approche théorique utilisée pour calculer les spectres XMCD. En effet il s'agit de comprendre pourquoi les rapports intégrés de branchement restent sous-estimés par rapport à l'expérience dans les calculs ab initio. Cette approche s'est appuyée sur le traitement des corrélations dans l'approximation GGA+U.

[1] Le XMCD est la différence, pour un matériau magnétique, entre l'absorption des rayons X polarisés circulairement à gauche et à droite.

– Nous avons utilisé les énergies GGA+U à la place des énergies LDA pour calculer les spectres XMCD dans une approche où l'on ne tient pas compte de l'attraction entre le trou de coeur et l'électron promu dans un état vide.

– Nous avons généralisé nos calculs aux composés de terres rares tels que le gadolinium, le GdN et le $GdFe_2$. Pour ce dernier par exemple, les propriétés magnétiques résultent d'une forte hybridation des états $5d$ de la terre rare et des états $3d$ du métal de transition ainsi que des états localisés $4f$ de la terre rare. Nous avons alors, pour des composés de la famille terre rare - métaux de transition, calculé le signal de dichroïsme aux seuils $L_{2,3}$ de la terre rare (transitions dipolaires électriques $2p_{1/2,3/2} \longrightarrow 5d$) et confronté les spectres théoriques aux spectres expérimentaux disponibles. En effet, les électrons $4f$ jouent un rôle prépondérant dans l'interprétation du dichroïsme aux seuils $L_{2,3}$ de la terre rare. En absence de moment magnétique d'origine $4f$, cas du $LaFe_2$ et $LuFe_2$ (couche $4f$ respectivement vide ou pleine), la bande $5d$ est polarisée en spin par les électrons $3d$ du fer et par conséquent la terre rare développe un magnétisme induit. Le signe du spectre de dichroïsme $L_{2,3}$ montre que le moment de spin des états $5d$ est antiparallèle au moment magnétique des états $3d$ du fer en accord avec le calcul de structure de bandes. Par contre, lorsque les états $4f$ sont partiellement remplis, le spectre de dichroïsme $L_{2,3}$ est beaucoup plus compliqué car dans ce cas les états $5d$ interagissent également par échange intra-atomique avec les électrons $4f$. On doit éventuellement tenir compte des transitions quadrupolaires électriques ($2p \longrightarrow 4f$) pour expliquer les détails des spectres expérimentaux.

Nous ne pouvons pas nous permettre de parler de la spectroscopie XMCD sans évoquer ses règles de somme. Grâce à ces règles, il est devenu possible d'extraire directement les moments de spin et orbital des spectres XMCD. C'est ce qui fait l'originalité de cette technique, comparée aux autres. En effet, il existe plusieurs techniques pour mesurer les propriétés magnétiques des matériaux. La plupart d'entre elles sont sensibles à l'aimantation *totale* et ne peuvent pas différencier entre les contributions des différents atomes d'un alliage ou d'une multicouche, et leurs moments de spin et d'orbite. Pour expliquer les spectres expérimentaux, nous avons confronté nos résultats de calcul XMCD aux résultats expérimentaux (voir Fig. 1.1). Ceux concernant le gadolinium ont révélé le rôle important des corrélations électroniques provenant des orbitales f fortement localisées, et l'adéquation de la méthode GGA+U pour décrire la structure électronique. Les résultats obtenus par cette méthode sont en bon accord avec les résultats expérimentaux, tels que la photoémission et la photoémission inverse (voir Fig. 1.2) et l'ordre magnétique. Nos spectres XMCD et les moments calculés à partir de la règle de somme aux seuils $L_{2,3}$ ou $M_{4,5}$ sont également conformes à l'expérience (voir papier I).

Cet accord approuve ainsi l'approximation dipolaire que nous avons adoptée dans le cadre du formalisme XMCD, et montre le caractère local des électrons f à travers l'accord des moments calculés à partir du calcul auto-ccohérent et ceux des règles de somme. Ces résultats devraient stimuler de futures recherches théoriques dans le cadre de la méthode GGA+U, pour les autres terres rares.

Pendant longtemps, le rôle des états $4f$ dans la détermination de la nature de la structure électronique du gadolinium était mal compris (voir papier I). En utilisant la méthode FLAPW nous avons montré que la méthode LDA(GGA)+U permet une meilleure compréhension de la structure électronique du Gd, ce qui pourrait encourager l'étude de la structure électronique des autres terres rares. Les calculs que nous avons effectués en FLAPW nous ont permis de montrer que le magnétisme du Gd est proprement décrit

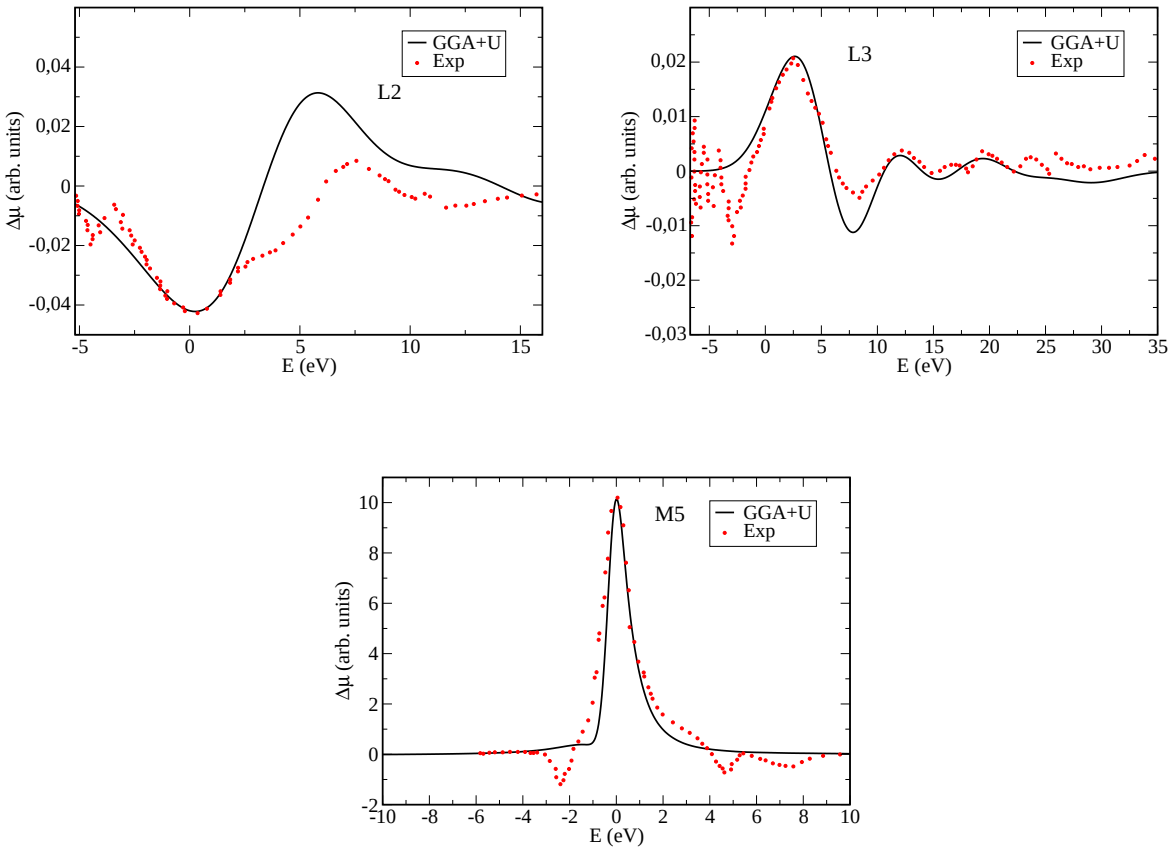

Figure 1.1: *Les spectres XMCD calculés (en courbe noire continue) comparés aux spectres expérimentaux (en cercles rouge) pour le Gd massif. En haut à gauche le seuil L_2, à droite le seuil L_3, et en bas le seuil M_5.*

dans le cas où l'on prend en compte l'interaction intra-atomique des électrons $4f$ fortement localisés, en utilisant la méthode LDA(GGA)+U.

L'émergence de la spintronique, et l'intérêt qu'a suscité la communauté scientifique à l'égard des semiconducteurs magnétiques dilués (DMS) et particulièrement à l'égard des demi-métaux – faisant de ces derniers des candidats potentiels pour l'injection de spin – nous a tout naturellement amené à étudier le composé GdN.

Contrairement aux DMS classiques, où le magnétisme est dû aux électrons iténirants d, le magnétisme du GdN est dû aux électrons localisés f et aux orbitales délocalisées $5d$. De plus, le composé GdN, suivant la nature du substrat sur lequel on le fait croître, couvre une grande gamme de propriétés électroniques, allant d'un métal à un semi-conducteur en passant par un demi-métal. La compréhension de ce type de systèmes représente ainsi un enjeu majeur pour la spintronique. Afin de souligner l'importance de la structure électronique et magnétique du GdN, nous avons effectué des calculs ab-initio en utilisant la méthode GGA+U dans le cadre de la méthode FLAPW. Les calculs que nous avons faits à cet égard ont montré la forte hybridation des orbitales p du nitrogène N avec les orbitales d du Gd. Pour voir l'effet de la présence du N sur les orbitales d du Gd, nous avons calculé les spectres XMCD aux seuils $L_{2,3}$ du Gd dans le composé GdN (voir Fig. 1.3).

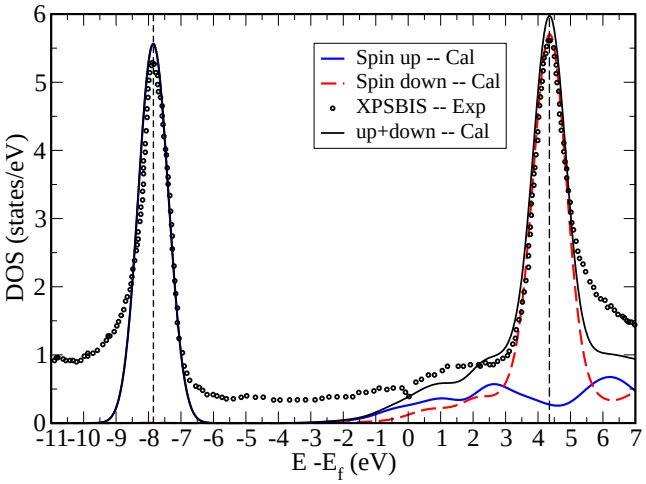

Figure 1.2: *Densité d'états totale (en courbe noire) comparée aux expériences de photoémission et photoémission inverse pour le Gd massif. Les spins majoritaires sont en bleu et les spins minoritaires sont en rouge.*

Nous avons également confirmé que la structure électronique du GdN est celle d'un demi-métal pour le paramètre de réseau expérimental. Sous la compression ou l'extension du réseau cristallin, due à la présence d'un substrat, la structure électronique est plutôt celle d'un semi-métal ou d'un semiconducteur. Sous pression hydrostatique, nos calculs prédisent également la possibilité d'une transition de phase structurale de la phase rock-salt vers une phase wurtzite (voir papier II).

Afin d'aborder plus en détails le magnétisme de ces matériaux, nous nous sommes intéressés à l'énergie d'anisotropie magnétocrystalline (MAE). En utilisant le théorème de force[2], nous avons effectué des calculs pour différentes directions de l'aimantation. Ces calculs montrent que cette énergie est de l'ordre de quelques micro électronvolts et que l'axe d'aimantation facile pour le Gd est le (0001) pour le paramètre de maille expérimental. Les calculs de la MAE, effectués en utilisant les différentes méthodes de traitement des électrons $4f$, montrent clairement que la méthode GGA+U est la plus adéquate pour représenter l'énergie d'anisotropie magnétique du Gd (voir Fig. 5).

Pour simuler l'effet de la présence d'un autre élément non-magnétique (N) tel que le composé GdN, ou d'un élément magnétique (Fe) tel que le composé $GdFe_2$ sur l'anisotropie du Gd, nous avons procédé comme pour le calcul de l'anisotropie magnétique du gadolinium. Le calcul montre que trois axes symétriquement équivalents : (100), (010), et (001) sont les axes de facile aimantation pour le GdN et le $GdFe_2$ (voir papier III). Ainsi, même

[2]Ce théorème stipule que l'anisotropie magnétique peut être calculée en supposant que le couplage spin-orbite (SOC) est une perturbation dans l'Hamiltonien total. C'est surtout par rapport au temps de calcul que ce théorème est utile. Si le terme du SOC est de petite contribution, nous n'avons pas besoin de converger le calcul self-consistent pour calculer ses effets sur la structure électronique. Une seule itération serait suffisante pour introduire cette contribution pour différentes directions de l'aimantation tout en gardant le potentiel cristallin gelé.

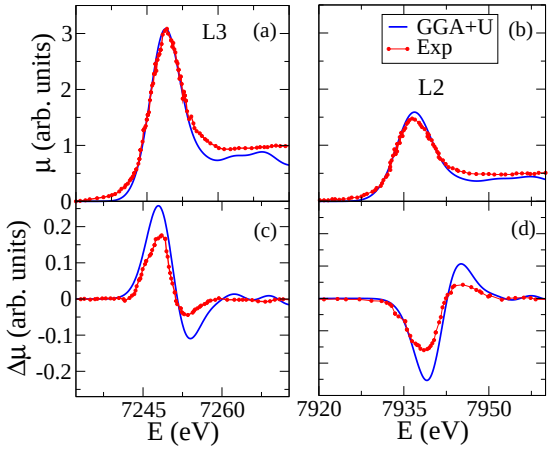

Figure 1.3: *Les spectres d'absorption et d'XMCD calculés (en courbe bleue continue) comparés aux spectres expérimentaux (en cercles rouges) pour les atomes Gd dans le GdN. Le panneau à groite; en haut (a) le spectre d'absorption au seuil L_3 et en bas (c) le spectre XMCD correspondant. Le panneau à groite; en haut (b) le spectre d'absorption au seuil L_2 et en bas (d) le spectre XMCD correspondant.*

dans les systèmes cubiques c'est le magnétisme du Gd qui gère l'anisotropie magnétique du système en question.

Le travail effectué dans le cadre de cette thèse nous a permis d'étudier la structure électronique, magnétique et structurale des matériaux constitués d'électrons $4f$. Les résultats de cette étude ont montré le rôle important de la présence des orbitales f parmi les bandes de valences du gadolinium métallique. Malgré leur forte localisation, cette présence se manifeste par une forte hybridation avec les orbitales $5d$. La seule méthode qui nous a permis de bien décrire ce type de systèmes, tout en tenant compte de l'interaction coulombienne intra-atomique des électrons $4f$, est la méthode dite LDA(GGA)+U. En effet, cette méthode semble la plus adaptée pour décrire des terres rares dont la structure électronique est dominée par les électrons $4f$. Le bon accord entre les spectres XMCD calculés et l'expérience ainsi que les moments calculés à partir de ces spectres et ceux de l'expérience, justifie indirectement l'approximation dipolaire électrique et le caractère presque atomique des orbitales sondées. La spectroscopie XMCD est par conséquent un moyen très efficace pour étudier le magnétisme des électrons localisés.

Même si notre étude avait clairement mis en évidence l'adéquation et l'efficacité de la méthode LDA(GGA)+U, cette méthode ne nous permettrait pas d'aborder l'aspect physique de certains phénomènes dynamiques. Dans les spectres XMCD calculés aux seuils $M_{4,5}$ du Gd par exemple (Fig. 6), nous ne retrouvons pas les structures expérimentales qui apparaissent avant et après le pic principal. Ces structures proviendraient de l'effet des multiplets et des processus dynamiques de l'interaction photoélectron-trou. Selon la théorie du champ moyen dynamique (DMFT) il serait possible de comprendre des scénarios de ce genre. En fait, la dynamique engendrée pendant les absorptions X serait essentiellement due à l'interaction électron-trou. Etant donné que les niveaux énergétiques initiaux sont des niveaux de coeur profonds en énergie, on peut s'attendre à ce que les rayons X créent un trou avant qu'un électron déjà excité puisse relaxer. Dans le cadre de la méthode DMFT (voir Ref. [20] et les références qui y sont citées) on peut

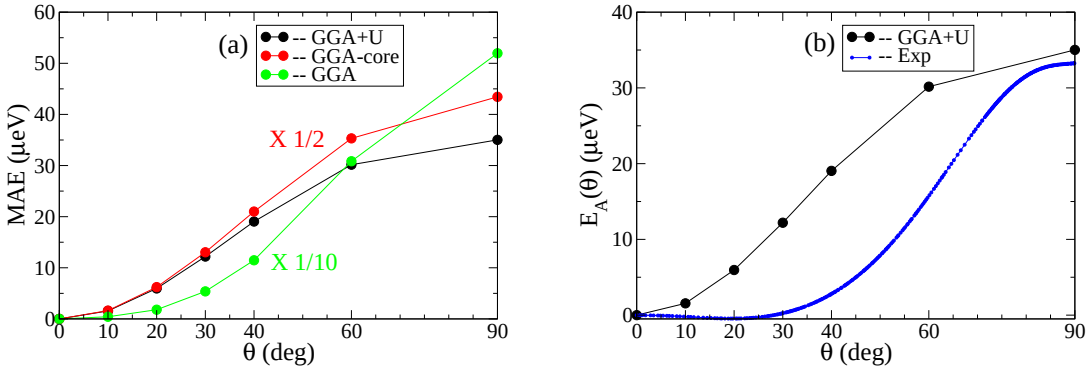

Figure 1.4: *L'énergie d'anisotropie magnétique du Gd définie comme* $MAE \equiv E_A(\theta) - E_A(0°)$. *La figure (a) représente la MAE calculée en traitant les électrons 4f de trois manières différentes; en noir le calcul GGA+U où l'interaction coulombienne U est prise en compte pour les électrons 4f qui font partie des électrons de conduction; en rouge le calcul GGA-core où les électrons 4f sont considérés comme des électrons du coeur, et en vert le calcul GGA standard où les électrons 4f sont traités comme des électrons de conduction. La figure (b) représente le calcul GGA+U (la courbe en noir est la même que celle en (a)) comparé à l'expérience (courbe en bleu).*

traiter l'atome de Gd excité comme une impureté. La dynamique de cette impureté serait donc considérée comme son interaction moyenne à chaque instant, avec un bain formé par le reste des atomes. Il serait donc important de faire des calculs XMCD dans le cadre de cette méthode pour *suivre* l'évolution des transitions pendant l'absorption X.

En perspective, il serait important d'étudier un autre aspect du magnétisme; le magnétisme non-colinéaire (ou les ondes de spin). Ce qui permettrait de calculer la température de Curie qui est une grandeur physique importante. Le magnétisme non-colinéaire est une conséquence directe de la compétition entre le couplage spin-orbite et l'interaction d'échange. La pression ou le dopage change la configuration magnétique et la température de Curie. La continuation de ce travail sera par conséquent de doper GdN, soit avec du manganèse soit avec de l'hydrogène, afin d'augmenter fortement sa température de Curie, qui, dans l'état massif est de l'ordre de 60 K. Dans ce contexte, il est aussi envisagé d'étudier l'effet du dopage en hydrogène sur la température de Curie, des composés de terres rares $TRFe_2$ et $TRMn_2$.

Remerciements

Ce manuscrit est le résultat de mes dernières années d'étude passées à l'ULP de Strasbourg. Je tiens à remercier mon père, sans qui je ne serais jamais venu en France, de m'avoir toujours soutenu, de m'avoir pris en charge pendant ma première année à Grenoble et de m'avoir encouragé tout au long de mon parcours universitaire. Un grand merci à ma mère d'avoir toujours eu confiance en moi et d'avoir été présente tout au long de mon éducation et surtout pendant mon parcours universitaire en Algérie. Je vous embrasse papi et mami.

Merci tout d'abord à mon directeur de thèse, Prof. Mebarek Alouani, pour avoir orienté ma recherche pendant ces trois années avec beaucoup de présence et de disponibilité et pour les conversations fructueuses que j'ai eues avec lui.

Merci aux membres du jury Dr. Christine Boeglin, Dr. Andrei Postnikov, et Dr. Leonid Sandratskii pour le temps qu'ils ont consacré à ma thèse.

Merci au Prof. S. Blügel et au Dr. G. Bihlmayer de m'avoir accordé beaucoup de leur temps pour m'initier à l'utilisation du code Fleur pendant mon séjour à Jülich (Allemagne).

Merci également au Dr. N. Baadji pour les nombreuses discussions que j'ai eues avec lui sur la physique de l'XMCD.

Je souhaite également remercier Dr. Leonid Sandratskii pour les discussions stimulantes sur le magnétisme non-colinéaire ainsi que sur le calcul de la température de Curie pendant mon séjour à Halle (Allemagne).

Je souhaite saluer également Bertrand Leriche, Madjid Abes, Gabriel Vasseur, Feng Xiaobing, Ilyas Z. Ismagilov, Mohammed Haroun, Bouzid Sekiou, Nabil Najjari, Lamjed Debbichi, Menad Hamdaoui, Lyamine Mokhtari, Leila Messad, Madjid Boussendel, Abdelhamid Bouaine, Makhlouf Kharoubi, Faical Azzouzi, et tous mes amis et collègues.

Une pensée bien affectueuse à ma femme, à celle qui s'est dévouée sans cesse et qui m'a toujours soutenue dans mes décisions et m'a toujours aidé de son mieux, sans oublier mon brave fils Nasr Eddine, que le bon dieu le garde et le bénisse.

Je profite de ces remerciements pour exprimer mon affection pour mes soeurs et mes frères, surtout Mohammed et Zineb et sans oublier toute la famille en Algérie. Le temps passé auprès de vous est toujours trop court!.

acknowledgments

This thesis is the result of my studies at the University Louis Pasteur and the Institute of Physics and Chemistry of Materials of Strasbourg. I would like to thank my father without whom I would have never attended the French University. Thanks a lot father for supporting me throughout my University studies. Sincere thanks to my beloved mother. Thank you mother for your devotion and especially during my post-graduate studies in Algeria.

I am indebted to Prof. Mebarek Alouani for supervising my thesis and many helpful discussions I had with him on the theory of magnetism. Thank you for being available, for your confidence on me and for all you did for my Phd thesis.

I also thank the member of the jury, Dr. Christine Boeglin, Dr. Andrei Postnikov, and Dr. Leonid Sandratskii for the time they spent reading my thesis manuscript.

I want to thank Prof. S. Blügel and Dr. G. Bihlmayer for inviting me to the theory 1 group of Jülich (Germany), for spending time teaching me how to use the Fleur code.

In this respect, I am also grateful to Dr. M. Lezaïc for several discussions I shared with here concerning the non-colinear magnetism implementation within the Fleur code.

To Dr. N. Baadji, I want to say thank you for the discussions on the XMCD theory.

I also thank Leonid Sandratskii for stimulating discussions on the non-colinear magnetism and on the Curie temperature calculations during my stay in Halle (Germany).

I would like to greet Bertrand Leriche, Madjid Abes, Gabriel Vasseur, Feng Xiaobing, Ilyas Z. Ismagilov, Mohammed Haroun, Bouzid Sekiou, Nabil Najjari, Lamjed Debbichi, Menad Hamdaoui, Lyamine Mokhtari, Leila Messad, Madjid Boussendel, Abdelhamid Bouaine, Makhlouf Kharoubi, Faical Azzouzi, and all friends and colleages.

I am feeling grateful to my affectionate wife, who has been encouraging me ceaselessly during my Phd thesis study, and to my beloved six month old boy Nasr Eddine.

I would not forget of course my family in Algeria. I would like to say to my brother's and sisters: Dalila, Salah, Aldelbaki, and Ouided, I miss you all.

"L'envie de pénétrer les secrets est profondément ancrée dans l'âme humaine, même le moins curieux des esprits s'enflamme à l'idée de détenir une information interdite à d'autres." John CHADWICK

Chapter 2

Introduction

In the last few decades there have been a considerable improvements in designing and manufacturing electronic devices, especially those based on the spin degrees of freedom, labeled nowadays spintronic(s) devises. It is the functionnalization of the electronic spin degrees of freedom together with the charge degrees of freedom which led to such interesting electronic devices. In this respect, the 2007 Nobel prize in physics is awarded to Fert and Grünberg for their discovery of the giant magnetoresistance. Their discovery has given rise to many nanoelectronic devises of great usefulness to the computer industry. Understanding magnetic properties of materials is therefore of great interest. In particular, mastering the spin degrees of freedom might be beneficial at the nanoscale, increased data processing speed, decreased electric power consumption and increased integration densities [21].
Nowadays mostly $3d$ magnetic materials are studied for such interesting applications while only a few attention is paid to rare earth magnetic materials. Due to their $4f$ localized orbitals rare earth materials exhibit a strong magnetism. These materials might be, therefore, promising candidates for the above mentioned applications. Because of its half-filled $4f$ shell, gadolinium (Gd) is certainly the most important among these materials. With the evolution of the computational resources, modern electronic structure methods are going to be more and more used for studying magnetic materials.
Since the pioneering work of Dimmock and Freeman [22] where the Gd electronic structure has been calculated using the core model for the treatment of the $4f$ electrons, there has been a few more band-structure calculations for Gd. In this simple model, while the $4f$ bands have been successfully *removed* from the conduction band at the vicinity of the Fermi level, the hybridization of the $4f$ states with the others states was not accounted for. Some years later, the self-consistent calculations of Sticht and Kubler [23] have shown that the standard LDA potential leads to a smaller lattice parameter because of the spurious presence of the $4f$ minority states close to the Fermi level. Later, Temmerman and Sterne [24] have found a very large sensitivity to the treatment of the extended $5p$ core states as semi-core states. Afterwords, Singh [14] has shown that the LDA does not provide a fully satisfactory description of Gd. This reflects particularly the complexity of the Gd electronic structure due to the presence of $4f$ electrons. The conduction electrons of Gd consist of three kind of electrons: the $4f$ strongly localized electrons, the $5p$ and $5s$ semicore electrons, and the itinerant $3d$ and $6s$ electrons.
In addition, it is unclear whether the Gd magnetism is that of a typical Stoner-like magnetism [15, 16] or that of a Heisenberg-like magnetism [17]. It turns out that its electronic properties and therefore its magnetic properties are far from being fully understood, and a further theoretical investigations are therefore called for.

The failure of the LDA for the description of localized electron systems was already proved, i.e, the so-called Mott insulators were found to be metallic within the LDA calculations. Indeed, unlike in pure $3d$ transition metals, the Mott insulators $3d$ electrons, such as, NiO, are localized because of the presence of neighboring oxygen. This means that an *extra*-Coulomb interaction between these electrons should take place. It is this interaction which is missing in the LDA scheme and one should therefore, come up with a method which allows an appropriate representation of those localized electrons.
The LDA(GGA)+U method [7] which is a generalization of the Hubbard model [3, 4, 5, 6] was found to be adequate for the description of the electronic structure of localized electron systems, where the U is the intra-atomic Coulomb interaction. Within this method, the electronic structure of the Mott insulators was successfully accounted for [8, 9, 10, 11] by correctly describing the $3d$ electrons. Henceforth, one is left with a method incorporating the strong Coulomb intra-atomic interaction for localized electrons. The LDA(GGA)+U method is therefore, expected to be efficient for the study of $4f$ strongly localized systems electronic structure such as Gd and Gd compounds.
The appreciable progress in spectroscopic techniques such as those of the x-ray magnetic circular dichroism (XMCD), and the several investigations this spectroscopy had led to, have motivated our implementation of the XMCD within the ab-initio Fleur code [25] using the full potential linear augmented plane wave method (FLAPW) [18, 19]. In fact, XMCD spectra have two useful properties for magnetic materials characterization. The first one is that of the atomic species and orbital selectivity, i.e., each chemical element and each core orbital has its own absorption edge(s), the second one is that of the final shell or of the final states selectivity, i.e., the transitions involved during the x-ray absorption are selected according to the specific selection rules. Since the initial states are chosen, only the transitions for which the final states satisfy the dipolar selection rules may happen. In this respect, we should remind the powerful advantage of the XMCD sum-rules. Nowadays, there are many techniques for magnetic properties measurements. Most of them are sensitive to the *total* magnetization and do not distinguish between the different atomic contributions of alloys, or between their spin magnetic and orbital moments. With the derivation of the sum rules by Thole and cowerkers [26, 27], XMCD spectroscopy became the most efficient technique for studying magnetic materials. The sum rules allow the extraction of both the spin and orbital magnetic moments from the absorption spectra. In order to extract the spin and orbital moments from the x-ray absorption spectra we have implemented these sum rules.
In this thesis, we have approached the electronic structure of Gd in a first step. The calculations are carried out with the FLAPW, one of the most precise density functional methods for multicomponent materials, open structures and surfaces. We have focused on the GGA+U treatment of the electronic and magnetic structure of Gd (see paper I), comparing the calculated density of states to the the experimental photoemission and inverse photoemission spectra (XPS and BIS) the GGA+U is found to be the most appropriate for treating the $4f$ Gd electrons. We have investigated the bulk properties, and calculated the XMCD spectra at the $L_{2,3}$ and $M_{4,5}$ edges within the dipolar approximation. The spin-orbit interaction is included in a second-variation scheme according to the scalar relativistic approximation. The agreement of the calculated spectra with those of the experiment is the indication of the relevance of the XMCD formalism within the one-electron picture.
The emergence of spintronics, and the great interest which aroused the scientific community towards magnetic diluted semiconductors (DMS), and particularly half-metals because of their applications for spin injections, have motivated us to study the GdN

compound. Unlike the classical DMS, where the magnetism is due to $3d$ electrons, GdN compound proposes a semi-itinerant magnetism due to the f electrons. Furthermore, GdN, following the nature of the substrate on which it is grown, covers a big range of electronic properties, half metal, semimetal, or semiconductor. The understanding of such systems properties is thus of interest to spintronics.
Within the same FLAPW computational framework we have carried out first-principles calculations of the GdN electronic, magnetic, and structural properties (see paper II). The corresponding results show that the ground state electronic structure of GdN is that of a half metal. Under hydrostatic pressure the half metal rocksalt (Nacl structure) transforms into a wurtzite semiconductor.
The last part of our computational investigations is devoted to the magnetic anisotropy aspect of the Gd and its compounds GdN and $GdFe_2$. The rotation or the deviation of the magnetization in a large variety of materials, e.g., permanent magnetic materials, ultrathin films, low-dimensional magnetic nanostructures or atomic chain, influences the magnetic and therefore the electronic properties of these materials. The energy required to rotate the magnetization of a magnetic crystal is defined as the magnetocrystalline anisotropy energy (MAE).
Using the force theorem, we have calculated the MAE of Gd, GdN, and $GdFe_2$ for different directions of the magnetization (see paper III). Indeed, owing to the nil spin-orbit interaction of the $4f$ half filled shell, the force theorem is expected to be efficient for Gd and Gd compounds MAE calculations. This theorem allows a considerable computational effort gain since the spin-orbit coupling could be calculated only for one selfconsistent iteration.
Once again, the GGA+U method is found to be the most adequate approach for the force theorem calculations of the Gd MAE. The GGA and GGA-core model treatment of the $4f$ states have led to a wrong Gd MAE. It turns out that the electronic properties and the magnetic properties of $4f$ systems are tightly related, and the $4f$ electrons are of crucial role in the rare earth magnetic anisotropy.
Though the Gd MAE is found to be too similar to that of a typical $3d$ transition metal like hcp Co, the GdN and $GdFe_2$ cubic crystals MAEs are found to be different from that of a pure $3d$ cubic material like fcc Ni. In these compounds we have found that the magnetization lies along the (001) direction while it is found to lie along the (111) direction for Ni.
This thesis is structured as follows. The founder ideas and the formulation of the DFT are presented in Chapter 3. The main features of the FLAPW method (as implemented in the Fleur code) are described in Chapter 4. Emphasis is put on the description of the spin-orbit coupling relativistic effect within the FLAPW method, a brief derivation of the force theorem as well as a description for its application to the MAE calculations is provided in Chapter 5. Chapter 6 is devoted to another consequence of the spin-orbit coupling, that of the XMCD. A quit rich bibliography is supplied in preamble, and a special attention is given to the description and the derivation of the XMCD formalism as a magneto-optical effect. Chapter 7 is that of the main results (paper I, II, and III). Finally, in Chapter 8, concluding remarks and perspectives for the $4f$ magnetism theoretical investigations and applications are presented.

Chapter 3

Density Functional Theory

Calculating electronic and magnetic properties of solids is not trivial task even when solids are in their ground state. In solid state, condensed matter is composed of atoms held together by chemical bonds insured by the valence electrons. Involving so many particles gives rise to a complex many-body problem. One of the early proposed model to deal with such complexity is the Born-Oppenheimer approximation.

3.1 The Born-Oppenheimer approximation

The Born-Oppenheimer approximation [28] consists of dividing the total solid-state problem into two parts: The motion of the electrons in a stationary lattice and that of the ions in a uniform space charge of electrons. The total Hamiltonian H which represents the total energy of a *realistic* system can be written as:

$$H = H_{el} + H_{ion} + H_{el-ion} + H_{ex}, \tag{3.1}$$

where H_{el}, H_{ion}, and H_{el-ion} are respectively the electrons, the ions, and the electrons-ions interactions Hamiltonian. These terms consist of, the kinetic energy of all electrons, all ions, and the energy associated with all the interactions between theses particles. The last term represents any interactions with external fields. The Born-Oppenheimer approximation allows us to rewrite separately the electron and ion components as follows:

$$H_{el} = -\sum_{k} \frac{\hbar^2}{2m}\nabla_k^2 + \frac{1}{8\pi\epsilon_0}\sum_{k,k'} \frac{e^2}{|\mathbf{r}_k - \mathbf{r}'_k|} + H_{+}. \tag{3.2}$$

$$H_{ion} = -\sum_{i} \frac{\hbar^2}{2M_i}\nabla_i^2 + \frac{1}{2}\sum_{i,i'} V_{ion}(\mathbf{R}_i - \mathbf{R}'_i) + H_{-}. \tag{3.3}$$

The Hamiltonian equation (3.3) is the basis for the study of lattice dynamics and ion-ion interactions (phonons). The first terms in (3.2) and (3.3) are the kinetic energies, the second terms are those of the Coulomb interactions between the charges of each kind, and H_+ and H_- represent the interaction of the electrons (ions) with the average charge of the ions ρ^+ (the average charge of the electrons ρ^-). This approximation is based on the argument that electrons and ions have very different masses (the electron-ion inertia ratio is about 10^{-3}). The ions can respond only slowly to a change in the electron configuration, while the electrons respond adiabatically to a change in the positions of the ions and as far as the motion of the electrons is concerned, it is only the instantaneous configuration

of the ions which is of interest. In the absence of an external field one can therefore adopt for the electrons a Schrödinger equation of the form:

$$H_{el}\Psi = E_{el}\Psi, \tag{3.4}$$

where the wave function $\Psi = \Psi(\mathbf{r}_1, \dots \mathbf{r}_N)$ depends on the coordinates of the N electrons[1]. However, since the Hamiltonian is the observable accounting for the measurable total energy, according to quantum mechanic principles, the eigenfunction Ψ have to be written as an expansion in terms of a complete set of wave functions, i.e., this is the case for example for the configuration interaction (CI) method where the ground-state wave function is a linear combination of Slater-wave functions. The Hartree-Fock mean field approximation have offered a simpler approach to handle the N electrons problem.

3.2 The Hartree-Foch approximation

We focus now on the motion of the electrons, as described by (3.2). We consider an *electron gas* which is embedded in a homogeneous, positively charged medium (jellium medium) or in a rigid lattice of positively charged ions. Even with a jellium medium this problem is very difficult to solve because of the complexity of the electron-electron interaction. In the absence of this interaction, the many-body problem would decouple into one-body problems which describe the motion of an electron in an effective potential (*the one-electron approximation*). In this case the Hamiltonian (3.2) becomes:

$$H = -\sum_k \frac{\hbar^2}{2m}\nabla_k^2 + \sum_k V(\mathbf{r}_k). \tag{3.5}$$

Here we have expressed the H_+ Hamiltonian of equation (3.2) as the total electron-ion potential energy $\sum_k V(\mathbf{r}_k)$ with $V(\mathbf{r}_k)$=$\sum_i V(\mathbf{r}_k - \mathbf{R}_i)$ the interaction between one electron and all the other atoms seen as fixed sources of potential. The wave function of the Schrödinger equation $\sum_k H_k\phi = E\phi$ could be written as the product of individual wave functions:

$$\phi(\mathbf{r}_1 \dots \mathbf{r}_N) = \varphi_1(\mathbf{r}_1)\varphi_2(\mathbf{r}_2)\dots\varphi(\mathbf{r}_N), \tag{3.6}$$

with $E = \sum_k E_k$. The full Schrödinger equation reduces to one-electron Schrödinger equations: $H_k\varphi_k(\mathbf{r}_k) = E_k\varphi_k(\mathbf{r}_k)$. If we take into account the electron-electron interaction the Hamiltonian (3.5) becomes:

$$H = -\sum_k \frac{\hbar^2}{2m}\nabla_k^2 + \sum_k V(\mathbf{r}_k) + \frac{1}{8\pi\epsilon_0}\sum_{k,k'}\frac{e^2}{|\mathbf{r}_k - \mathbf{r}_{k'}|} = \sum_k H_k + \sum_{k,k'} H_{k,k'}. \tag{3.7}$$

From now on the wave function (3.6) is not any more an exact solution for the Hamiltonian (3.7). The so-called Hartree approximation allow us to use the wave function (3.6) as an approximate solution for the Hamiltonian (3.7). Inserting the function (3.6) into the Schrödinger equation $H\phi = E\phi$, with H given by equation (3.7), the expectation value of the energy $E = \langle\phi|H|\phi\rangle$ can be written as :

$$E = \langle\phi|H|\phi\rangle = \sum_k \langle\varphi_k|H_k|\varphi_k\rangle + \frac{e^2}{8\pi\epsilon_0}\sum_{k,k'}\left\langle \varphi_k\varphi_{k'}\left|\frac{1}{|\mathbf{r}_k - \mathbf{r}_{k'}|}\right|\varphi_k\varphi_{k'}\right\rangle, \tag{3.8}$$

[1]The wave function depends also on the coordinates of atoms, but these coordinates appear only as parameters in equation (3.4).

where the φ_k are assumed to be normalized. This is only the expectation value of the energy for arbitrarily given φ_k. According to the variational principle, those φ_k which minimize E represent the best set of functions for the ground state. We therefore vary (3.8) for any φ_k^* or φ_k and equate the variation to zero

$$\delta[E - \sum_k \epsilon_k(\langle\phi_k|\phi_k\rangle - 1)] = 0, \tag{3.9}$$

We then get

$$\left[-\frac{\hbar^2}{2m}\nabla^2 + V(\mathbf{r}) + \frac{e^2}{4\pi\epsilon_0}\sum_{k'\neq k}\int\frac{|\varphi_{k'}(\mathbf{r}')|^2}{|\mathbf{r}-\mathbf{r}'|}d\tau'\right]\varphi_k(\mathbf{r}) = \epsilon_k\varphi_k(\mathbf{r}), \tag{3.10}$$

where E_k are the Lagrange parameters.
Here we are representing the positions of the k^{th} ($\mathbf{r}_k$) and the k'^{th} ($\mathbf{r}_{k'}$) electrons by $\mathbf{r}$ and $\mathbf{r}'$, respectively. Equation (3.10) is the *Hartree* [29] single-particle Schrödinger equation. It describes an electron (k) at location $\mathbf{r}$ in the potential field $V(\mathbf{r})$ of the lattice ions, and in the Coulomb potential of an average distribution of all other electrons ($k' \neq k$).
For the Pauli principle to apply, the expression (3.6) should be replaced by a Slater determinant

$$\phi = (N!)^{-1/2}\begin{vmatrix} \varphi_1(\mathbf{X}_1) & \dots & \varphi_N(\mathbf{X}_1) \\ \vdots & & \vdots \\ \varphi_1(\mathbf{X}_N) & \dots & \varphi_N(\mathbf{X}_N) \end{vmatrix}, \tag{3.11}$$

where the X_N coordinates stand for both the spatial coordinates r_N and the spin coordinates χ_N. The normalizing factor $(N!)^{-1/2}$ accounts for the indistinguishability of the electrons since there are $N!$ possible ways of distributing N electrons at the N positions $\mathbf{r}_1 \dots \mathbf{r}_N$. The fermionic character of the electrons is therefore insured by the antisymmetric wave function (3.11). With the wave function (3.11), we can again calculate the expectation value $E = \langle\phi\,|H|\,\phi\rangle$. It is given by

$$\begin{aligned} E = \sum_k\int\varphi_k^*(\mathbf{X}_1)H_k\varphi_k(\mathbf{X}_1)d\tau_1 + \frac{e^2}{8\pi\epsilon_0}\sum_{k,k'}\int\frac{|\varphi_k(\mathbf{X}_1)|^2\,|\varphi_{k'}(\mathbf{X}_2)|^2}{|\mathbf{r}_1-\mathbf{r}_2|}d\tau_1 d\tau_2 \\ -\frac{e^2}{8\pi\epsilon_0}\sum_{k,k'}\int\frac{\varphi_k^*(\mathbf{X}_1)\varphi_k(\mathbf{X}_2)\varphi_{k'}^*(\mathbf{X}_2)\varphi_{k'}(\mathbf{X}_1)}{|\mathbf{r}_1-\mathbf{r}_2|}d\tau_1 d\tau_2. \end{aligned} \tag{3.12}$$

The integration here includes a summation over the spin variables. We note further that in the absence of spin-orbit coupling, every wave function can be written as the product of a space function and a spin function. The last term of the right-hand side of (3.12) leaves us with just a summation over electrons with the same spin, because the orthogonality of the spin functions causes the other spin terms to disappear. Taking this into account, the spin does not explicitly appear further and we can replace $\mathbf{X}_k$ with just the space vectors $\mathbf{r}_k$. Equation (3.12) Compared with (3.8) an extra term appears. Taking into account the orthogonality condition, and invoking the variation equation (3.9), we find

$$\begin{aligned} \left[-\frac{\hbar^2}{2m}\nabla^2 + V(\mathbf{r})\right]\varphi_k(\mathbf{r}) + \frac{e^2}{4\pi\epsilon_0}\sum_{k'\neq k}\int\frac{|\varphi_{k'}(\mathbf{r}')|^2}{|\mathbf{r}-\mathbf{r}'|}d\tau'\varphi_k(\mathbf{r}) \\ -\frac{e^2}{4\pi\epsilon_0}\sum_{k'\neq k(spin||)}\int\frac{\varphi_{k'}^*(\mathbf{r}')\varphi_k(\mathbf{r}')}{|\mathbf{r}-\mathbf{r}'|}d\tau'\varphi_{k'}(\mathbf{r}) = \epsilon_k\varphi_k(\mathbf{r}), \end{aligned} \tag{3.13}$$

where, as in (3.10), we use $\mathbf{r}$ for the coordinates of the electron under consideration and $\mathbf{r}'$ for the integration variable. This is the *Hartree-Fock* equation [30, 31]. The Schrödinger equation for the many-electron problem is thus splitted up into one-electron wave equations. While the Hartree equation was easy to interpret, the newly added third term on the right-hand side of (3.13) has no classical analogue. It is called the *exchange interaction*. There is an equation of the same form for each of the different one-electron functions, and these equations must be solved simultaneously. For a single atom this can be done by a method of successive approximations, until self-consistency of the required degree of accuracy is reached. In metals the problem is too complicated and a cruder approximations must be used. Electrons repel one another, so that they do not move independently but in such a way as to avoid each other as far as possible. Such correlations among the electrons motions, or positions, are called *Coulomb correlations*. In the Hartree method Coulomb correlations are completely ignored, each electron being supposed to move in the *average* charge distribution of the other electrons. The total wave function is a single product of one-electron functions, so that the probability of a given configuration depends only upon the one-electron functions and not directly upon the distances between pairs of electrons. The Hartree-Fock method again neglects proper Coulomb correlations, but includes correlations of another sort. These are correlations among the positions of electrons with parallel spins only (the exchange interaction of the equation (3.13)), and are due, not to the Coulomb force, but to the Pauli principle, as embodied in the use of a determinantal wave function.
The correlations, associated with the exchange and known rather under the name of the exchange-correlations potential in the density functional theory (DFT) formalism, will be approached in more details in the fifth section of this chapter.
One of the early attempts to estimate the electron-electron interaction in solids and introduce the charge dependent total energy in solids is that of the Thomas-Fermi model [32, 33], the Hartree-Fock approximation and the X-α method of Slater [34]. The extension of these ideas, which have given rise to a revolution in the parameter-free *ab-initio* description of complex electronic structure, is known as DFT. This was established by Hohenberg and Kohn [35] and Kohn and Sham [36].

3.3 The Hohenberg-Kohn theorem

The finding of Hohenberg and Kohn for non-magnetic systems with a non-degenerate ground state is based on two theorems.
Theorem 1 *For a given external potential v, the total energy of a system is a unique functional of the ground state electron density.*
Theorem 2 *The exact ground state density minimizes the energy functional $E[n(\mathbf{r})]$.* A brief demonstration is provided in the Hohenberg-Kohn paper [35]. In their paper, the Hamiltonian H is defined as, $H = T + V + W$, for which T represents the kinetic energy of the system, V the interaction of the electrons with an external potential and W the electron-electron interaction. The solution of this Hamiltonian is the many-body wave function $\Psi(\mathbf{r}_1, \mathbf{r}_2, \ldots \mathbf{r}_N)$, and we have

$$H\Psi = E\Psi. \tag{3.14}$$

The electron density can be calculated from

$$n(\mathbf{r}) = \left\langle \mathbf{\Psi} \left| \sum_{\mathbf{i=1}}^{\mathbf{N}} \delta(\mathbf{r} - \mathbf{r_i}) \right| \mathbf{\Psi} \right\rangle \tag{3.15}$$

The extension of these theorems to the spin polarized systems can be done by including an external magnetic field, $B(\mathbf{r})$, so that the Hamiltonian becomes $H = T+U+W$, where $U = \int \upsilon(\mathbf{r})n(\mathbf{r}) - \mathbf{B}(\mathbf{r}) \cdot \mathbf{m}(\mathbf{r})d^3r$.
Using the variational principle (in the same way as it was used to demonstrate theorem 1) one can show that the ground state energy is a unique functional of the electron and magnetization density ($n(\mathbf{r})$ and $m(\mathbf{r})$). Using the theorems above to get a practical scheme to use DFT in describing solids Kohn and Sham [36] have shown that instead of solving the many-body equation (3.14), it suffices to solve an effective one-particle equation.

3.4 The Kohn-Sham equations

An important step on the way to finding an applicable approximation of the Hohenberg-Kohn functional energy is the Kohn-Sham [36] equations.
The main idea of their theory is to approximate the many-body equation (3.14) by a set of effective one-particle equations

$$\left[\frac{-\nabla^2}{2} + V_{eff}(\mathbf{r})\right] \psi_i(\mathbf{r}) = \epsilon_i \psi_i(\mathbf{r}), \tag{3.16}$$

where the effective potential $V_{eff}(\mathbf{r})$

$$V_{eff}(\mathbf{r}) = V_{ext}(\mathbf{r}) + \frac{e^2}{4\pi\epsilon_0} \int \frac{n(\mathbf{r}')}{|\mathbf{r} - \mathbf{r}'|} d^3r' + V_{xc}(\mathbf{r}), \tag{3.17}$$

where the first term is the external potential generated by the nuclei, the second term is the electrostatic potential and the last is the exchange-correlation potential supposed to include all many body effect. The density is now constructed using

$$n(\mathbf{r}) = \sum_{i=1}^{N} |\psi_i(\mathbf{r})|^2, \tag{3.18}$$

where the sum runs over all occupied states.
The set of equations (3.16-3.18) represents the Kohn-Sham equations. The Kohn-Sham equation (3.16) can be viewed as a Schrödinger equation in which the external potential is replaced by the effective potential (3.17), which depends on the density. The density itself depends on the one-particle states ψ_i. The Kohn-Sham equation therefore needs to be solved in a self-consistent manner. The total energy functional $E[n(\mathbf{r})]$ expressed in terms of the one particle energies ϵ_i (the Fock eigenvalues) has the form

$$E[n(\mathbf{r})] = T_0[n(\mathbf{r})] + \int n(\mathbf{r}) V_{ext}(\mathbf{r}) d^3r + \frac{e^2}{8\pi\epsilon_0} \int \int \frac{n(\mathbf{r}).n(\mathbf{r}')}{|\mathbf{r} - \mathbf{r}'|} d^3r d^3r' + E_{xc}[n(\mathbf{r})], \tag{3.19}$$

where $T_0[n(\mathbf{r})]$ accounts for independent-electron kinetic energy. This kinetic energy can be expressed in terms of the one particle energies ϵ_i (the Fock eigenvalues) as

$$T_0[n(\mathbf{r})] = \sum_i \epsilon_i - \int V_{eff}(\mathbf{r}) n(\mathbf{r}) d^3r. \tag{3.20}$$

The whole total-energy functional can then be rewritten by using (3.20) as

$$E[n(\mathbf{r})] = \sum_i \epsilon_i - \frac{e^2}{8\pi\epsilon_0}\int\int \frac{n(\mathbf{r}).n(\mathbf{r}')}{|\mathbf{r}-\mathbf{r}'|}d^3r d^3r' - \int V_{xc}(\mathbf{r})n(\mathbf{r})d^3r + E_{xc}[n(\mathbf{r})]. \quad (3.21)$$

The exact exchange-correlation potential V_{xc} and functional $E_{xc}[n(\mathbf{r})]$ are however not known and further approximations are needed for the solution of the electronic structure problem.

3.5 The Local Density Approximation

Since the first three terms on the right hand side of equation (3.19) are possible to calculate numerically, in this way the problem of the complexity of the fully interacting system is mapped onto the problem of finding the exchange and correlation functional. The most common and widely used approximation of the exchange-correlation functional is the local density approximation (LDA) where the exchange-correlation energy is assumed to be as in an homogeneous uniform electron gas,

$$E_{xc}[n(\mathbf{r})] = \int \epsilon_{xc}^{hom}[n(\mathbf{r})]n(\mathbf{r})d^3r, \quad (3.22)$$

where ϵ_{xc}^{hom} is the sum of the exchange and the correlation energy density of the uniform electron gas of density $n(\mathbf{r})$. The exchange energy can be calculated analytically and the correlation energy has been calculated to great accuracy numerically from quantum Monte Carlo methods [37]. The exchange-correlation potential $V_{xc}^{LDA}(\mathbf{r})$ is the functional derivative of E_{xc}^{LDA}, which can be written as

$$V_{xc}(\mathbf{r}) = \frac{\delta E_{xc}}{\delta n} = \epsilon_{xc}[n(\mathbf{r})] + n(\mathbf{r})\frac{\delta\epsilon_{xc}[n(\mathbf{r})]}{\delta n(\mathbf{r})}. \quad (3.23)$$

The most early attempts to parametrize the exchange-correlation energy ϵ_{xc} are those of Barth and Hedin [38]. The form suggested by von Barth and Hedin is given by

$$\epsilon_{xc}(n_\uparrow, n_\downarrow) = \epsilon_{xc}^P(r_s) + [\epsilon_{xc}^F(r_s) - \epsilon_{xc}^P(r_s)]f(n_\uparrow, n_\downarrow), \quad (3.24)$$

where

$$f(n_\uparrow, n_\downarrow) = [(2n_\uparrow/n)^{4/3} + (2n_\downarrow/n)^{4/3} - 2]/(2^{4/3} - 2), \quad (3.25)$$

$n_\uparrow$ and $n_\downarrow$ represent respectively the spin-up and spin-down components of the total charge n ($n = n_\uparrow + n_\downarrow$), and r_s is defined by

$$(4/3)\pi r_s^3 = 1/n. \quad (3.26)$$

The paramagnetic and ferromagnetic exchange-correlation energies ϵ_{xc}^P,ϵ_{xc}^F in equation (3.24) are given by

$$\epsilon_{xc}^i = \epsilon_{xc}^i(r_s) - c_i G(r_s/r_i), i = P, F \quad (3.27)$$

where $\epsilon_x^P = -0.91633/r_s$, $\epsilon_x^F = 2^{1/3}\epsilon_x^P$,

$$G(x) = (1+x^3)\ln(1+1/x) - x^2 + x/2 - 1/3, \quad (3.28)$$

and c_P, c_F, r_P, r_F were chosen by fitting equation (3.24) to ϵ_{xc} for the homogeneous electron gas. The resulting parameters [38] are:

$$C_P = 0.045, r_P = 21, c_F = c_P/2, r_F = 2^{4/3}r_P \quad (3.29)$$

The commonly used parametrization is that of Moruzzi *et al.* [39]. The corresponding parameters are:

$$C_P = 0.0504, r_P = 30, c_F = 0.0254, r_F = 75. \tag{3.30}$$

According to (3.24) and (3.23) the resulting potential takes the form:

$$\begin{aligned} V_{xc}^{\sigma} = \quad & [4/3\epsilon_x^P(r_s) + \gamma(\epsilon_c^F(r_s) - \epsilon_c^P(r_s))](2n_\sigma/n)^{1/3} \\ & +\mu_c^P(r_s) - \gamma(\epsilon_c^F(r_s) - \epsilon_c^P(r_s)) \\ & +[\mu_c^F(r_s) - \mu_c^P(r_s) - 4/3(\epsilon_c^F(r_s) - \epsilon_c^P(r_s)]f(n_\uparrow, n_\downarrow), \end{aligned} \tag{3.31}$$

where

$$\begin{aligned} \mu_c^P(r_s) &= -c_P \ln(1 + r_s/r_P), \\ \mu_c^F(r_s) &= -c_F \ln(1 + r_s/r_F), \\ \gamma &= 4/3(2^{1/3} - 1). \end{aligned} \tag{3.32}$$

This potential is referred to as the LDA exchange-correlation potential in the rest of the manuscript.
Although the local density approximation is rather simple and expected to be valid only for homogeneous cases, it turns out that it usually works remarkably well even for inhomogeneous cases. However, for solids LDA very often gives too small equilibrium volumes ($\sim 3\%$) due to overbinding. A simple improvement to the LDA that corrects the lattice parameter is based on the generalized gradient approximation (GGA).

3.6 The Generalized Gradient Approximation

Even though the LDA approximation has been successfully applied to systems with spatially varying charge density, it is rather valid for systems with nearly constant charge density. In order to understand the effect of the charge density variation in terms of the exchange-correlation interaction many attempts have been done so far. One of these attempts has given rise to the so-called generalized gradient approximation (GGA), where not only the density itself enters in the exchange-correlation energy but also its local gradient. The most successful one is the one suggested by Perdew and Wang (PW91) [40] and its simpler form by Perdew, Burke and Ernzerhof (PBE) [41]. We focus here on the latter one, which will be henceforth referred to as the GGA exchange-correlation potential.
The exchange-correlation energy has now the form:

$$E_{xc}^{GGA} = \int n(\mathbf{r})\epsilon_{xc}^{hom}(n(\mathbf{r}), |\nabla n|)d^3r. \tag{3.33}$$

Which can be expressed as [41]:

$$E_{xc}^{GGA} = \int f(n_\uparrow, n_\downarrow, \nabla n_\uparrow, \nabla n_\downarrow)d^3r. \tag{3.34}$$

The simplified scheme of the PBE approximation consists of evaluating separately the correlation and the exchange energy as follows:

$$E_c^{GGA} = \int [\epsilon_c^{unif} + H(r_s, \xi, t)]d^3r, \tag{3.35}$$

where r_s is the local Seitz radius (as defined by equation (3.26)), ξ is the relative spin polarization, and $t = |\nabla n|/2\phi(\xi)k_s n$ is a dimensionless density gradient. Here $\phi(\xi) = [(1+\xi)^{2/3} + (1-\xi)^{2/3}]/2$ is a spin scaling factor, and $k_s = \sqrt{(4k_F/\pi a_0)}$ is the Thomas-Fermi screening wave number. The constructed H function has the form:

$$H = 2\gamma\phi^3 \ln\left\{1 + \frac{\beta}{\gamma}t^2\left[\frac{1+At^2}{1+At^2+A^2t^4}\right]\right\}, \tag{3.36}$$

where

$$A = \frac{\beta}{\gamma}\left[exp(-\epsilon_c^{unif}/(\gamma\phi^3 e^2/a_0)) - 1\right]^{-1}. \tag{3.37}$$

$\beta = 0.066725$ and $\gamma = (1 - \ln 2)/\pi^2$. The exchange energy functional obeys the relationship:

$$E_x[n_\uparrow, n_\downarrow] = (E_x[2n_\uparrow] + E_x[2n_\downarrow])/2, \tag{3.38}$$

where

$$E_x = \int n\epsilon_x(n)F_x(s)d^3r, \tag{3.39}$$

and

$$F_x(s) = 1 + \kappa - \kappa/(1 + \mu s^2/\kappa). \tag{3.40}$$

where $s = |\nabla n|/2k_F n$ is another dimensionless density gradient, $\kappa = 0.804$ and $\mu = 0.21951$ are fitting parameters found optimal over a large number of systems.
It is worth mentioning here that like LDA the GGA approximation obeys the exchange and correlation hole density sum rules, firstly derived for LDA (Ref. [42] and references therein):

$$\int n_x(\mathbf{r}, \mathbf{r}')d^3r' = -1, \tag{3.41}$$

$$\int n_c(\mathbf{r}, \mathbf{r}')d^3r' = 0, \tag{3.42}$$

and the negativity condition of the exchange hole:

$$n_x(\mathbf{r}, \mathbf{r}') \leq 0, \tag{3.43}$$

where $\mathbf{r}' = \mathbf{r} + \mathbf{u}$ and $n_x(\mathbf{r}, \mathbf{r}+\mathbf{u})$, $n_c(\mathbf{r}, \mathbf{r}+\mathbf{u})$ are respectively the exchange and the correlation hole density of radius $\mathbf{u}$ surrounding the electron at $\mathbf{r}$ according to the exchange-energy definition of Gunnarson and Lundqvist [43]: the exchange-correlation energy is the electrostatic interaction of each electron at $\mathbf{r}$ with the density $n_{xc}(\mathbf{r}, \mathbf{r}+\mathbf{u}) = n_x + n_c$ at $\mathbf{r} + \mathbf{u}$ of the exchange-correlation hole which surrounds it. In other words, The exchange-correlation energy is the sum of electrostatic interaction energies over all electrons, whereby that situated at, say, $\mathbf{r}$, interacts only with the exchange-correlation hole $n_{xc}(\mathbf{r}, \mathbf{r}+\mathbf{u})$ it carries around. Figure 3.1 illustrates the difference between the exchange-correlation potential calculated using the GGA and LDA. As it can be seen from the figure, although both approximations lead to small differences for different radii (because each of them is satisfying the same sum-rules), this difference is locally perceptible (varying from 0.01 to 0.1 Htr). We have to mention here, that compared to the LDA exchange-potential the GGA one leads to better structural properties, i.e., it gives lattice parameters in better agreement with experiments, and gives somewhat a better estimation of the semiconductors energy gaps. However both the LDA and GGA potentials suffer from the self-interaction contribution. Perdew and Zunger [12] have tried to remove this

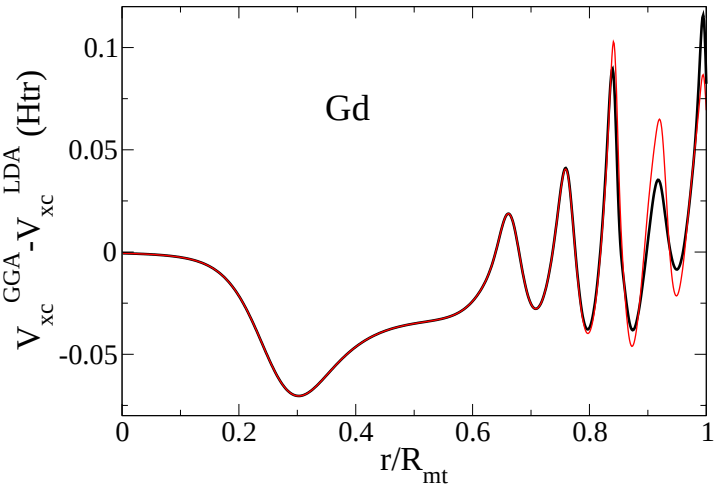

Figure 3.1: (Color online) The difference between the GGA exchange-correlation and that of the LDA up to the muffin-tin radii for gadolinium metal Gd. The spin up part (in black) and the spin down part (in red).

contribution which is not in Hartree-Fock based methods. Their self-interaction correction consists in proposing an exchange-correlation potential parametrization so that the sum of the self-interaction coming from the Coulomb interaction and that coming from the exchange-correlation tend to cancel each other:

$$U\left[n_{l,\sigma}\right] + E_{Coulomb}\left[n_{l,\sigma}\right] = 0, \tag{3.44}$$

where l is the orbital quantum number and σ the spin. Although this approximation has led to a good description (improved total energy and separate exchange and correlation pieces of it, and improved description of the charge density) of light atoms and a number of monovalent metallic atoms compared to the Hartree-Fock one, it has not been able to remove this self-interaction for extended systems such as molecules and solids with localized orbitals.
A powerful alternative is the so-called LDA(GGA)+U method, which allows us not only to keep the LDA(GGA) potential but also to add the intra-atomic Coulomb interaction, particularly necessary for strongly localized and correlated electrons systems. The LDA(GGA)+U method should be efficient to remove of the self-interaction of localized orbitals.

3.7 The LDA(GGA)+U method

The LDA+U method [44], which is a generalization of the Hubbard model [3, 4, 5, 6], is aimed to include the intra-atomic Coulomb interaction U in a mean field (MF) Hartree-Fock-like manner. The original idea of this method is to add the intra-atomic Coulomb potential for the localized orbitals to the Hamiltonian. Separating thus the electronic system into two systems: a Hartree-Fock-like localized electrons d (f) (with no self-interaction) and an LDA delocalized electrons (with negligible self-interaction). Because

of the involved localized orbitals (d or f) it would be technically practical to use atomiclike orbitals as basis functions. The linearized muffin-tin orbital method (LMTO) in the atomic-sphere approximation [44] (ASA) or its full-potential version [45] have been the first methods within which the LDA+U method was implemented. We present here the LDA+U implementation within the FLAPW method as it has been described by Shick *et al.* [7] without supplying details about the FLAPW method (the FLAPW method will be discussed in the next section). The variational LDA+U total-energy functional takes the form:

$$E^{LDA+U}\left[n_\sigma\right] = E^{LDA}\left[n_\sigma\right] + E^{ee}\left[n_\sigma\right] - E^{dc}\left[n_\sigma\right], \tag{3.45}$$

where $E^{LDA}\left[n_\sigma\right]$ is the LDA total energy, $E^{ee}\left[n_\sigma\right]$ is the electron-electron interaction energy of the correlated orbitals,

$$\begin{aligned} E^{ee} = \frac{1}{2}\sum_{\sigma,\sigma'}\sum_{m_1,m_2,m_3,m_4} n^{\sigma}_{m_1,m_2}(\langle m_1,m_3|V^{ee}|m_2,m_4\rangle \\ -\langle m_1,m_3|V^{ee}|m_4,m_2\rangle\delta_{\sigma,\sigma'})n^{\sigma'}_{m_3,m_4}, \end{aligned} \tag{3.46}$$

which can be also written as [45]

$$\begin{aligned} E^{ee} = \frac{1}{2}\sum_{\sigma}\sum_{m_1,m_2,m_3,m_4} \langle m_1,m_3|V^{ee}|m_2,m_4\rangle n^{\sigma}_{m_1,m_2}n^{-\sigma}_{m_3,m_4} \\ +(\langle m_1,m_3|V^{ee}|m_2,m_4\rangle \\ -\langle m_1,m_3|V^{ee}|m_4,m_2\rangle)n^{\sigma}_{m_1,m_2}n^{\sigma}_{m_3,m_4}, \end{aligned} \tag{3.47}$$

and in terms of U and J as [46]

$$\begin{aligned} E^{ee} = \frac{1}{2}\sum_{\sigma}\sum_{m_1,m_2,m_3,m_4} n^{\sigma}_{m_1,m_2}n^{-\sigma}_{m_3,m_4}U_{m_1,m_2,m_3,m_4} \\ + \left(U_{m_1,m_2,m_3,m_4} - J_{m_1,m_2,m_3,m_4}\right) n^{\sigma}_{m_1,m_2}n^{\sigma}_{m_3,m_4}, \end{aligned} \tag{3.48}$$

and $E^{dc}\left[n_\sigma\right]$ the double counting part;

$$E^{dc} = \frac{U}{2}n(n-1) - \frac{J}{2}\sum_{\sigma} n^{\sigma}(n^{\sigma}-1). \tag{3.49}$$

The LDA+U potential which corresponds to the E^{LDA+U} can be expressed as

$$V^{LDA+U} = \sum_{\sigma}\sum_{m_1,m_2} |m_1,\sigma\rangle V^{\sigma}_{m_1,m_2}\langle m_2,\sigma|, \tag{3.50}$$

where the potential matrix elements $V^{\sigma}_{m_1,m_2}$ are defined as

$$V^{\sigma}_{m_1,m_2} = \frac{\partial E^{LDA+U}}{\partial n^{\sigma}_{m,m'}} = \frac{\partial E^{ee}}{\partial n^{\sigma}_{m,m'}} - \frac{\partial E^{dc}}{\partial n^{\sigma}_{m,m'}}. \tag{3.51}$$

Using (3.45), (3.46) and (3.49), (3.51) can be expressed as:

$$\begin{aligned} V^{\sigma}_{m_1,m_2} = \sum_{\sigma}\sum_{m_3,m_4} \langle m_1,m_3|V^{ee}|m_2,m_4\rangle n^{-\sigma}_{m_3,m_4} + (\langle m_1,m_3|V^{ee}|m_2,m_4\rangle \\ -\langle m_1,m_3|V^{ee}|m_4,m_2\rangle)n^{\sigma}_{m_3,m_4} - \delta_{m_1,m_2}U(n-\frac{1}{2}) + \delta_{m_1,m_2}J(n^{\sigma}-\frac{1}{2}), \end{aligned} \tag{3.52}$$

where $n^\sigma = Tr(n^\sigma_{m_1,m_2})$ and $n = \sum_\sigma n^\sigma$.
According to (3.50) the expected value of V^{LDA+U} is then:

$$\langle \psi_i^\sigma | V^{LDA+U} | \psi_i^\sigma \rangle = \sum_{m_1,m_2} V^\sigma_{m_1,m_2} n^\sigma_{m_2,m_1}, \tag{3.53}$$

where

$$n^\sigma_{m_2,m_1} = \sum_{i\{occ\}} \langle \psi_i^\sigma | m_1, \sigma \rangle \langle m_2, \sigma | \psi_i^\sigma \rangle, \tag{3.54}$$

is the density matrix, and ψ_i^σ is the FLAPW wave function (see equation 4.55).
With the help of the variational principal, one can minimize equation (3.45) with respect to ψ_i^σ:

$$\left[\nabla^2 + V^\sigma_{LDA}(\mathbf{r})\right] \psi_i^\sigma(\mathbf{r}) + \sum_{m_1,m_2} V^\sigma_{m_1,m_2} \frac{\delta n^\sigma_{m_1,m_2}}{\delta \psi_i^\sigma} = e_i^\sigma \psi_i^\sigma(\mathbf{r}). \tag{3.55}$$

This set of equations is that of the Kohn-Sham equations with an additional term accounting for the U (LDA+U) correction for selected Hartree-Fock-like states only.
It is worth noticing that the present derivation of the LDA+U method (to which we will refer to from now on as the LDA+U method) is rotationally invariant [47]. That is because the main ingredients used in this formulation are of atomic-HF-equations. In its atomic limit the electron-electron interaction takes the form ([45] and references therein):

$$\begin{aligned} \langle m_1, m_3 | v^{ee} | m_2, m_4 \rangle &= \sum_k a_k(m_1, m_2, m_3, m_4) F_k, \\ a_k(m_1, m_2, m_3, m_4) &= \frac{4\pi}{2k+1} \sum_{q=-k}^{k} \langle l m_1 | Y_{kq} | l m_2 \rangle \langle l m_3 | Y^*_{kq} | l m_4 \rangle, \end{aligned} \tag{3.56}$$

where $|l, m\rangle$ are $d(f)$ spherical harmonics, F_k the Slater integrals and a_k are related to the Gaunt coefficients through the complex spherical harmonics.
The Slater integrals F_k are given by:

$$F_k = \frac{e^2}{4\pi\epsilon_0} \int_0^\infty \int_0^\infty dr_1 dr_2 \frac{r_<^k}{r_>^k} R_{k,m_1}(r_1) R_{k,m_2}(r_1) R_{k,m_1}(r_2) R_{k,m_2}(r_2), \tag{3.57}$$

where $r_<(r_>)$ is the lesser (greater) of r_1 and r_2.
The on-site Coulomb and exchange interactions U, J are given by:

$$\begin{aligned} U &= \frac{1}{(2l+1)^2} \sum_{m_1,m_3} \langle m_1, m_3 | v^{ee} | m_1, m_3 \rangle, \\ J &= U - \frac{1}{2l(2l+1)} \sum_{m_1,m_3} \left[\langle m_1, m_3 | V^{ee} | m_1, m_3 \rangle - \langle m_1, m_3 | V^{ee} | m_3, m_1 \rangle \right. \\ &= \frac{1}{2l(2l+1)} \sum_{m_1 \neq m_3, m_3} \langle m_1, m_3 | V^{ee} | m_3, m_1 \rangle. \end{aligned} \tag{3.58}$$

Although this atomic formulation is appropriate and reliable to incorporate these intra-atomic interactions, the electron-electron interaction (3.56) is *unscreened* and is therefore overestimated.
Some attempts have been already made to calculate U and J interactions. The results

obtained within the constrained LDA [48] calculations have shown the difficulty of simulating the screening effect for $3d$ and $4f$ systems in an electron gas, and led to too strong (for $3d$ metals) and too small (for $4f$ metals) intra-atomic interactions compared to that provided by experiment. It turns out that the most realistic way to get an estimation of these intra-atomic interactions is to make use of the experimental spectra such as XPS (X-ray Photoemission Spectroscopy) and BIS (Bremsstrahlung Isochromat Spectroscopy) spectra to extract the U and J interactions and use them as input *parameters* for LDA+U calculations (see paper I).
Once the U and J parameters (the *screened* interactions) are known, the Slater integrals can be calculated using equations (3.58);
for d orbitals (l=2):

$$\begin{aligned} U &= F_0, \\ J &= (F_2 + F_4)/14; F_4/F_2 = 5/8, \end{aligned} \tag{3.59}$$

for f orbitals (l=3):

$$\begin{aligned} U &= F_0, \\ J &= (286F_2 + 195F_4 + 250F_6)/6435; F_2/F_4 = 675/451; F_2/F_6 = 2025/1001. \end{aligned} \tag{3.60}$$

Even though the conception of the LDA+U scheme parametrization (using U and J as parameters) make the ab-initio DFT calculations lose its non-parametrized character, this method has provided a better description (compared to the LDA) of the electronic structure of transition-metal oxides and Mott-Hubbard insulators such as NiO and CoO [8, 9, 10, 11]. We will show in the following chapters that the LDA+U approach is also appropriate for describing electronic structure of correlated $4f$ rare-earth metals (paper I).

Chapter 4

The FLAPW Method

4.1 Introduction

Before introducing the full-potential linear augmented plane wave (FLAPW) method, we would like to give a brief overview of ab-initio methods. Several methods have been developed to practically solve the Kohn-Sham (KS) equations (3.16). The idea of dividing the space into spheres centered at each atom site, the so-called muffun-tin (MT) regions, and the remaining interstitial region was already proposed by Slater [49, 50, 51] before the KS equations. The concept of this division for a periodic potential corresponds to the Augmented Plane Wave (APW) technique. Soon after, this concept has been adopted by the Korringa [52], Kohn and Rostoker [53] (KKR) method. The APW method, as all the others MT orbital based methods, has known some deficiencies. The most problematic is that of the non-linearity of the eigenvalue equations with respect to the energy. Other methods, such as the orthogonalized plane wave (OPW) method [54] and the linear combination of atomic orbitals (LCAO) method [55], which are quite similar to the APW method[1], have been successful due to their accurate calculations of particular crystals. The applications of the OPW method, however, have been limited primarily to nearly-free-electron (NFE) crystals. The reasons for that can be summarized in two points. The first one is that this method requires the electrons in the crystal to be separated into core and itinerant electrons, and all the non-overlapping atomic states with the neighboring lattice site states are considered as core states, so that the *d*-states, for example, will be considered as such[2]. The second one is that the OPW method is more difficult to apply to heavy elements since they have more core electron states. Therefore orthogonalizing a plane wave function[3] to these states requires more efforts. The complications of the OPW method had stimulated, at that time, the development of the actually used pseudopotential methods.
In the APW method, all that is required is the total electronic charge density based on atomic self-consistent calculations.
Some years later Andersen [57] succeeded in linearizing these eigenvalue equations within the same MT model, which thus has given rise to both the linear muffin-tin orbitals (LMTO) method and the linear augmented plane wave (LAPW) method.

[1] Terrel has shown that the APW method gives nearly the same results as the OPW method for the Be metal [56].

[2] The problem which we would like to notice here is that though the *d*-states are relatively narrow and do not overlap with the other states they are still far from being considered as frozen core states.

[3] The OPW basis functions are constructed by orthogonalizing plane waves to the core states. The resulting OPW's have nodal character in the core region but are essentially plane waves in the outer part.

One of the commonly used methods to solve the Kohn-Sham equations is to use some kind of basis set to represent the Bloch wave functions. A suitable basis-set choice suggested by Bloch's theorem is a sum of plane waves. They have several advantages: the implementation of the plane-waves based methods is rather straightforward because of their simplicity; they are orthogonal and diagonal in momentum. The only problem which arises from this representation is that it requires so many plane waves to account for the fast varying electron wave functions near the core. To overcome this problem with only a few basis functions, one can use a basis set which contains radial wave functions to describe the oscillations near the core. This is the suggested fundamental idea by Slater [49] for the augmented plane wave (APW) method.

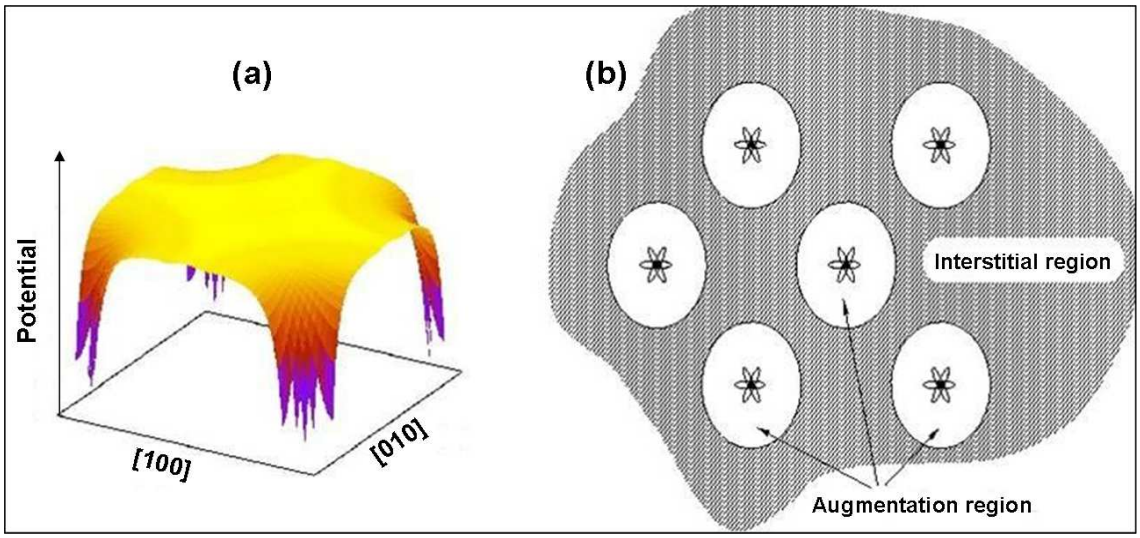

Figure 4.1: (a) A typical form of a based APW potential, (b) The representation of space into muffin-tin and interstitial regions.

4.2 The APW concept

Within the APW approach, space is divided into spheres centered at each atom site (the muffin-tin spheres), and the remaining region is the interstitial region (Fig. 4.1). Inside the muffin-tin spheres the potential is of spherical symmetry, and the interstitial potential is constant. The single particle wave function $\psi_\nu(\mathbf{k},\mathbf{r})$, which describes the physics within such environment, is therefore expressed in terms of the following basis functions:

$$\varphi_{\mathbf{G}}(\mathbf{k},\mathbf{r}) = \begin{cases} e^{i(\mathbf{G}+\mathbf{k})\mathbf{r}} & \text{interstitial region} \\ \sum_{lm} A_{lm}^{\mu\mathbf{G}}(\mathbf{k}) u_l(r) Y_{lm}(\hat{\mathbf{r}}) & \text{muffin-tin } \mu. \end{cases} \tag{4.1}$$

Thus, the wave function takes the form:

$$\psi(\mathbf{k},\mathbf{r}) = \sum_{\mathbf{G}} \mathbf{C}_{\mu\mathbf{k}}^{\mathbf{G}} \varphi_{\mathbf{G}}(\mathbf{k},\mathbf{r}) = \begin{cases} \sum_{\mathbf{G}} C_{\mu}^{\mathbf{G}}(\mathbf{k}) e^{i(\mathbf{G}+\mathbf{k})\mathbf{r}} & \text{interstitial region} \\ \sum_{\mathbf{G}} \sum_{lm} C_{\mu\mathbf{k}}^{\mathbf{G}} A_{lm}^{\mu}(\mathbf{k}) u_l(r) Y_{lm}(\hat{\mathbf{r}}) & \text{muffin-tin } \mu. \end{cases} \tag{4.2}$$

Where $\mathbf{k}$ is the Bloch wave vector, $\mathbf{G}$ is the reciprocal lattice vector, l and m are the angular quantum numbers, and u_l is the radial solution of the Schrödinger equation:

$$\left\{-\frac{\hbar^2}{2m}\frac{\partial^2}{\partial r^2}+\frac{\hbar^2}{2m}\frac{l(l+1)}{r^2}+V(r)-E_l\right\}ru_l(r)=0. \tag{4.3}$$

Here E_l is an energy parameter, and $V(r)$ is the spherical component of the potential. Since the u_l functions account for the regular solutions, the basis functions inside the spheres should form a completely orthogonal basis set and the u_l functions should be orthonormal. Using the Rayleigh expression:

$$e^{i(\mathbf{k}+\mathbf{G})\mathbf{r}}=4\pi\sum_{lm}i^l j_l(|\mathbf{k}+\mathbf{G}||\mathbf{r}|)Y^*_{lm}(\widehat{\mathbf{k}+\mathbf{G}})Y_{lm}(\hat{\mathbf{r}}), \tag{4.4}$$

and the continuity of the wave functions at the boundary of the muffin-tin spheres, the $A^{\mu\mathbf{G}}_{lm}(\mathbf{k})$ coefficients are calculated according to:

$$A^{\mu G}_{lm}(\mathbf{k})=\frac{4\pi i^l}{\sqrt{\Omega}u_l(R)}\sum_{\mathbf{G}}C^{\mathbf{G}}_{\mu}(\mathbf{k})j_l(|\mathbf{k}+\mathbf{G}||\mathbf{R}|)Y_{lm}(\widehat{\mathbf{k}+\mathbf{G}}), \tag{4.5}$$

where R is the muffin-tin radius and Ω is the cell volume.
The eigenvalue problem has the following form:

$$\hat{H}\psi_\nu(\mathbf{k},\mathbf{r})=\varepsilon_{\nu\mathbf{k}}\psi_\nu(\mathbf{k},\mathbf{r}), \tag{4.6}$$

where ν is the band index.
Even though plane waves form an orthogonal basis set, the APW functions do not. The plane waves in the interstitial region are non-orthogonal, because the muffin-tin regions are cut-out and, therefore, the integration over r space (in terms of which the orthogonality is defined) is not carried out over the whole unit cell, but only over the interstitial region. An additional contribution comes from the muffin-tin regions, this is the so-called *augmented* contribution, which somehow, make the plane waves coupled to the muffin-tin functions $(u_l(r)Y_{lm}(\hat{r}))$.
Due to the non-orthogonality of the basis functions the overlap matrix $\mathbf{S}$:

$$S^{\mathbf{G},\mathbf{G}'}(\mathbf{k})=\int\varphi_{\mathbf{G}'}(\mathbf{k},\mathbf{r})\varphi_{\mathbf{G}}(\mathbf{k},\mathbf{r})d^3r, \tag{4.7}$$

is not diagonal.
Using the wave function expansion (4.2), the eigenvalue problem (4.6) can be rewritten in its generalized form as:

$$(\mathrm{H}(\mathbf{k})-\varepsilon_{\nu\mathbf{k}}\mathbf{S}(\mathbf{k}))\mathbf{C}_{\nu\mathbf{k}}=\mathbf{0}\qquad\forall\,\mathbf{k}\in\mathrm{BZ}. \tag{4.8}$$

Within the APW method, the E_l parameters are mapped to the *real* band energies $\varepsilon_{\nu\mathbf{k}}$, thus the u_l solutions become the functions of these band energies $u_l(r,\varepsilon_{\nu\mathbf{k}})$, and the equation (4.8) is therefore nonlinear in energy[4], so it can no longer be determined by a simple diagonalization. One way of solving this problem is to fix the energy E_l and scan over $\mathbf{k}$ to find the solution $u_l(\varepsilon_{\nu\mathbf{k}})$, which corresponds to the optimal shape of the band energies $\varepsilon_{\nu\mathbf{k}}$, instead of diagonalizing a matrix to find all the bands at a given $\mathbf{k}$. The Slater's formulation of the secular equation is, thus, computationally much more

[4]The Hamiltonian matrix H depends not only on $\mathbf{k}$, but also on $\varepsilon_{\nu\mathbf{k}}$, $\mathrm{H}(\varepsilon_{\nu\mathbf{k}})$.

demanding than an ordinary linear one.
Another limitation of the APW method (known as the *asymptote* problem) is that of the zero value of $u_l(R)$ at the MT boundary in equation (4.5). The $A_{lm}^{\mu G}$'s are no longer finite, and the radial function and the plane wave become decoupled. Further details about the APW method can be found in the book by Loucks [58], which contains several early papers including Slater's original publications.
These problems are circumvented within the LAPW method proposed by Andersen [57]. The following section is devoted to the discussion of the main features of this method.

4.3 The LAPW concept

The basic idea of the linearized version of the APW (LAPW) is to expand the u_l functions into a Taylor-series around the E_l energy parameters

$$u_l(\varepsilon, r) = u_l(E_l, r) + \dot{u}_l(E_l, r)(\varepsilon - E_l) + O[(\varepsilon - E_l)^2]. \tag{4.9}$$

Here $\dot{u}_l$ denotes the energy derivative of u_l, $\partial u_l(\varepsilon, r)/\partial\epsilon$, and $O[(\varepsilon - E_l)^2]$ denotes errors that are quadratic in energy. Therefore, according to the variational principle the error in the calculated band energies is of order $(\varepsilon - E_l)^4$. Because of this high order, the linearization works well even over a rather broad energy region.
With this linearization, the explicit form of the basis functions is now as following:

$$\varphi_{\mathbf{G}}(\mathbf{k}, \mathbf{r}) = \begin{cases} e^{i(\mathbf{G}+\mathbf{k})\mathbf{r}} & \text{interstitial region} \\ \sum_{lm}(A_{lm}^{\mu\mathbf{G}}(\mathbf{k})u_l(r) + B_{lm}^{\mu\mathbf{G}}(\mathbf{k})\dot{u}_l(r))Y_{lm}(\hat{\mathbf{r}}) & \text{muffin-tin } \mu. \end{cases} \tag{4.10}$$

The values of the coefficients $A_{lm}^{\mu\mathbf{G}}(\mathbf{k})$ and $B_{lm}^{\mu\mathbf{G}}(\mathbf{k})$ are determined by ensuring the continuity of the basis functions and their derivatives at the muffin-tin boundary (a detailed description of these coefficients will be provided in the following sections). The energy dependence of the Hamiltonian is therefore removed, which reduces the energy search given by equation (4.8) to a standard eigenvalue problem of linear algebra. This is a direct consequence of the disappearance of the discontinuity in the basis functions derivatives (encountered in the APW method).
Taking the energy derivative of equation (4.3);

$$\left\{-\frac{\hbar^2}{2m}\frac{\partial^2}{\partial r^2} + \frac{\hbar^2}{2m}\frac{l(l+1)}{r^2} + V(r) - E_l\right\} r\dot{u}_l(r) = r u_l(r), \tag{4.11}$$

$\dot{u}_l$ can be calculated as a solution of a Schrödinger-like equation.
Since it is no longer necessary to set the energy parameters equal to the band energies, the latter can be determined by a single diagonalization of the Hamiltonian matrix (equation (4.8)).
In order to simplify the calculation of the elements of the Hamiltonian matrix, the normalization of u_l is required,

$$\int_0^{R_{MT}} u_l^2(r) r^2 dr = 1, \tag{4.12}$$

which implies that the energy derivatives of u_l, $\dot{u}_l(r)$ are orthogonal to the radial functions, i.e.,

$$\int_0^{R_{MT}} u_l(r)\dot{u}_l(r) r^2 dr = 0. \tag{4.13}$$

Once the u_l and $\dot{u}_l$ are made orthogonal, the basis functions inside the spheres form a completely orthogonal basis set, since the angular functions $Y_{lm}(\hat{r})$ are also orthogonal. However, the LAPW functions are, in general, not orthogonal to the core states, which are treated separately in the LAPW method.
In some materials the high-lying core states, the so-called semicore states, pose a problem to LAPW calculations: they are too delocalized to be described as core states, and too deep in energy to be described as valence (conduction) states[5]. One of the strategies to overcome this problem is the use of local orbitals [59]. The local orbitals are an extension to the FLAPW basis, that can be used to improve the representation of the semicore states. The extra basis functions are completely localized inside the muffin-tin spheres, and their values and derivatives fall to zero at the muffin-tin radii[6]. This can be achieved via a linear combination including three radial functions, the standard FLAPW functions u_l and $\dot{u}_l$ plus a further radial function $u_{l_{lo}}$, where l_{lo} is the quantum number l for local orbitals. This new radial function is constructed in the same way as u_l, but with different energy parameter $E_{l_{lo}}$. A detailed discussion of these problems can be found in the book by Singh [14].
The three functions u_l, $\dot{u}_l$ and $u_{l_{lo}}$ have to be combined, so that the value and the derivative of the local orbital are zero at the muffin-tin radii. In addition, the resulting radial functions can be required to be normalized. Hence, to determine the coefficients of the radial functions $A^{\mu\mathbf{G_{lo}}}_{l_{lo}m}$, $B^{\mu\mathbf{G_{lo}}}_{l_{lo}m}$ and $C^{\mu\mathbf{G_{lo}}}_{l_{lo}m}$ we make use of the following three conditions:

$$a_{l_{lo}}u_l(R_{MT}) + b_{l_{lo}}\dot{u}_l(R_{MT}) + c_{l_{lo}}u_{l_{lo}}(R_{MT}) = 0, \tag{4.14}$$

$$a_{l_{lo}}\frac{\partial u_l}{\partial r}(R_{MT}) + b_{l_{lo}}\frac{\partial \dot{u}_l}{\partial r}(R_{MT}) + c_{l_{lo}}\frac{\partial u_{l_{lo}}}{\partial r}(R_{MT}) = 0, \tag{4.15}$$

$$\int_0^{R_{MT}} (a_{l_{lo}}u_l(r) + b_{l_{lo}}\dot{u}_l(r) + c_{l_{lo}}u_{l_{lo}}(r))^2 r^2 dr = 1, \tag{4.16}$$

where lo is the index of the local orbital, which is necessary because more than one local orbital can be added for each atom.
The local orbitals are finally coupled to "fictitious" plane waves, $\mathbf{G}_{lo}$, in the same way as the FLAPW basis functions:

$$\varphi^{\mu,lo}_{\mathbf{G_{lo}}}(\mathbf{k},\mathbf{r}) = \sum_m (A^{\mu\mathbf{G_{lo}}}_{l_{lo}m}(\mathbf{k})u_l + B^{\mu\mathbf{G_{lo}}}_{l_{lo}m}(\mathbf{k})\dot{u}_l + C^{\mu\mathbf{G_{lo}}}_{l_{lo}m}(\mathbf{k})u_{l_{lo}})Y_{lm}(\hat{r}), \tag{4.17}$$

with (cf. equations (4.45))

$$A^{\mu\mathbf{G_{lo}}}_{l_{lo}m}(\mathbf{k}) = e^{i(\mathbf{k}+\mathbf{G_{lo}})\boldsymbol{\tau}^\mu} a_{l_{lo}} 4\pi \frac{1}{W} i^l Y^*_{lm}(\widehat{\mathbf{k}+\mathbf{G_{lo}}}), \tag{4.18}$$

$$B^{\mu\mathbf{G_{lo}}}_{l_{lo}m}(\mathbf{k}) = e^{i(\mathbf{k}+\mathbf{G_{lo}})\boldsymbol{\tau}^\mu} b_{l_{lo}} 4\pi \frac{1}{W} i^l Y^*_{lm}(\widehat{\mathbf{k}+\mathbf{G_{lo}}}), \tag{4.19}$$

$$C^{\mu\mathbf{G_{lo}}}_{l_{lo}m}(\mathbf{k}) = e^{i(\mathbf{k}+\mathbf{G_{lo}})\boldsymbol{\tau}^\mu} c_{l_{lo}} 4\pi \frac{1}{W} i^l Y^*_{lm}(\widehat{\mathbf{k}+\mathbf{G_{lo}}}). \tag{4.20}$$

In the results chapter we shall show the necessity of treating the 5s and 5p orbitals as semicore orbitals for Gd metal (paper I) and GdN compound (paper II).
Given that the LAPW basis set offers enough variational freedom, its extension to non spherical potentials could be done with little difficulty. This leads then to the full-potential linearized augmented plane wave method (FLAPW).

[5] The corresponding energy parameter E_l, is already used to describe higher localized valence state.
[6] That is why no additional boundary conditions has to be satisfied.

4.4 The FLAPW concept

The full-potential LAPW method (FLAPW) [18, 19] combines the choice of the LAPW basis set with the treatment of the full-potential and charge density without any shape-approximation in the interstitial region and inside the muffin-tins:

$$V(\mathbf{r}) = \begin{cases} \sum_{\mathbf{G}} V_I^{\mathbf{G}} e^{i\mathbf{G}\mathbf{r}} & \text{interstitial region} \\ \sum_{lm} V_{MT}^{l,m}(r) Y_{lm}(\hat{\mathbf{r}}) & \text{muffin-tin,} \end{cases} \tag{4.21}$$

the charge density, $\rho(\mathbf{r})$, is represented in the same way as the potential:

$$\rho(\mathbf{r}) = \begin{cases} \sum_{\mathbf{G}} \rho_I^{\mathbf{G}} e^{i\mathbf{G}\mathbf{r}} & \text{interstitial region} \\ \sum_{lm} \rho_{MT}^{l,m}(r) Y_{lm}(\hat{\mathbf{r}}) & \text{muffin-tin.} \end{cases} \tag{4.22}$$

We have to mention here that though the potential is nearly constant in the interstitial region (the open systems and the systems with small packing factor), this is not the case for the most of the metallic materials with relatively high packing factor. It turns out that on contrary to the methods using the atomic sphere approximation (ASA)[7] [57], the FLAPW method accounts for the most realistic potential and leads, therefore, to a realistic distribution of the charge density within the whole space. In other words, within the FLAPW scheme the charge density is sensitive to the slightest variation of the potential in the whole space.

As other density functional theory based codes, the first-principles FLAPW (Fleur code

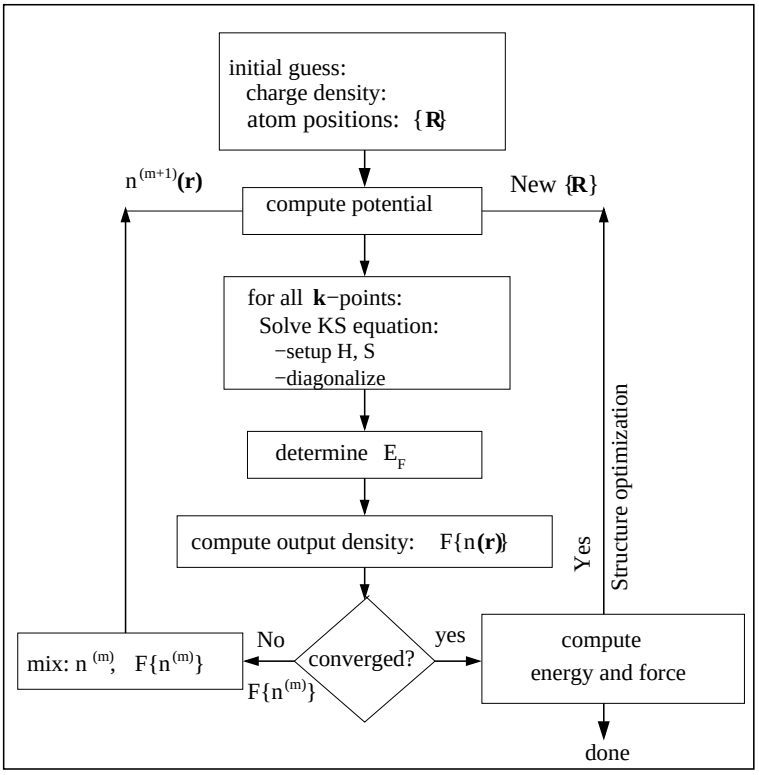

Figure 4.2: Typical loop structure of a first-principles code based on density functional theory.

[25]) method is implemented according to a typical self-consistent loop (figure (4.2)). We provide in the following subsections the features of the main steps of a bulk calculation.

[7] In this method the potential is represented by the spherically averaged potentials in the overlapping space-filling spheres centered at the atomic nuclei; such treatment of the potential and the charge space-filling within both of the regions (muffin-tin and interstitial) on the same footing was at the origin of the ASA method failure for many materials [60], i.e., the conduction band structure is strongly dependent on the sphere radius.

4.4.1 Construction of the potential

The total potential consists of two parts, the Coulomb potential, and the exchange-correlation potential. The Coulomb potential is composed of the Hartree potential $V_H(\mathbf{r})$ and the external potential of the nuclei $V_i(\mathbf{r})$:

$$V_c(\mathbf{r}) = V_H(\mathbf{r}) + V_i(\mathbf{r}). \tag{4.23}$$

Once an initial charge density $n^0(\mathbf{r})$ (atomic charge) and atom positions ($\mathbf{R}$) are given, the Hartree potential can be determined from the charge density via the Poisson equation:

$$\triangle V_H(\mathbf{r}) = \frac{en(\mathbf{r})}{\epsilon_0}, \tag{4.24}$$

in real space the solution of equation (4.24) is given by:

$$V_H(\mathbf{r}) = \frac{e}{4\pi\epsilon_0} \int \frac{n(\mathbf{r})}{|\mathbf{r} - \mathbf{r}'|} d^3r. \tag{4.25}$$

In reciprocal space, however, the Poisson equation is diagonal:

$$V_H(\mathbf{G}) = \frac{en(\mathbf{G})}{\epsilon_0 \mathbf{G}^2}. \tag{4.26}$$

Therefore, and because of the representation of the charge density and the potential in the interstitial region, the solution of the Poisson equation in reciprocal space appears to be convenient. However, due to the rather localized core and valence states the charge density changes on a very small length scale near the nuclei (the muffin-tin region). Thus, the plane wave expansion of n converges slowly, and a direct use of equation (4.26) is impractical. The pseudocharge method [61] is used to circumvent this difficulty.
The problem of determining the exchange-correlation potential is quite different from that of the Coulomb potential, V_{xc}^{σ} is a local quantity and depends only on $n_{\uparrow}(\mathbf{r})$ and $n_{\downarrow}(\mathbf{r})$ at the same position $\mathbf{r}$. Thus, the muffin-tin and the interstitial regions can be treated independently. Furthermore, V_{xc}^{σ} and ϵ_{xc}^{σ} are non-linear functions of $n_{\uparrow}$ and $n_{\downarrow}$, and have to be calculated in real space. First, $n_{\uparrow}$ and $n_{\downarrow}$ are transformed to the real space, where V_{xc}^{σ} and ϵ_{xc}^{σ} are calculated[8], and then back-transformed. The potential V_{xc}^{σ} is then added to the Coulomb potential, yielding the spin-dependent potential $V_{\uparrow}$ and $V_{\downarrow}$, whereas ϵ_{xc}^{σ} is needed for the determination of the total energy.

4.4.2 Construction of the Hamiltonian matrix

The FLAPW Hamiltonian and overlap matrices consist of two contributions from the two regions into which space is divided.

$$H = H_I + H_{MT} \quad \text{and} \quad S = S_I + S_{MT}. \tag{4.27}$$

Both contributions have to be computed separately.

[8] As it was explained in section (3.5) and section (3.6), V_{xc}^{σ} and ϵ_{xc}^{σ} are calculated using either the LDA or the GGA.

The muffin-tins contribution

By writing the product of the radial functions u_l with the spherical harmonics as $\phi_{lm} = u_l Y_{lm}$, the contribution of the muffin-tin to the Hamiltonian matrix is given by:

$$H_{MT}^{\mathbf{G}'\mathbf{G}}(\mathbf{k}) = \sum_\mu \int_{MT^\mu} \left((\sum_{l',m'} A_{l'm'}^{\mu\mathbf{G}'}(\mathbf{k}) \phi_{l'm'}(\mathbf{r}-\mathbf{R}_\mu) + B_{l'm'}^{\mu\mathbf{G}'}(\mathbf{k}) \dot{\phi}_{l'm'}(\mathbf{r}-\mathbf{R}_\mu) \right) \hat{H}_{MT^\mu} \left((\sum_{l,m} A_{lm}^{\mu\mathbf{G}}(\mathbf{k}) \phi_{lm}(\mathbf{r}-\mathbf{R}_\mu) + B_{lm}^{\mu\mathbf{G}}(\mathbf{k}) \dot{\phi}_{lm}(\mathbf{r}-\mathbf{R}_\mu) \right) d^3r, \quad (4.28)$$

and

$$S_{MT}^{\mathbf{G}'\mathbf{G}}(\mathbf{k}) = \sum_\mu \int_{MT^\mu} \left((\sum_{l',m'} A_{l'm'}^{\mu\mathbf{G}'}(\mathbf{k}) \phi_{l'm'}(\mathbf{r}-\mathbf{R}_\mu) + B_{l'm'}^{\mu\mathbf{G}'}(\mathbf{k}) \dot{\phi}_{l'm'}(\mathbf{r}-\mathbf{R}_\mu) \right) . \left((\sum_{l,m} A_{lm}^{\mu\mathbf{G}}(\mathbf{k}) \phi_{lm}(\mathbf{r}-\mathbf{R}_\mu) + B_{lm}^{\mu\mathbf{G}}(\mathbf{k}) \dot{\phi}_{lm}(\mathbf{r}-\mathbf{R}_\mu) \right) d^3r, \quad (4.29)$$

where $\hat{H}_{MT^\mu}$ is the scalar relativistic Hamiltonian operator. It can be split into two parts, the spherical Hamiltonian $\hat{H}_{sp}$ (equation (4.3)) and the nonspherical contributions to the potential V_{ns}:

$$\hat{H}_{MT}^\mu = \hat{H}_{sp} + V_{ns}. \quad (4.30)$$

The functions $\phi_{l,m}$ and $\dot{\phi}_{l,m}$ have been chosen to diagonalize the spherical part of the muffin-tin Hamiltonian (equations (4.3) and (4.11):

$$\hat{H}_{sp}|\phi_{l,m}\rangle = E_l|\phi_{l,m}\rangle \quad \text{and} \quad \hat{H}_{sp}|\dot{\phi}_{l,m}\rangle = E_l|\dot{\phi}_{l,m}\rangle + |\phi_{l,m}\rangle. \quad (4.31)$$

Multiplying these equations by $\phi_{l'm'}(\mathbf{r})$ and $\dot{\phi}_{l'm'}(\mathbf{r})$, respectively, and integrating over the muffin-tins gives:

$$\langle\phi_{l',m'}|\hat{H}_{sp}|\phi_{l,m}\rangle_{MT^\mu} = \delta_{ll'}\delta_{mm'}E_l; \qquad \langle\phi_{l',m'}|\hat{H}_{sp}|\dot{\phi}_{l,m}\rangle_{MT^\mu} = 0$$
$$\langle\dot{\phi}_{l',m'}|\hat{H}_{sp}|\phi_{l,m}\rangle_{MT^\mu} = 0; \quad \langle\dot{\phi}_{l',m'}|\hat{H}_{sp}|\dot{\phi}_{l,m}\rangle_{MT^\mu} = \delta_{ll'}\delta_{mm'}E_l\langle\dot{u}_l|\dot{u}_l\rangle_{MT^\mu}, \quad (4.32)$$

where the normalization condition for u_l has been used.
The above integrations contain the following type of matrix elements:

$$t_{ll'mm'}^{\mu\phi\phi} = \int_{MT^\mu} \phi_{l',m'}(\mathbf{r}) \hat{H}_{MT^\mu} \phi_{l,m}(\mathbf{r}) d^3r. \quad (4.33)$$

Since the potential is expanded into a product of radial functions and spherical harmonics:

$$V^\mu(\mathbf{r}) = \sum_{l'',m''} V_{l''m''}^\mu(\mathbf{r}) Y_{l''m''}(\hat{\mathbf{r}}), \quad (4.34)$$

the corresponding integrals consist of a product of radial integrals and angular integrals over three spherical harmonics, the so-called Gaunt coefficients:

$$t_{ll'mm'}^{\mu\phi\phi} = \sum_{l''} I_{l'll''}^{\mu uu} G_{l'll''}^{m'mm''} + \delta_{ll'}\delta_{mm'}E_l. \quad (4.35)$$

where

$$G_{l'll''}^{m'mm''} = \int Y_{lm}^* Y_{l'm'} Y_{l''m''} d\Omega \quad \text{and} \quad I_{l'll''}^{\mu uu} = \int u_{l'}^\mu(r) u_l^\mu(r) V_{l''}^\mu(r) r^2 dr, \quad (4.36)$$

as well as similar expressions for $I_{l'll''}^{\mu u\dot{u}}$ and others. Finally, the Hamiltonian and overlap matrix elements become:

$$H_{MT}^{\mathbf{G}'\mathbf{G}}(\mathbf{k}) = \sum_\mu \sum_{l'm',lm} (A_{l'm'}^{\mu\mathbf{G}'}(\mathbf{k}))^* t_{l'm'lm}^{\mu\phi\phi} A_{lm}^{\mu\mathbf{G}}(\mathbf{k}) + (B_{l'm'}^{\mu\mathbf{G}'}(\mathbf{k}))^* t_{l'm'lm}^{\mu\dot{\phi}\dot{\phi}} B_{lm}^{\mu\mathbf{G}}(\mathbf{k}) + (A_{l'm'}^{\mu\mathbf{G}'}(\mathbf{k}))^* t_{l'm'lm}^{\mu\phi\dot{\phi}} B_{lm}^{\mu\mathbf{G}}(\mathbf{k}) + (B_{l'm'}^{\mu\mathbf{G}'}(\mathbf{k}))^* t_{l'm'lm}^{\mu\dot{\phi}\phi} A_{lm}^{\mu\mathbf{G}}(\mathbf{k}), \quad (4.37)$$

$$S_{MT}^{\mathbf{G}'\mathbf{G}}(\mathbf{k}) = \sum_\mu \sum_{lm} (A_{lm}^{\mu\mathbf{G}'}(\mathbf{k}))^* A_{lm}^{\mu\mathbf{G}}(\mathbf{k}) + (B_{lm}^{\mu\mathbf{G}'}(\mathbf{k}))^* B_{lm}^{\mu\mathbf{G}}(\mathbf{k}) \langle\dot{u}_l|\dot{u}_l\rangle_{MT\mu}. \quad (4.38)$$

The interstitial contribution

The interstitial contributions to the Hamiltonian and overlap matrix have the following form:

$$H_I^{\mathbf{GG'}}(\mathbf{k}) = \frac{1}{\Omega}\int_I e^{-i(\mathbf{G}+\mathbf{k})\mathbf{r}}(-\frac{\hbar^2}{2m}\triangle + V(\mathbf{r}))e^{i(\mathbf{G'}+\mathbf{k})\mathbf{r}}, \tag{4.39}$$

$$S_I^{\mathbf{GG'}} = \frac{1}{\Omega}\int_I e^{-i(\mathbf{G}+\mathbf{k})\mathbf{r}}e^{i(\mathbf{G'}+\mathbf{k})\mathbf{r}}. \tag{4.40}$$

The potential is also expanded into plane waves in the interstitial region:

$$V(\mathbf{r}) = \sum_{\mathbf{G}} V_{\mathbf{G}} e^{-i\mathbf{G}\mathbf{r}}. \tag{4.41}$$

Once the Hamiltonian and overlap matrix are determined in the whole space (muffin-tins and interstitial), the eigenvalue problem (equation (4.8)) will be solved for each $\mathbf{k}$ point of the Brillouin zone.

4.4.3 The muffin-tin A- and B- coefficients

Within the FLAPW method the electron wave functions are expanded differently in the interstitial region and in the muffin-tins. Each basis function consists of a plane wave in the interstitial region, which is matched to the radial functions and spherical harmonics in the muffin-tins. The coefficients of the function inside the sphere are determined from the requirement that the basis functions and their derivatives are continuous at the sphere boundaries. A plane wave $e^{i\mathbf{K}\mathbf{r}}$ within the *global representation* transforms to $e^{i(\mathbf{R}^\mu\mathbf{K})(\mathbf{r}+\mathbf{R}^\mu\boldsymbol{\tau})}$ within the *local representation*. Therefore, the Rayleigh expansion (equation (4.4)) expressed in the global frame becomes in the local frame:

$$e^{i\mathbf{K}\mathbf{r}} = e^{i\mathbf{K}\boldsymbol{\tau}^\mu}4\pi\sum_{lm} i^l j_l(|\mathbf{K}||\mathbf{r}|)Y_{lm}^*(\mathbf{R}^\mu\hat{\mathbf{K}})Y_{lm}(\hat{\mathbf{r}}), \tag{4.42}$$

where $\mathbf{K}$ abbreviates $\mathbf{G}+\mathbf{k}$, and $\boldsymbol{\tau}^\mu$ is the position of a μ atom type in the global frame. Indeed, $\mathbf{K}$ and $\boldsymbol{\tau}^\mu$ looked at from the local frame viewpoint appear to be transformed according to the space group operations $\{\mathbf{R}|\mathbf{t}\}$. More details can be found in the physics diploma by Philipp Kurz [62].
The first requirement of continuity of the wave functions at the sphere boundary leads to the equation:

$$\begin{aligned}&\sum_{lm}(A_{lm}^{\mu\mathbf{G}}(\mathbf{k})u_l(R_{MT}) + B_{lm}^{\mu\mathbf{G}}(\mathbf{k})\dot{u}_l(R_{MT}))Y_{lm}(\hat{\mathbf{r}})\\ &= e^{i\mathbf{K}\boldsymbol{\tau}^\mu}4\pi\sum_{lm} i^l j_l(|\mathbf{K}||\mathbf{R}_{MT}|)Y_{lm}^*(\mathbf{R}^\mu\hat{\mathbf{K}})Y_{lm}(\hat{\mathbf{r}}).\end{aligned} \tag{4.43}$$

The second requirement is, that the derivative with respect to r, denoted by $\partial u/\partial r \equiv u'$, is also continuous:

$$\begin{aligned}&\sum_{lm}(A_{lm}^{\mu\mathbf{G}}(\mathbf{k})u_l'(R_{MT}) + B_{lm}^{\mu\mathbf{G}}(\mathbf{k})\dot{u_l'}(R_{MT}))Y_{lm}(\hat{\mathbf{r}})\\ &= e^{i\mathbf{K}\boldsymbol{\tau}^\mu}4\pi\sum_{lm} i^l j_l'(|\mathbf{K}||\mathbf{R}_{MT}|)Y_{lm}^*(\mathbf{R}^\mu\hat{\mathbf{K}})Y_{lm}(\hat{\mathbf{r}}).\end{aligned} \tag{4.44}$$

Therefore, the $A_{lm}^{\mu\mathbf{G}}(\mathbf{k})$ and $B_{lm}^{\mu\mathbf{G}}(\mathbf{k})$ coefficients, which satisfy these conditions, are determined as:

$$A_{lm}^{\mu\mathbf{G}}(\mathbf{k}) = e^{i\mathbf{K}\boldsymbol{\tau}^{\mu}} 4\pi \frac{1}{W} i^l Y_{lm}^*(\mathbf{R}^{\mu}\hat{\mathbf{K}}) \left[\dot{u}_l(R_{MT}) K j_l'(R_{MT}K) - \dot{u}_l'(R_{MT}) j_l(R_{MT}K)\right],$$
$$B_{lm}^{\mu\mathbf{G}}(\mathbf{k}) = e^{i\mathbf{K}\boldsymbol{\tau}^{\mu}} 4\pi \frac{1}{W} i^l Y_{lm}^*(\mathbf{R}^{\mu}\hat{\mathbf{K}}) \left[u_l'(R_{MT}) K j_l(R_{MT}K) - u_l(R_{MT}) j_l'(R_{MT}K)\right], \quad (4.45)$$

where K denotes $|\mathbf{K}|$ and W is the Wronskian:

$$W = \left[\dot{u}_l(R_{MT}) u_l'(R_{MT}) - u_l(R_{MT}) \dot{u}_l'(R_{MT})\right]. \quad (4.46)$$

4.4.4 Brillouin zone integration for Fermi energy and Fermi surface energy

The Brillouin zone integrations are involved many times during the self-consistent loop procedure. They are used to calculate the electron density, the total energy or the sum of eigenvalues. All these physical quantities depend on the Bloch vector and the energy band. These integrations are performed over the region of the Brillouin zone where the band energy $\varepsilon_\nu(\mathbf{k})$ is lower than the Fermi energy. Hence these integrals are of the form:

$$\frac{1}{V_{BZ}} \int_{BZ} \sum_{\nu\{\varepsilon_\nu(\mathbf{k}) \leq E_F\}} f_\nu(\mathbf{k}) d^3k, \quad (4.47)$$

where f is the function to be integrated.
Usually the special points method [63] is used to integrate a smoothly varying periodic functions of $\mathbf{k}$. The function to be integrated have to be calculated at a set of special points in the IBZ, each of which is assigned a weight according to the employed point group symmetry. Thus, the BZ integration is transformed into a sum over a set of $\mathbf{k}$-points:

$$\sum_{\mathbf{k} \in IBZ} \sum_{\nu\{\varepsilon_\nu(\mathbf{k}) \leq E_F\}} f_\nu(\mathbf{k}) w(\mathbf{k}), \quad (4.48)$$

where the function $f_\nu(\mathbf{k})$ is now a product of the function f (to be integrated) with a step function[9] that cuts out the region of the Brillouin zone, i.e., the band energies are below the Fermi energy. In the implementation of the FLAPW method, the Fermi energy is determined in two steps. First, the bands are occupied starting from the lowest energy until the sum of their weights equals the total number of electrons per unit cell, i.e., the discretized equivalent of equation (4.47) is solved at $T = 0$. Then, the step function is replaced by the Fermi function and the Fermi energy is determined from the requirement that:

$$N = \sum_{\mathbf{k}} \sum_{\nu} w(\mathbf{k}, \varepsilon_\nu(\mathbf{k}) - E_F), \quad (4.49)$$

where the weights are given by:

$$w(\mathbf{k}, \varepsilon_\nu(\mathbf{k}) - E_F) = w(\mathbf{k}) \frac{1}{e^{\frac{\varepsilon_\nu(\mathbf{k}) - E_F}{k_B T}} + 1}, \quad (4.50)$$

[9] This step function is replaced by the Fermi function $\frac{1}{e^{\frac{\varepsilon_\nu(\mathbf{k}) - E_F}{k_B T}} + 1}$ to account for the so-called temperature broadening and avoid the problem of the sudden (sharp differentiation) variations of the integrand during the iterations. This is happening usually for bands very close to the Fermi energy.

and N is the total electrons number.
The weights $w(\mathbf{k},\varepsilon_\nu(\mathbf{k}) - E_F)$ are stored to be used for later Brillouin zone integrations. The Fermi surface energy calculation method we have implemented (paper I) is based on a linear tetrahedron method [64].
Metallic materials are characterized by a number of partially filled bands. In such systems the energy of the highest occupied level, the Fermi energy E_F, lies within the energy range of one or more bands. For each partially filled band there will be a surface in **k**-space, separating the occupied levels from the unoccupied ones. The set of all such surfaces is known as the Fermi surface. In a first step, a reciprocal equispaced grid is defined. The next step consists of dividing each submesh cell into a six tetrahedra of equal volume. These tetrahedra are, therefore, selected according to the range of the corresponding eigenenergies[10]. Figure (4.3) shows the different contributions to the calculated Fermi

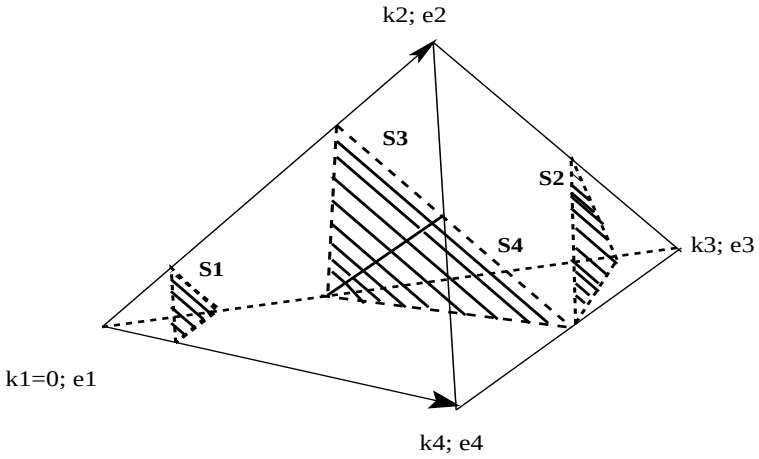

Figure 4.3: One of the six tetrahedron of a submesh cubic cell. To each reciprocal space corner ($\mathbf{k}_1$, $\mathbf{k}_2$, $\mathbf{k}_3$ and $\mathbf{k}_4$) corresponds an eigenvalue (ε_1, ε_2, ε_3 and ε_4). The different contributions to the Fermi surface are presented as hatched planes (notice that only one possibility out of three may occur for each tetrahedron).

surface energy. Using a linear interpolation of $\varepsilon(\mathbf{k})$ and arranging the eigenvalues as $\varepsilon_1 < \varepsilon_2 < \varepsilon_3 < \varepsilon_4$, these contributions can be enumerated as:

1. If $\varepsilon_1 < \varepsilon_F < \varepsilon_2 < \varepsilon_3 < \varepsilon_4$ the calculated contribution to the Fermi surface is the hatched surface $\mathbf{S}_1$ (see figure (4.3)).

2. If $\varepsilon_1 < \varepsilon_2 < \varepsilon_3 < \varepsilon_F < \varepsilon_4$ the calculated contribution to the Fermi surface is the hatched surface $\mathbf{S}_2$.

3. If $\varepsilon_1 < \varepsilon_2 < \varepsilon_F < \varepsilon_3 < \varepsilon_4$ the corresponding contribution is the sum of the $\mathbf{S}_3$ and $\mathbf{S}_4$ surfaces.

The surface areas calculations are provided in Appendix (A).

[10] If the corresponding eigenvalues (ε_1, ε_2, ε_3 and ε_4) lie around the Fermi energy, this means that these tetrahedron should be crossed, in the reciprocal space, by the Fermi surface.

4.4.5 Construction of the electron density

Once the diagonalization of the Hamiltonian is achieved, the resulting eigenfunctions can be used to determine the charge density. The electron density is given by an integral over the Brillouin zone (cf. equation (4.47)):

$$n(\mathbf{r}) = \frac{1}{V_{BZ}} \int_{BZ} \sum_{\nu\{\varepsilon_\nu(\mathbf{k})<E_F\}} |\psi_\nu(\mathbf{k},\mathbf{r})|^2 \, d^3k. \tag{4.51}$$

The summation includes also the spin-index σ for spin-polarized calculations, while a factor "2" has to be added to account for the spin degeneracy. This integration has to be transformed into a weighted sum over the **k**-points in order to sample the eigenfunctions, where the choice of **k**-points and their weights depend on the integration method used. These weights depend not only on the **k**-points but also on the band energy, because each band contributes to the electron density only if its energy is below the Fermi energy:

$$n(\mathbf{r}) = \sum_{\mathbf{k}} \sum_{\nu} |\psi_\nu(\mathbf{k},\mathbf{r})|^2 \, w(\mathbf{k}, \varepsilon_\nu(\mathbf{k}) - E_F). \tag{4.52}$$

Within the FLAPW method the eigenfunctions are presented in terms of the coefficients of the augmented plane waves:

$$\psi_\nu(\mathbf{k},\mathbf{r}) = \sum_{\mathbf{G}} C_\nu^{\mathbf{G}}(\mathbf{k}) \varphi_{\mathbf{G}}(\mathbf{k},\mathbf{r}). \tag{4.53}$$

Inside the muffin-tin spheres each plane wave is coupled to a sum of spherical harmonics and radial functions. Hence, in a sphere μ an eigenfunction is given by:

$$\psi_\nu(\mathbf{k},\mathbf{r}) = \sum_{\mathbf{G}} C_\nu^{\mathbf{G}}(\mathbf{k}) \sum_{lm} (A_{lm}^{\mu\mathbf{G}}(\mathbf{k}) u_l(r) + B_{lm}^{\mu\mathbf{G}}(\mathbf{k}) \dot{u}_l(r)) Y_{lm}(\hat{\mathbf{r}}). \tag{4.54}$$

By performing a contraction over the plane waves, this equation becomes:

$$\psi_\nu(\mathbf{k},\mathbf{r}) = \sum_{lm} (A_{lm}^{\mu}(\mathbf{k}) u_l(r) + B_{lm}^{\mu}(\mathbf{k}) \dot{u}_l(r)) Y_{lm}(\hat{\mathbf{r}}), \tag{4.55}$$

where

$$A_{lm}^{\mu}(\mathbf{k}) = \textstyle\sum_{\mathbf{G}} C_\nu^{\mathbf{G}}(\mathbf{k}) A_{lm}^{\mu\mathbf{G}}(\mathbf{k}) \quad , \quad B_{lm}^{\mu}(\mathbf{k}) = \sum_{\mathbf{G}} C_\nu^{\mathbf{G}}(\mathbf{k}) B_{lm}^{\mu\mathbf{G}}(\mathbf{k}). \tag{4.56}$$

Construction of the electron density in the muffin-tins

Substituting equation (4.55) into equation (4.51) yields the electron density in the muffin-tin spheres:

$$n^\mu(\mathbf{r}) = \frac{1}{V_{BZ}} \int_{BZ} \sum_{\nu,\varepsilon_\nu(\mathbf{k})<E_F} \sum_{l'm'} (A_{l'm'}^{\mu}(\mathbf{k}) u_{l'}(r) + B_{l'm'}^{\mu}(\mathbf{k}) \dot{u}_{l'}(r))^* Y_{l'm'}^*(\hat{\mathbf{r}}) \cdot \sum_{lm} (A_{lm}^{\mu}(\mathbf{k}) u_l(r) + B_{lm}^{\mu}(\mathbf{k}) \dot{u}_l(r)) Y_{lm}(\hat{\mathbf{r}}) \mathbf{d^3k}. \tag{4.57}$$

The particle density inside the muffin-tins is also expanded into spherical harmonics:

$$n^\mu(\mathbf{r}) = \sum_{lm} C_{lm}^{\mu}(r) Y_{lm}(\hat{r}). \tag{4.58}$$

The coefficients $C^{\mu}_{l''m''}(\hat{r})$ can be determined by multiplying equation (4.57) with $\int d\Omega Y_{l''m''}(\hat{r})$:

$$C^{\mu}_{l''m''} = \frac{1}{V_{BZ}} \int_{BZ} \sum_{\nu,\varepsilon_\nu(\mathbf{k})<E_F} \sum_{l'm'} (A^{\mu}_{l'm'}(\mathbf{k}) u_{l'}(r) + B^{\mu}_{l'm'}(\mathbf{k}) \dot{u}_{l'}(r))^* \cdot \sum_{lm} (A^{\mu}_{lm}(\mathbf{k}) u_l(r) + B^{\mu}_{lm}(\mathbf{k}) \dot{u}_l(r)) G^{mm'm''}_{ll'l''} d^3k, \tag{4.59}$$

where the Gaunt coefficients ($G^{mm'm''}_{ll'l''}$) are used as reals. Finally, applying a Brillouin zone integration method yields:

$$C^{\mu}_{l''m''} = \sum_{l'l} \left(\sum_{\mathbf{k}} \sum_{\nu} \sum_{m'm} (A^{\mu}_{l'm'}(\mathbf{k}))^* A^{\mu}_{lm}(\mathbf{k}) G^{mm'm''}_{ll'l''} w(\nu, \mathbf{k}) \right) u_{l'}(r) u_l(r) + \ldots A^*B + B^*A + B^*B \ldots. \tag{4.60}$$

Construction of the electron density in the interstitial region

In the interstitial region the wave functions are represented in the following form:

$$\psi_\nu(\mathbf{k}, \mathbf{r}) = \sum_{\mathbf{G}} \mathbf{C}^{\mathbf{G}}_{\nu}(\mathbf{k}) \mathbf{e}^{\mathbf{i}(\mathbf{G}+\mathbf{k})\mathbf{r}}. \tag{4.61}$$

Starting from equation (4.51) the electron density is expressed as:

$$n(\mathbf{r}) = \frac{1}{V_{BZ}} \int_{BZ} \sum_{\nu,\varepsilon_\nu(\mathbf{k})<E_F} \sum_{\mathbf{G'G''}} \left(C^{\mathbf{G'}}_{\nu}(\mathbf{k}) \right)^* C^{\mathbf{G''}}_{\nu}(\mathbf{k}) e^{i(\mathbf{G''}-\mathbf{G'})\mathbf{r}} d^3k. \tag{4.62}$$

The electron density in the interstitial region is also expanded into plane waves:

$$n(\mathbf{r}) = \sum_{\mathbf{G}} n^{\mathbf{G}} e^{i\mathbf{G}\mathbf{r}}. \tag{4.63}$$

Hence, the plane wave coefficients of the electron density are:

$$n^{\mathbf{G}} = \frac{1}{V_{BZ}} \int_{BZ} \sum_{\nu,\varepsilon_\nu(\mathbf{k})<E_F} \sum_{\mathbf{G'G''},\mathbf{G''}-\mathbf{G'}=\mathbf{G}} \left(C^{\mathbf{G'}}_{\nu}(\mathbf{k}) \right)^* C^{\mathbf{G''}}_{\nu}(\mathbf{k}) d^3k. \tag{4.64}$$

Therefore the $\mathbf{k}$ and state dependent density is given by the momentum space convolution:

$$n^{\mathbf{G}}_{\nu}(\mathbf{k}) = \sum_{\mathbf{G'G''},\mathbf{G''}-\mathbf{G'}=\mathbf{G}} \left(C^{\mathbf{G'}}_{\nu}(\mathbf{k}) \right)^* C^{\mathbf{G''}}_{\nu}(\mathbf{k}) = \sum_{\mathbf{G'}} \left(C^{\mathbf{G'}}_{\nu}(\mathbf{k}) \right)^* C^{\mathbf{G}+\mathbf{G'}}_{\nu}(\mathbf{k}) \tag{4.65}$$

For each coefficient, a sum over $\mathbf{G}$ has to be performed. Consequently, the numerical effort put into the determination of $n^{\mathbf{G}}_{\nu}(\mathbf{k})$ scales proportional to the number of $\mathbf{G}$-vectors squared, i.e., proportional to $(G_{max})^6$. However, $n^{\mathbf{G}}_{\nu}(\mathbf{k})$ can be calculated using the fast Fourier transform (FFT)[11].

[11] This can be done at a $(G_{max})^3 \ln(G_{max})^3$ numerical effort cost instead of $(G_{max})^6$. First, $C^{\mathbf{G}}_{\nu}(\mathbf{k})$ is Fourier transformed to the real space, where it is squared on a real space mesh yielding $n_\nu(\mathbf{k}, \mathbf{r})$, then all states are summed up, and finally the resulting particle density is back-transformed to the momentum space.

$$C^{\mathbf{G}}_{\nu}(\mathbf{k}) \xrightarrow{FFT} \psi_\nu(\mathbf{k}, \mathbf{r}) \xrightarrow{square} n_\nu(\mathbf{k}, \mathbf{r}) \xrightarrow{\sum_\nu} n(\mathbf{k}, \mathbf{r}) \xrightarrow{FFT^{-1}} n^{\mathbf{G}}(\mathbf{k}). \tag{4.66}$$

In a last step the plane waves have to be combined in order to form the three dimensional stars.

4.5 The LDA(GGA)+U approach within the FLAPW

The LDA(GGA)+U implementation within the FLAPW method follows the same logic as explained in section (3.7). The variational LDA(GGA)+U Schrödinger equations are those of equations (3.55):

$$\left[\nabla^2 + V^{\sigma}_{LDA}(\mathbf{r})\right]\psi^{\sigma}_{\mathbf{k},\nu}(\mathbf{r}) + \sum_{m_1,m_2} V^{\sigma}_{m_1,m_2}\frac{\delta n^{\sigma}_{m_1,m_2}}{\delta\psi^{\sigma}_{\mathbf{k},\nu}} = \varepsilon^{\sigma}_{\mathbf{k},\nu}\psi^{\sigma}_{\mathbf{k},\nu}(\mathbf{r}), \tag{4.67}$$

where $V^{\sigma}_{LDA}(\mathbf{r})$ is the LSDA or GGA potential calculated using the LDA(GGA)+U charge density:

$$\begin{array}{rcl} n^{\sigma}_{m_1 m_2} & = & \sum_{\mathbf{k},\nu} w(\nu,\mathbf{k})\left[A_{lm_1}(\mathbf{k})A^{*}_{lm_2}(\mathbf{k}) + \langle \dot{u}^{\sigma}_l|\dot{u}^{\sigma}_l\rangle B_{lm_1}(\mathbf{k})B^{*}_{lm_2}(\mathbf{k})\right]; \\ A_{lm}(\mathbf{k}) & = & \langle u^{\sigma}_l Y_{lm}|\psi^{\sigma}_{\mathbf{k},\nu}\rangle\ ,\ B_{lm}(\mathbf{k}) = \langle \dot{u}^{\sigma}_l Y_{lm}|\psi^{\sigma}_{\mathbf{k},\nu}\rangle. \end{array} \tag{4.68}$$

and (cf. equation (4.69)):

$$\begin{aligned} V^{\sigma}_{m_1,m_2} = \sum_{m_3,m_4}^{\sigma'} & (\langle m_1,m_3|V^{ee}|m_2,m_4\rangle - \langle m_1,m_3|V^{ee}|m_2,m_4\rangle\delta_{\sigma,\sigma'})n^{-\sigma'}_{m_3,m_4} \\ & -\delta_{m_1,m_2}U(n-\frac{1}{2}) + \delta_{m_1,m_2}J(n^{\sigma}-\frac{1}{2}). \end{aligned} \tag{4.69}$$

The last term of the variational Hamiltonian is calculated from equation (4.68):

$$\begin{aligned} \frac{\delta n^{\sigma}_{m_1,m_2}}{\delta\psi^{\sigma}_{\mathbf{k},\nu}} &= \langle\psi^{\sigma}_{\mathbf{k},\nu}|u^{\sigma}_l Y_{lm_2}\rangle u^{\sigma}_l Y_{lm_1} + \langle\dot{u}^{\sigma}_l|\dot{u}^{\sigma}_l\rangle\langle\psi^{\sigma}_{\mathbf{k},\nu}|\dot{u}^{\sigma}_l Y_{lm_2}\rangle\dot{u}^{\sigma}_l Y_{lm_1} \\ &= \left[|u^{\sigma}_l Y_{lm_1}\rangle\langle u^{\sigma}_l Y_{lm_2}| + \langle\dot{u}^{\sigma}_l|\dot{u}^{\sigma}_l\rangle|\dot{u}^{\sigma}_l Y_{lm_1}\rangle\langle\dot{u}^{\sigma}_l Y_{lm_2}|\right]\psi^{\sigma}_{\mathbf{k},\nu}. \end{aligned} \tag{4.70}$$

The U intra-atomic Coulomb interaction and the J exchange interaction can be calculated according to equations (3.58) within an unscreened atomic formulation. Within the Fleur implementation [25], these interactions are considered as a parameters, and they are usually extracted from experimental results.

Chapter 5

Spin-orbit coupling and the magnetic anisotropy

In a ferromagnetic material, below the Curie temperature, the total energy is found to be dependent on the orientation of the magnetization. This is usually what is meant by the magnetocrystalline anisotropy in the literature. Two principle magnetic mechanisms are responsible for such phenomena. One is the dipole-dipole interaction between the moments localized at different lattice points [65, 66, 67]. The second one is related to the orientation of the spin axis and is of pure relativistic character appearing only when the spin-orbit interaction is taken into account [68]. The spin-orbit coupling (SOC) provides the mechanism that couples the spin moment to the crystal generating thereby a dependence of the energy from the spin axis.

5.1 The Kohn-Sham-Dirac equation

Relativistic effects are important for the correct description of core or valence electrons. Both core and valence electrons have finite wave functions near the nucleus, where the kinetic energy is large. This kinetic energy becomes more significant for heavier elements and compounds. Additionally, only relativistic effects, in particular the spin-orbit coupling, introduce a link between spatial and spin coordinates. Thus, information about the orientation of spins relative to the lattice can only be gained if relativity is taken into account. For fully relativistic description of the electronic structure all relativistic effects, i.e., mass-velocity, Darwin-term, spin-orbit coupling, have to be taken into account [69]. However, in many applications an approximation is used, where the spin-orbit coupling is neglected. This approximation is called the scalar relativistic approximation. It consists in including the spin-orbit interaction additionally[1], either self-consistently or with the use of Andersen's force theorem [70].
In a relativistic density functional theory the Kohn-Sham equations have the form of a single particle Dirac equation

$$\{c\boldsymbol{\alpha}\cdot\mathbf{p}+(\beta-1)mc^2+V_{eff}(\mathbf{r})\}\boldsymbol{\Psi}=E\boldsymbol{\Psi}, \tag{5.1}$$

$$\boldsymbol{\alpha}=\left(\begin{pmatrix}0&\sigma_x\\\sigma_x&0\end{pmatrix},\begin{pmatrix}0&\sigma_y\\\sigma_y&0\end{pmatrix},\begin{pmatrix}0&\sigma_z\\\sigma_z&0\end{pmatrix}\right)^{\mathrm{tr}}=\begin{pmatrix}0&\boldsymbol{\sigma}\\\boldsymbol{\sigma}&0\end{pmatrix}, \tag{5.2}$$

$$\beta=\begin{pmatrix}\mathbf{I}_2&0\\0&-\mathbf{I}_2\end{pmatrix}. \tag{5.3}$$

[1] This is known as the second variational scheme.

σ_x, σ_y, and σ_z are the three components of the Pauli matrix vector $\boldsymbol{\sigma}$, $\mathbf{p}$ is the momentum operator, and $\mathbf{I}_n$ is the $(n \times n)$ unit matrix. V_{eff} is the effective potential, that contains electron-nucleon Coulomb potential, Hartree potential and exchange-correlation potential. In the case of spin-polarization, V_{eff} is spin-dependent. Finally, $\boldsymbol{\Psi}$ is the relativistic four component wave function.
The straightforward way to solve this problem would be to expand each of the four components of $\boldsymbol{\Psi}$ in terms of the FLAPW basis. However, if all four components were treated with the same accuracy, this would result in a basis set which contains four times as many functions as in the non-relativistic (non-magnetic) case.
The FLAPW implementation we use introduces some approximations to make relativistic calculations more efficient. One of these approximations is the scalar relativistic approximations, which has been suggested by D.D. Koelling and B.N. Harmon [71], where the spin-orbit term is neglected, and spin and spatial coordinates become decoupled. Hence, the Hamiltonian matrix reduces to two matrices of half the size, which can be diagonalized separately. This saves a factor of four in computing time. The scalar relativistic approximation will be discussed more detailed in the next section. It should be noted that relativistic effects are only significant close to the nucleus, where the kinetic energy is large. It is therefore reasonable to treat the interstitial region non-relativistically. Thus, merely within the muffin-tin spheres the electrons are treated relativistically. Moreover, only the large component of $\boldsymbol{\Psi}$ is matched to the non-relativistic wave functions at the boundary between the muffin-tins and the interstitial region, because the small component is already negligible at this distance from the nucleus. The small component is attached to the large component, and cannot be varied independently. However, this is a somewhat sensible approximation for two reasons: Firstly even inside the muffin-tin sphere the large component is still much bigger than the small component, and plays an important role, and secondly the two components are determined by solving the scalar relativistic equations for the spherically averaged potential. Therefore, they are very well suited to describe the wave functions.
Hence, the size of the basis set and the Hamiltonian matrix remains the same as in non-relativistic calculations, but the problem has to be solved twice, once for each direction of spin. This numerical effort is equal to that needed in spin-polarized non-relativistic calculations.

5.2 The scalar relativistic approximation

As it was pointed out in the previous section, the electrons are only treated relativistically inside the muffin-tin spheres. Thus the first problem that has to be addressed is the construction of the radial function. This is done by solving the scalar relativistic equation, including only the spherically averaged part of the potential. The starting point is the following Dirac equation:

$$\{c\boldsymbol{\alpha} \cdot \mathbf{p} + (\beta - 1)mc^2 + V(\mathbf{r})\}\boldsymbol{\Psi} = E\boldsymbol{\Psi}. \tag{5.4}$$

The solution of equation (5.4) is discussed in many textbooks, e.g., E.M. Rose [72]. Due to the spin-orbit coupling m_l and m_s are not good numbers any more, and they have to be replaced by the quantum numbers κ and μ (or j and μ), which are eigenvalues of the operators K and the z-component of the total angular momentum j_z (or the total angular momentum $\mathbf{j}$ and j_z) respectively. K is defined by

$$K = \beta(\boldsymbol{\sigma} \cdot \mathbf{l} + 1). \tag{5.5}$$

The solution of equation (5.4) have the form

$$\Psi = \Psi_{\kappa\mu} = \begin{pmatrix} g_\kappa(r)\chi_{\kappa\mu} \\ if_\kappa(r)\chi_{-\kappa\mu} \end{pmatrix}, \tag{5.6}$$

where $g_\kappa(r)$ is the large component, $f_\kappa(r)$ is the small component, $\chi_{\kappa\mu}$ and $\chi_{-\kappa\mu}$ are spin angular functions, which are eigenfunctions of $\mathbf{j}$, j_z, K, and $\mathbf{s}^2$ with eigenvalues j, μ, κ $(-\kappa)$ and s=1/2 respectively. The spin angular functions can be expanded into a sum of products of spherical harmonics and Pauli spinors, where the expansion coefficients are the Clebsh-Gordan coefficients. The radial functions have to satisfy the set of coupled equations:

$$\begin{pmatrix} -\frac{\kappa+1}{r} - \frac{\partial}{\partial r} & 2Mc \\ \frac{1}{c}(V(r)-E) & \frac{\kappa-1}{r} - \frac{\partial}{\partial r} \end{pmatrix} \begin{pmatrix} g_\kappa(r) \\ f_\kappa(r) \end{pmatrix} = 0, \tag{5.7}$$

with

$$M = m + \frac{1}{2c^2}(E - V(r)). \tag{5.8}$$

To derive the scalar relativistic approximation D.D. Koelling and B.N. Harmon [71] have introduced the following transformation:

$$\begin{pmatrix} g_\kappa(r) \\ \phi_\kappa(r) \end{pmatrix} = \begin{pmatrix} 1 & 0 \\ \frac{1}{2Mc}\frac{\kappa+1}{r} & 1 \end{pmatrix} \begin{pmatrix} g_\kappa(r) \\ f_\kappa(r) \end{pmatrix}. \tag{5.9}$$

Using this transformation equation (5.7) becomes

$$\begin{pmatrix} -\frac{\partial}{\partial r} & 2Mc \\ \frac{1}{2Mc}\frac{l(l+1)}{r^2} + \frac{1}{c}(V(r)-E) + \frac{\kappa+1}{r}\frac{M'}{2M^2c} & -\frac{2}{r} - \frac{\partial}{\partial r} \end{pmatrix} \begin{pmatrix} g_\kappa(r) \\ \phi_\kappa(r) \end{pmatrix} = 0, \tag{5.10}$$

where M' denotes the radial derivative of M $(\frac{\partial M}{\partial r})$, and the identity $\kappa(\kappa+1) = l(l+1)$ has been used. Since κ is the eigenvalue of $K = \beta(\boldsymbol{\sigma}\cdot\mathbf{l}+1)$ the term $\frac{(\kappa+1)M'}{2M^2cr}$ can be identified as the spin-orbit term. This term is dropped in the scalar relativistic approximation, because it is the only one, that causes coupling of spin up and spin down contributions. The radial functions $g_l(r)$ and $\phi_l(r)$ (the index κ has been replaced by l) can now be calculated from the following differential equations:

$$\frac{\partial}{\partial r} g_l(r) = 2Mc\phi_l(r), \tag{5.11}$$

$$\frac{\partial}{\partial r}\phi_l(r) = \left(\frac{1}{2Mc}\frac{l(l+1)}{r^2} + \frac{1}{c}(V(r)-E)\right) g_l(r) - \frac{2}{r}\phi_l(r). \tag{5.12}$$

The energy derivative of these equations yields straightforwardly a set of equations for $\dot{g}_l(r)$ and $\dot{\phi}_l(r)$, which are the relativistic analog of $\dot{u}_l(r)$. For numerical reasons the functions $g_l(r)$ and $\phi_l(r)$ are replaced by $p_l(r) = rg_l(r)$ and $q_l(r) = cr\phi_l(r)$.

5.3 The spin-orbit coupling implementation within the FLAPW

In the present Fleur code implementation [25] of the FLAPW method the relativistic radial wave functions are normalized according to

$$\left\langle \begin{pmatrix} g_l(r) \\ \phi_l(r) \end{pmatrix} \middle| \begin{pmatrix} g_l(r) \\ \phi_l(r) \end{pmatrix} \right\rangle = \int_0^{R_{MT}} (g_l^2(r) + \phi_l^2(r))r^2 dr = 1. \tag{5.13}$$

The energy derivatives of the radial functions have to be made orthogonal to the radial functions:

$$\left\langle \begin{pmatrix} g_l(r) \\ \phi_l(r) \end{pmatrix} \middle| \begin{pmatrix} \dot{g}_l(r) \\ \dot{\phi}_l(r) \end{pmatrix} \right\rangle = 0. \tag{5.14}$$

So that the scalar relativistic FLAPW basis set takes the form

$$\varphi_{\mathbf{G}}(\mathbf{k},\mathbf{r}) = \begin{cases} e^{i(\mathbf{G}+\mathbf{k})\mathbf{r}} & \text{interstitial region} \\ \sum_{lm} \left(A_{lm}^{\mu\mathbf{G}}(\mathbf{k}) \begin{pmatrix} g_l(r) \\ \phi_l(r) \end{pmatrix} + B_{lm}^{\mu\mathbf{G}}(\mathbf{k}) \begin{pmatrix} \dot{g}_l(r) \\ \dot{\phi}_l(r) \end{pmatrix} \right) Y_{lm}(\hat{\mathbf{r}}) & \text{muffin-tin } \mu, \end{cases} \tag{5.15}$$

which is similar to that of a non-relativistic basis set (equation (4.10)).
Note that the Pauli-spinors have been omitted, since the spin-up and spin-down problems are solved independently within the scalar relativistic approximation. Ignoring the spin-orbit coupling term in equation (5.10) the scalar relativistic Hamiltonian including only the spherically averaged part of the potential can be expressed as:

$$H_{sp} \begin{pmatrix} g_l(r) \\ \phi_l(r) \end{pmatrix} = E \begin{pmatrix} g_l(r) \\ \phi_l(r) \end{pmatrix}, \tag{5.16}$$

with

$$H_{sp} = \begin{pmatrix} \frac{1}{2M}\frac{l(l+1)}{r^2} + V(r) & -\frac{2c}{r} - c\frac{\partial}{\partial r} \\ c\frac{\partial}{\partial r} & -2mc^2 + V(r) \end{pmatrix}. \tag{5.17}$$

Thus, the Hamiltonian will be set up and diagonalized in a similar manner to that of section (4.4.2).
In a *second* step, the spin-orbit coupling is calculated according to the following relation:

$$\hat{V}_{so}(r) = \frac{1}{2m^2c^2}\frac{\hbar}{2}\frac{1}{r}\frac{dV}{dr}\mathbf{L}.\boldsymbol{\sigma} = \begin{pmatrix} V_{so}^{\uparrow\uparrow} & V_{so}^{\uparrow\downarrow} \\ V_{so}^{\downarrow\uparrow} & V_{so}^{\downarrow\downarrow} \end{pmatrix}. \tag{5.18}$$

Therefore, the spin-orbit coupling of the two spin channels is related to the *unperturbed* potential[2] via the angular momentum operator $\mathbf{L}$ and the Pauli spin matrix $\boldsymbol{\sigma}$.
The 2×2 matrix form is written in spinor basis. The two spin directions are denoted $\uparrow$ and $\downarrow$. The derivation of the spin-orbit coupling angular part $\mathbf{L}.\boldsymbol{\sigma}$ is supplied in Appendix (B).
Finally the scalar relativistic Hamiltonian matrix elements will be constructed as:

$$H_{\nu,\nu'}^{\sigma,\sigma'}(\mathbf{k}) = \varepsilon_\nu(\mathbf{k})\delta_{\nu,\nu'}\delta_{\sigma,\sigma'} + \left\langle \psi_\nu(\mathbf{k},\mathbf{r}) \middle| \hat{V}_{so} \middle| \psi_{\nu'}(\mathbf{k},\mathbf{r}) \right\rangle, \tag{5.19}$$

where the corresponding eigenfunctions are of the form:

$$\mathbf{\Psi}_n(\mathbf{k},\mathbf{r}) = \sum_{\nu,\sigma} a_{\nu',\nu}^{\sigma}\psi_\nu(\mathbf{k},\mathbf{r}), \tag{5.20}$$

where $\psi_\nu(\mathbf{k},\mathbf{r})$ and $\varepsilon_\nu(\mathbf{k})$ are the eigenfunctions and the eigenvalues of the Hamiltonian (5.17) calculated without spin-orbit coupling, and n, ν are the band index. As it can be easily seen from equation (5.20) the n index should be twice that of ν because of the summation is carried out over both spins. This leads to a spin *mixing*[3] which makes this latter not a good quantum number.

[2]This is the spherical potential of equation (B.4) calculated without including the spin-orbit interaction.

[3]This effect results in a lifting of the Kramers degeneracy and can be observed in the band structure of typical magnetic metals.

5.4 Force-theorem applied to the magnetic anisotropy

One of the interesting aspects of the magnetism is that of the magnetic anisotropy. Indeed this anisotropy result from a complex interplay of the crystal and the magnetic degree of freedom. This interplay is a direct consequence of the spin-orbit coupling [68]. In $3d$ magnetic materials for example, the magnetocrystalline anisotropy energy (MAE) is found to be of about some μeV [73, 74] for bulk and up to some meV [75, 76] for surfaces and thin films. According to the Bruno [75] and van der Laan [77] models these small values of the MAE is a direct consequence of the tiny effect of the spin-orbit coupling. Given that so small spin-orbit coupling compared to the rest of the contributions to the Hamiltonian, this coupling can be treated as a perturbation in the same way that is explained in the previous section. In this respect, because of the computational effort saving gained by the force theorem [70] approximation many computational investigations [78, 79, 80] have been performed to explain the corresponding experimental results [81, 82]. These investigations have allowed a better understanding of the MAE of magnetic $3d$ based materials. However, magnetic $4f$ material anisotropy is only rarely studied. In order to get insight into the magnetic anisotropy in $4f$ rare-earth magnetic metals we have chosen to work with the gadolinium (Gd) materials. This choice was motivated by the interesting magnetic properties of Gd, especially its high spin magnetic moment.
The MAE is defined as the difference in energy:

$$MAE \equiv E(\text{hard axis}) - E(\text{easy axis}). \tag{5.21}$$

Sometimes, since the hard and easy axes are not known in advance the definition of the MAE is the one used in paper III, where, in a hcp crystal, we considered

$$MAE \equiv E(\text{a axis}) - E(\text{c axis}). \tag{5.22}$$

Further, one can define an anisotropy energy, or the energy dependence from the magnetization orientation, $E_A(\theta)$ as

$$E_A(\theta) \equiv E(\theta) - E(\text{ref. axis}), \tag{5.23}$$

where ref. axis indicates the axis chosen as reference (typically the easy axis or a symmetry axis of the crystal) and θ is the angle measured from it. The anisotropy energy can also be expanded as

$$E_A(\theta) = K_1 sin^2(\theta) + K_2 sin^4(\theta) + (K_3 + K_4 cos\phi) sin^6(\theta) + \dots \tag{5.24}$$

where K_i are the anisotropy constants, which are increasingly small.

5.5 The force theorem

The fact that the spin-orbit interaction can be introduced as a perturbation to scalar relativistic systems can be exploited in order to speed up the evaluation of the MAE. The way to do so is given by the force theorem for band structure calculations [70]. Let us consider an unperturbed system[4] with its total energy given by equation (3.19):

$$E = T_0[n(\mathbf{r})] + \int n(\mathbf{r}) \upsilon(\mathbf{r}) d^3r + \frac{e^2}{8\pi\epsilon_0} \int\int \frac{n(\mathbf{r}).n(\mathbf{r}')}{|\mathbf{r} - \mathbf{r}'|} d^3r d^3r' + E_{xc}[n(\mathbf{r})]. \tag{5.25}$$

[4]The perturbation will be, for our purposes the SOC, but, the theorem for more general.

By *switching on* a perturbation, one introduces a change in the total energy, to the first order in the charge density, δn, equal to

$$\begin{aligned}\delta E &= \delta T_0[n(\mathbf{r})] + \int \delta n(\mathbf{r}) \upsilon(\mathbf{r}) d^3r \\ &+ \frac{e^2}{4\pi\epsilon_0} \int\int \frac{n(\mathbf{r}).\delta n(\mathbf{r}')}{|\mathbf{r}-\mathbf{r}'|} d^3r d^3r' + \int \mu_{xc}[n(\mathbf{r})]\delta n(\mathbf{r}) d^3r + O(\delta n^2) \qquad (5.26) \\ &\equiv \delta T_0[n(\mathbf{r})] + \int V(\mathbf{r})\delta n(\mathbf{r}) d^3r + O(\delta n^2),\end{aligned}$$

where the change in the nuclei has been disregarded and the identities

$$E_{xc} \equiv \int \epsilon_{xc}[n(\mathbf{r})] n(\mathbf{r}) d^3r, \qquad (5.27)$$

$$\frac{\delta E_{xc}}{\delta n(\mathbf{r})} = V_{xc}(\mathbf{r}) = n(\mathbf{r}) \frac{\delta \epsilon_{xc}[n(\mathbf{r})]}{\delta n(\mathbf{r})} + \epsilon_{xc}[n(\mathbf{r})], \qquad (5.28)$$

$$V = \upsilon(\mathbf{r}) + V_H + V_{xc}, \qquad (5.29)$$

have been used. The last equality is that of the total Kohn-Sham potential of equation (3.17). According to equation (3.20) the kinetic energy can be rewritten in the form

$$T_0[n(\mathbf{r})] = \sum_i \epsilon_i - \int V(\mathbf{r}) n(\mathbf{r}) d^3r, \qquad (5.30)$$

therefore, its change is (also to the first order in the charge density change)

$$\delta T_0[n(\mathbf{r})] = \delta \sum_i \epsilon_i - \int \delta V(\mathbf{r}) n(\mathbf{r}) d^3r - \int V(\mathbf{r}) \delta n(\mathbf{r}) d^3r. \qquad (5.31)$$

Thus, if the potential is kept frozen, a substitution of equation (5.31) in (5.26), yields

$$\delta E = \delta \sum_i \epsilon_i, \qquad (5.32)$$

which is the force theorem we wanted to derive and is valid to order $O(\delta n)$. The reason why we wanted to show here the derivation of equation (5.32) is that it is interesting to see that some changes in the single contributions to the total energy are not zero but they partially cancel each other to first order.
Since the change in the total energy in a frozen potential is equal to just the change in the eigenvalue sum, one calculate this latter, less computationally demanding quantity[5], in order to obtain the former. A large number of evaluations of MAE via the force theorem in various elements and compounds have been carried out in the past 20 years [83, 84, 78, 85], showing that contributions of order $O(\delta n^2)$ are most often negligible and that the change in the eigenvalue sum is very close to the total energy change.

[5]Using the force theorem, a self-consistent calculations is performed without including the SOC. Since all one needs is the difference of the eigenvalues sum for two magnetization directions, one iteration would be sufficient to introduce the spin-orbit interaction.

5.6 The peculiar MAE of Gd

Gd metal is in the middle of the rare-earth (RE) series and its f-shell is half filled. This means that, in a Russel-Saunders (RS) scheme, no orbital moment is to be expected from the f-electron shell. Because of the sphericity of the $4f$ shell, one expects no crystal electric field (CEF) contribution to the anisotropy and indeed the MAE of Gd ($\sim 35\mu$ eV/atom) is two order of magnitude smaller than the MAE of other RE metals ($\sim$ meV/atom). The relevant question one may ask is therefore, where does the observed MAE of Gd originate from? In paper III we addressed this question and we found that this conduction band MAE is completely driven by the SOC band structure anisotropy (figure (5.1)). Our calculated anisotropy is found to be in excellent agreement with experiment [86], and can be explained by the Bruno model [75], according to which for spherical shell the magnetic anisotropy stems from the orbital magnetic moment anisotropy:

$$E_A(\theta) = \Delta E(\theta, 0^\circ) = -\frac{\xi}{4\mu_B}\left([\mu^{\uparrow}_{orb}(\theta) - \mu^{\downarrow}_{orb}(\theta)] - [\mu^{\uparrow}_{orb}(0^\circ) - \mu^{\downarrow}_{orb}(0^\circ)]\right), \tag{5.33}$$

where ξ is the spin-orbit parameter for $5d$ Gd orbitals and μ^{σ}_{orb} the orbital moment of the spin σ.
Our results make the classical dipole anisotropy contribution claimed by Colarieti-Tosti *et al.* [87, 88] doubtful. The force-theorem investigations of this work have shown that the Gd MAE stems from an interplay between the dipole interaction of the large localized $4f$ spin moments and the SOC conduction band MAE. This MAE was found to explain well the observed anisotropy energy [86], $E_A(\theta)$.

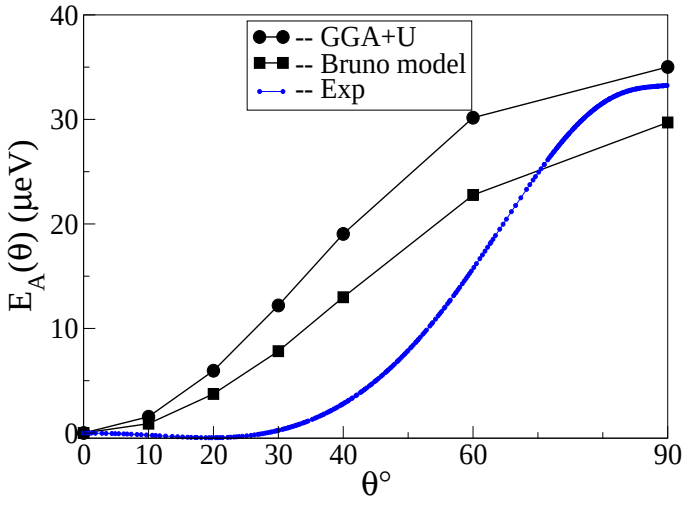

Figure 5.1: The force-theorem GGA+U calculated MAE (in black circles) and the Bruno model MAE (in black squares) compared to the experimental one [86].

Chapter 6

X-ray Magnetic Circular dichroism

6.1 History

Since the x-ray discovery by Röntgen [89] in 1895 a considerable attention and effort have been devoted to the use of the x-ray in different research areas. Some years after the finding of Röntgen, Bassler discovered the polarized character of this light as presented in his thesis: "*Polarization of x-rays evidenced with secondary radiation*" [90]. To go further in the understanding of this x-rays properties many experiments were set up to observe the interaction of light with magnetic materials [91] or non-magnetic materials with an external magnetic field, e.g., aluminium, carbon, copper, iron, nickel, platinum, zinc and silver [92]. The influence of the magnetism on x-ray absorption have then been investigated measuring the difference of the absorption (or the cross-section) rate between two different orientations of the magnetization. Unfortunately the tiny amount of this absorption difference rate has made the results of Bassler [90] questionable if not doubtful. The measurements recorded using the equipment of that time does not have a sufficient sensitivity [93] and have given rise to a long controversial debate [94, 95, 96, 97].
In 1983, G. Schütz and her colleagues [98] concentrated their efforts on the use of circularly polarized x-rays in order to elucidate the influence of the magnetic state of iron on x-ray absorption spectra. Again, the sensitivity of the experimental setup was not high enough to detect in this energy range any spin-dependent contribution to x-ray absorption. One year later, the attempt of Keller and Stern [99], despite of the use of a synchrotron radiation, has failed to reveal the dichroism of Gd in $Gd_{18}Fe_{82}$ alloy because the circular polarization rate of the incident x-rays was only 5%. Shortly later, the existence of x-ray magnetic circular dichroism (XMCD) was proved experimentally by Schütz *et al.* at the Fe K edge in an iron foil [100] and at the L edges of Gd in $Gd_3Fe_5O_{12}$ [101][1].
The first theoretical investigation of XMCD was performed by Erskine and Stern [103]. Unfortunately, very few people paid attention to their band structure calculation of XMCD at the $M_{2,3}$ absorption edges of ferromagnetic nickel. The most important finding from a theoretical point of view which marked the beginning of modern days for XMCD is that of Thole and coworkers [26, 27]. They considered a single ion electric dipole transitions model and derived a magneto-optical sum rules relating separately, integrated intensities of XMCD spectra to the ground-state orbital [26] and spin [27] moments. These sum rules provided experimentalists with a powerful tool to analyze XMCD spectra and to extract magnetic moments magnitudes and directions, with the full benefit of the element

[1] A more detailed Story of the XMCD can be found in the section entitled "*X-ray Magnetic Circular Dichroism: Historical Perspective And Recent Highlights*" by Andrei Rogalev *et al.*[102]

and orbital selectivity of x-ray absorption spectroscopy.

6.2 Theory

We have devoted this section to our implementation of XMCD calculations within the Fleur code. However, before presenting the theoretical background of this implementation it would be interesting to remind previous attempts to model, simulate and understand experimental dichroic x-ray absorption spectra.
The first theoretical investigations of XMCD are those of Thole *et al.* [104] who implemented an atomic multiplet approach [105]. This approach is based on an empirical atomic calculation. In addition to the absence of the hybridization effect this method (as all the others empirical methods) relies on the experimental spectra. Calculations applying this method to the $3d^9 4f^{n+1}$ multiplets of the $M_{4,5}$ edges of Lanthanides are summarized in the paper of Thole *et al.* [106]. Some years later Chen *et al.* [107] made use of the Erskine and Stern model[2] [103] for their experimental $L_{2,3}$ edges spectra of nickel. The disagreement between the measured branching ratio and that predicted by the model has been ascribed to the change of spin dependent unoccupied density of states near the Fermi level caused by the spin-orbit coupling effect. A year later the same group [108] published results of a tight-binding analysis in which they presented an attempt to include the spin-orbit coupling for d valence states. The valence spin-orbit ξ and exchange splitting Δ_{ex} parameters extracted from numerical experiments are found to be respectively larger and smaller than those of the ground-state to achieve an optimal agreement between the simulated and experimental spectra. Later Smith *et al.* [109] included properly the spin-orbit coupling within a tight binding scheme. The results for nickel are not too different from those of the previous calculation [108] but the parameters (ξ, Δ_{ex}) found for iron revealed the sensitivity of the XMCD spectra on the unfilled d band width. The discrepancies between the calculated and the experimental parameters were imputed to many-body effects, e.g., since the core hole is created, the $3d$ valence electrons will see a stronger attractive core potential and the spatial extent of their orbitals will contract. Consequently, relativistic effects such as the spin-orbit coupling will be stronger, and the exchange interaction among the first neighbors will be weaker.
The development of x-ray spectroscopy experiments probing the magnetic properties of a large variety of magnetic rare-earth materials and the growing interest of the scientific community toward their applications in media storage, strong magnets and the emerging field of spintronics have stimulated our XMCD calculations for these materials. The discovery of XMCD sum rules may be a powerful tool for understanding and characterizing magnetic properties.
In order to study the strongly localized magnetism of rare earth metals we have implemented the XMCD absorption within the dipolar approximation using polar geometry[3]. Before providing the corresponding theoretical background we will briefly discuss two much earlier magneto-optical (MO) effects which are, to some extent, related to XMCD. When the linearly polarized light beam penetrates a magnetized sample, the light will become elliptically polarized upon transmission as well as reflection. No matter whether the magnetization is present spontaneously or induced by an external magnetic field, these

[2] According to this model the large spin-orbit coupling of the core states and it's small value for valence states should allow us to treat these valence states without spin-orbit coupling.

[3] This configuration corresponds to the case where the magnetization direction is parallel to the wave vector of the x-ray beam.

phenomena are called the Faraday [110] and Kerr [111] effects.
The quantum mechanical understanding of the Kerr MO effect began as early as 1932 when Hulme [112] ascribed Kerr effect to the spin-orbit coupling (SOC).
The interaction of the electromagnetic radiation with a magnetic medium is described classically by Maxwell's equations [113]:

$$\nabla \times \mathbf{E} + \frac{\partial \mathbf{B}}{\partial t} = 0, \tag{6.1}$$

$$\nabla \cdot \mathbf{B} = 0, \tag{6.2}$$

$$\nabla \times \mathbf{H} - \frac{\partial \mathbf{D}}{\partial t} = \mathbf{J}, \tag{6.3}$$

$$\nabla \cdot \mathbf{D} = \rho, \tag{6.4}$$

where $\mathbf{D}$ is the electric displacement, which is related to the total electric field $\mathbf{E}$ caused in part by the polarization $\mathbf{P}$ of the medium:

$$\mathbf{D} = \epsilon_0 \mathbf{E} + \mathbf{P} = (1 + \chi_e)\epsilon_0 \mathbf{E} = \boldsymbol{\epsilon} \mathbf{E}, \tag{6.5}$$

and $\mathbf{B}$ is the magnetic induction, which is related to the macroscopic magnetic field $\mathbf{H}$ resulting from the magnetization $\mathbf{M}$:

$$\mathbf{B} = \mu_0(\mathbf{H} + \mathbf{M}) = (1 + \chi_m)\mu_0 \mathbf{H} = \boldsymbol{\mu} \mathbf{H}, \tag{6.6}$$

where ϵ_0 and μ_0 are the vacuum permittivity and the vacuum permeability, and χ_e and χ_m, are the electric and magnetic susceptibility respectively. According to Ohm's law the macroscopic current density $\mathbf{J}$ produced by an electric field $\mathbf{E}$ is given by:

$$\mathbf{J} = \boldsymbol{\sigma} \cdot \mathbf{E}. \tag{6.7}$$

Equations (6.5), (6.6), and (6.7) are known as the material equations. They are known such that because they characterize the *response functions of the medium to external excitations*: the dielectric constant $\boldsymbol{\epsilon}$, the magnetic permeability $\boldsymbol{\mu}$, and the electrical conductivity $\boldsymbol{\sigma}$. In general the dielectric constant is a function of both spatial and time variables that relates the displacement field $\mathbf{D}(\mathbf{r}, t)$ to the total electric field $\mathbf{E}(\mathbf{r}', t')$:

$$\mathbf{D}(\mathbf{r}, t) = \int \int_{-\infty}^{t} \boldsymbol{\epsilon}(\mathbf{r}, \mathbf{r}', t') \mathbf{E}(\mathbf{r}', t') dt' dr'. \tag{6.8}$$

In the following we neglect the spatial dependence of the dielectric constant and consider only its frequency dependence $\epsilon(\omega)$. Usually, the effect of the magnetic permeability $\boldsymbol{\mu}(\omega)$ on optical phenomena is small and we assume that $\boldsymbol{\mu}(\omega) = \mu_0 \mathbf{I}$ where $\mathbf{I}$ is a unit tensor. It should be stressed also that ϵ and μ may depend on the field strength. In such cases higher order terms in a Taylor expansion of the material parameters lead to appearance of the non-linear effects [114]. Using the material equations and Maxwell equations it can be easily shown that:

$$\boldsymbol{\epsilon} = \frac{1}{\epsilon_0}(1 + i\frac{\boldsymbol{\sigma}}{\omega}). \tag{6.9}$$

For simplicity let us consider a material of cubic structure with a magnetization $\mathbf{M}$ directed along z axis. Above the Curie temperature T_C the three components of the dielectric tensor are equal[4] so that

$$\boldsymbol{\epsilon}(\omega) = \epsilon \boldsymbol{I}. \tag{6.10}$$

[4]This is the case when the dielectric components are presented in the cubic principal axes. The principal axes are the classical analogue of the local frame axes in quantum mechanics.

When the magnetization $\mathbf{M}$ appears below T_C the symmetry is lower and $\boldsymbol{\epsilon}(\omega)$ becomes [115]

$$\boldsymbol{\epsilon}(\mathbf{M},\omega) = \begin{pmatrix} \epsilon_{xx} & \epsilon_{xy} & 0 \\ -\epsilon_{xy} & \epsilon_{xx} & 0 \\ 0 & 0 & \epsilon_{zz} \end{pmatrix}. \tag{6.11}$$

The remaining symmetry of the system depends on the orientation of the magnetization. The components of the dielectric tensor depend on the magnetization and satisfy the following Onsager relations

$$\epsilon_{i,j}(-\mathbf{M},\omega) = \epsilon_{j,i}(\mathbf{M},\omega), \tag{6.12}$$

where $i,j = x,y$ or z. These relations mean that the diagonal components of the dielectric tensor are even functions of $\mathbf{M}$, whereas the nondiagonal ones are odd functions of $\mathbf{M}$. In the lowest order in $\mathbf{M}$

$$\epsilon_{xy} \sim M,\ \epsilon_{zz} - \epsilon_{xx} \sim M^2. \tag{6.13}$$

In the absence of an external current ($\mathbf{J} = 0$) and free charges ($\rho = 0$) Maxwell equations reduce to

$$\nabla \times \mathbf{E} = -\mu_0 \frac{\partial \mathbf{H}}{\partial t}, \tag{6.14}$$

$$\nabla \times \mathbf{H} = \boldsymbol{\epsilon} \frac{\partial \mathbf{E}}{\partial t}. \tag{6.15}$$

After substitution of $\mathbf{E}$ and $\mathbf{H}$ in a form of plane waves

$$\mathbf{E} = \mathbf{E}_0 e^{[-i(\omega t - \mathbf{q}.\mathbf{r})]}, \tag{6.16}$$

$$\mathbf{H} = \mathbf{H}_0 e^{[-i(\omega t - \mathbf{q}.\mathbf{r})]}, \tag{6.17}$$

one arrives to a secular equation

$$\begin{pmatrix} N^2 - \epsilon_{xx} & -\epsilon_{xy} & 0 \\ \epsilon_{xy} & N^2 - \epsilon_{xx} & 0 \\ 0 & 0 & N^2 - \epsilon_{zz} \end{pmatrix} \begin{pmatrix} E_x \\ E_y \\ E_z \end{pmatrix} = 0, \tag{6.18}$$

where ω is the frequency, $\mathbf{q}$ is the wave vector of light and $\mathbf{N}$ is a unit vector directed along $\mathbf{q}$ ($N = \frac{q}{\omega}c$). When the light propagates along z direction, i.e., along M, $E_z = 0$, and one finds the eigenvalues

$$n_{\pm}^2 = \epsilon_{xx} \pm i\epsilon_{xy}. \tag{6.19}$$

This means that the normal modes of the light accounting for the response (the displacement field $\mathbf{D}$) to the plane-wave field ($\mathbf{E}$) are

$$D_+ = n_-^2(E_x + iE_y), D_- = n_+^2(E_x - iE_y), \tag{6.20}$$

i.e., a left and right polarized light wave with complex refractive indices of n_- and n_+, respectively.

6.2.1 Faraday effect

In 1845 Faraday discovered [110] that the polarization vector of linearly polarized light is rotated upon transmission through a sample of thickness l that is exposed to a magnetic field parallel to the propagation direction of the light. Indeed, in a ferromagnet the left-hand and right-hand circularly polarized lights (which my constitute a linearly polarized

light propagating along the z direction if they have the same amplitude) propagate generally with different refractive indices or different velocities c/n_- and c/n_+. When the two transmitted light waves are combined at the exit surface of the sample, they yield again a linearly polarized light, but its plane of polarization is rotated by the so-called Faraday angle θ_F given by [116]

$$\theta_F = \frac{\omega l}{2c} Re(n_+ - n_-). \tag{6.21}$$

The direction of the rotation depends on the relative orientation of the magnetization and the light propagation. If two circularly polarized waves attenuate at different rates, then after traveling through the sample, their relative amplitude change. Therefore the transmitted light becomes elliptically polarized, with an ellipticity

$$\eta_F = -\frac{\omega l}{2c} Im(n_+ - n_-). \tag{6.22}$$

The ellipticity η_F corresponds to the ratio of the minor to the major axes of the polarization ellipsoid, and is related to the magnetic circular dichroism, which is defined by the difference of the absorption coefficient μ between the right and left circularly polarized light

$$\Delta\mu(\omega) = \mu_+(\omega) - \mu_-(\omega) = -\frac{4\eta_F(\omega)}{l}. \tag{6.23}$$

6.2.2 Kerr Effect

About 30 years later, Kerr [111] observed that when linearly polarized light is reflected from a magnetic solid, its polarization plane (the major axis of the ellipse) also rotates over a small angle with respect to the incident light. Depending on the orientation of

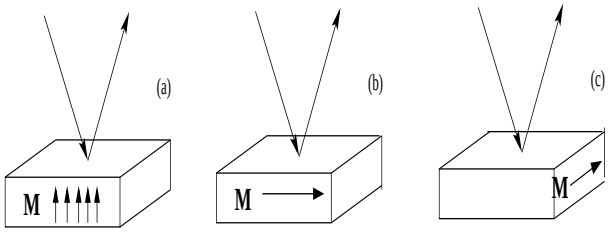

Figure 6.1: The different geometries for the MO Kerr effect: (a) the polar Kerr effect, (b) the longitudinal Kerr effect, (c) the transversal, or the equatorial Kerr effect .

the magnetization vector relative to the reflective surface and the plane of incidence of the light beam, three types of the magneto-optical effects in reflection are distinguished: polar, longitudinal, and transverse (equatorial) effects (figure (6.1). For linearly polarized incident light the reflected light will in general be elliptically polarized in the polar Kerr geometry (Fig. (6.1(a))). The relation between the complex polar Kerr angle and the complex refraction indices can be derived from the Fresnel relations and is given by [117]

$$\frac{1 + tan(\eta_K)}{1 - tan(\eta_K)} e^{2i\theta_K} = \frac{(1 + n_+)}{(1 - n_+)} \frac{(1 - n_-)}{(1 + n_-)}. \tag{6.24}$$

For most materials the Kerr rotation is less than 1 deg. For more detailed explanations for these effects and related results the reader is advised to see the chapter of reference [118].

6.2.3 The XMCD formalism

In the previous section the response of the medium to electromagnetic waves was described in a phenomenological manner in terms of the frequency dependent complex dielectric constant and conductivity. Within the linear response theory and using band structure methods Callaway and Wang [119, 120] have proposed a microscopic model for the calculations of the optical conductivity tensor

$$\sigma_{ij}(\omega) = \frac{ie^2}{m^2\hbar V}\sum_{\mathbf{k}}\sum_{\nu\nu'}\frac{(f(\epsilon_{\nu\mathbf{k}}) - f(\epsilon_{\nu'\mathbf{k}}))}{\left(\omega - \omega_{\nu\nu'(\mathbf{k})+\mathrm{i}\gamma}\right)}\frac{M^i_{\nu\nu'}(\mathbf{k})M^j_{\nu\nu'}(\mathbf{k})}{\omega_{\nu\nu'}(\mathbf{k})}. \tag{6.25}$$

It relates the macroscopic optical conductivity to the sum of interband transitions between Bloch states $\psi_{\nu\mathbf{k}}$ and $\psi_{\nu'\mathbf{k}}$ with energies $\epsilon_{\nu\mathbf{k}}$ and $\epsilon_{\nu'\mathbf{k}}$, where ν and ν' being the band indices, V the unit cell volume, $f(\epsilon_{\nu\mathbf{k}})$ the Fermi function, $\hbar\omega_{\nu\nu'}(\mathbf{k}) = \epsilon_{\nu\mathbf{k}} - \epsilon_{\nu'\mathbf{k}}$, and $\gamma = \frac{1}{\tau}$ is a phenomenological relaxation time parameter that takes into account the finite lifetime of the excited electronic states. $M^i_{\nu\nu'}(\mathbf{k})$ are the interband electronic transitions matrix elements which account for the probability of transition after an electron-photon interaction takes places. This matrix will be considered in more details later.
The real and imaginary parts $\sigma^{(1)}(\omega)$ and $\sigma^{(2)}(\omega)$ are related by the Kramers-Kronig relations [121] and can be determined separately. It is important to note that the relation (6.25) was derived for interband transitions, i.e., $\mathbf{q} = \mathbf{k} - \mathbf{k}'$=0. Usually the missing intraband contributions depend on lattice imperfections of the system as well as on the temperature. These contributions lie beyond the scope of our manuscript and are not considered.
In recent years the study of magneto-optical effects in the x-ray range has gained a great importance as a tool for the investigation of magnetic materials [122, 123]. The attenuation of the x-ray intensity when passing through a sample of thickness d is given by Beer's law:

$$I(d) = I_0 e^{-\mu_{\mathbf{q}\lambda}(\omega)d}, \tag{6.26}$$

where $\mu_{\mathbf{q}\lambda}(\omega)$ is the absorption coefficient which in general depends of the wave vector $\mathbf{q}$, the energy $\hbar\omega$, and the polarization λ of the radiation. In the x-ray regime the absorption coefficient $\mu_{\mathbf{q}\lambda}$ is related to the absorptive part of the dielectric function $\epsilon_{\mathbf{q}\lambda}$ or the optical conductivity $\sigma_{\mathbf{q}\lambda}$ via [122]

$$\mu_{\mathbf{q}\lambda}(\omega) = \frac{\omega}{c}\epsilon^{(2)}_{\mathbf{q}\lambda}(\omega) = \frac{4\pi}{c}\sigma^{(1)}_{\mathbf{q}\lambda}(\omega). \tag{6.27}$$

This means that $\mu_{\mathbf{q}\lambda}(\omega)$ can be evaluated[5] using equation (6.25):

$$\mu_{\mathbf{q}\lambda}(\omega) = \frac{\pi c^2}{\hbar\omega m V}\sum_{i}^{occ}\sum_{f}^{unocc}|M^{\mathbf{q}\lambda}_{if}|^2\delta(\hbar\omega - E_f + E_i). \tag{6.29}$$

In contrast to (6.25) in which the matrix elements of the electron-photon interaction are evaluated between two Bloch states, the matrix elements $M^{\mathbf{q}\lambda}_{if}$ are calculated between a

[5]Equation (6.29) can be considered as the limit of the real part of the matrix elements (equation (6.25)) when the frequency (ω) become too high (x-ray regime). In this case the frequency ω can be rewritten as $\omega = \omega_0 + \delta\omega$ because of the sharp energy of the involved core levels, and therefore

$$\frac{1}{\omega} = \frac{1}{\omega_0 + \delta\omega} \sim \frac{1}{\omega_0}. \tag{6.28}$$

This is why the factor $\frac{1}{\omega}$ is again present in equation (6.29).

well localized initial core state i and an extended final state f. The sum over initial states i is usually restricted to one core shell which could be achieved by an experimental fine-tuning of a particular absorption edge. This important property makes x-ray absorption an element specific probe.
The $M_{if}^{\mathbf{q}\lambda}$ transitions matrix accounts for the electron-photon interaction operator

$$\hat{H}_{el-ph} = -\frac{1}{c}\mathbf{J}\mathbf{A}_{\mathbf{q}\lambda}(\mathbf{r}) = -\frac{1}{c}\mathbf{J}\mathbf{e}_{\lambda}Ae^{i\mathbf{q}\mathbf{r}}, \tag{6.30}$$

where $\mathbf{A}_{\mathbf{q}\lambda}(\mathbf{r})$ is the vector potential with the wave vector $\mathbf{q}$ and polarization λ, $\mathbf{J}$ is the electronic current density operator

$$\mathbf{J} = -ec\boldsymbol{\alpha}, \tag{6.31}$$

and $\boldsymbol{\alpha}$ accounts for the electronic momentum operator[6]: $(\hbar/i)\boldsymbol{\nabla}$. The components of the polarization vector for linearly polarized light are given by

$$\mathbf{e}_x = \begin{pmatrix} 1 \\ 0 \\ 0 \end{pmatrix}, \mathbf{e}_y = \begin{pmatrix} 0 \\ 1 \\ 0 \end{pmatrix}, \mathbf{e}_z = \begin{pmatrix} 0 \\ 0 \\ 1 \end{pmatrix}. \tag{6.33}$$

For $\mathbf{q}$ pointing along the z axis, left (+) and right (-) circularly-polarized lights are presented by the polarization vector

$$\mathbf{e}_{\pm} = \frac{1}{\sqrt{2}} \begin{pmatrix} 1 \\ \pm i \\ 0 \end{pmatrix}. \tag{6.34}$$

In order to get insight into the corresponding absorption phenomena one needs to calculate matrix elements of the form

$$M_{if}^{\mathbf{q}\lambda} = \langle\psi_i|\hat{H}_{el-ph}|\psi_f\rangle. \tag{6.35}$$

It is generally argued that in the frequency range of conventional optics the amplitude of the vector potential varies only on a macroscopic scale. This implies that it is sufficient to expand the exponential factor in (6.30)

$$e^{i\mathbf{q}\mathbf{r}} = 1 + i\mathbf{q}\mathbf{r} - \frac{1}{2}(\mathbf{q}\mathbf{r})^2 \ldots, \tag{6.36}$$

and retain just the first constant term, in which case only the electric dipole interaction is accounted for. For x-ray regime (XMCD) the next term in the expansion that represents the quadripolar interaction may also be important. However, Arola *et al.* [124] showed that the contribution from the quadripolar interaction to the K edge cross sections of iron is two orders of magnitude smaller than that of the electric-dipole contribution. We have also shown that for bulk gadolinium (paper I) as well as for gadolinium compounds (paper II) (GdN) our dipolar XMCD calculations led to a good agreement with experiment without need for including the quadripolar contribution. Within the dipolar approximation the absorption coefficient reduces to

$$M_{if}^{\mathbf{q}\lambda} = \langle\psi_i|\boldsymbol{\alpha}\mathbf{e}_{\lambda}|\psi_f\rangle. \tag{6.37}$$

[6]Within the scalar-relativistic approximation (see section(5.2)) the total momentum operator is expressed as:

$$\alpha = \mathbf{p} + \frac{\hbar}{4mc^2}\boldsymbol{\sigma} \times \boldsymbol{\nabla}V = \frac{\hbar}{i}\boldsymbol{\nabla} + \frac{\hbar}{4mc^2}\boldsymbol{\sigma} \times \boldsymbol{\nabla}V, \tag{6.32}$$

while in the non-relativistic case ($c \to \infty$) this operator reduces to the electronic momentum operator.

The ec constant is deliberately omitted. It is worth mentioning that the symmetry reduction due to the presence of spontaneous magnetization, that leads to the appearance of nonzero off-diagonal components of the dielectric tensor, e.g. ϵ_{xy} in (6.18), occurs only if both the spin-polarization and the spin-orbit coupling are simultaneously taken into account in the calculations. Technically speaking, our FLAPW-XMCD calculations are performed in two steps. Firstly a good convergence is achieved (in term of total energy and charge density) within a scalar relativistic calculation where the SOC is included in a second variational way, after that one iteration is carried out in order to calculate the absorption coefficients using the electronic wave functions accounting for the supposed ground state. The initial core wave functions ψ_i are given by

$$\psi_i = \psi_{j\mu} = \sum_{m_{sc}} C^{j\mu}_{l_c\mu-m_{sc},\frac{1}{2}m_{sc}} u_{l_c}(r) Y_{l_c\mu-m_{sc}}(\hat{\mathbf{r}})\chi_{m_{sc}} = \sum_{m_{sc}} C^{j\mu}_{l_c m_c,\frac{1}{2}m_{sc}} u_{l_c}(r) Y_{l_c m_c}(\hat{\mathbf{r}})\chi_{m_{sc}}, \tag{6.38}$$

and the final wave functions ψ_f states are the dispersive ($\mathbf{k}$-dependent) FLAPW valence wave functions

$$\psi_f = \psi_\nu(\mathbf{k}, r) = \sum_{m_s}\sum_{lm}(A_{lm}(\mathbf{k})u_l(r)Y_{lm}(\hat{\mathbf{r}}) + B_{lm}(\mathbf{k})\dot{u}_l Y_{lm}(\hat{\mathbf{r}}))\chi_{ms}, \tag{6.39}$$

where χ_{sc}, χ_s, m_{sc}, and m_s are the core spin functions, the valence spin functions, the corresponding magnetic quantum numbers respectively. $C^{j\mu}_{l_c\mu-m_s,\frac{1}{2}}$ are the Clebsh-Gordan coefficients, j is the total momentum of the electron, l_c and l are the core and valence angular momentum quantum numbers, μ (or m_j) and m are the corresponding magnetic quantum numbers. The core and valence states are calculated separately and in a different way, that is to say that the core wave functions corresponding to deep energy levels are determined within a fully relativistic calculation while valence eigenfunctions are evaluated within a scalar relativistic calculation including the SOC as a perturbation (second variation approximation). Let us consider one edge transitions involving the initial j states and the final l states. The $M^{\mathbf{q}\lambda}_{if}$ matrix can be rewritten as

$$M^{\mathbf{q}\lambda}_{if} = M^{\mathbf{q}\lambda}_{j\mu}(\mathbf{k}) =$$

$$\sum_{m,m_s,m_{sc}} C^{j\mu}_{l_c m_c,\frac{1}{2}m_{sc}} \langle u_{l_c}(r)Y_{l_c m_c}(\hat{\mathbf{r}})|\boldsymbol{\alpha}\mathbf{e}_\lambda|(A_{lm}(\mathbf{k})u_l(r)Y_{lm}(\hat{\mathbf{r}}) + B_{lm}(\mathbf{k})\dot{u}_l Y_{lm}(\hat{\mathbf{r}}))\rangle\delta_{m_{sc}m_s}. \tag{6.40}$$

Using the relation

$$\boldsymbol{\alpha}\mathbf{e}_\lambda = \frac{\mathbf{e}_r.\mathbf{e}_\lambda}{i}\frac{\partial}{\partial r} - \frac{1}{r}(\mathbf{e}_r \times \mathbf{L}).\mathbf{e}_\lambda, \tag{6.41}$$

where $\mathbf{L}$ is the orbital angular momentum operator, equation (6.40) becomes

$$\begin{aligned} M^{\mathbf{q}\lambda}_{j\mu}(\mathbf{k}) \;=\; & \sum_{m,m_s} C^{j\mu}_{l_c m_c,\frac{1}{2}m_s} \left(\left\langle u_{l_c}(r)Y_{l_c m_c}(\hat{\mathbf{r}}) \left| \frac{\mathbf{e}_r.\mathbf{e}_\lambda}{i}\frac{\partial}{\partial r} \right| (A_{lm}(\mathbf{k})u_l(r)Y_{lm}(\hat{\mathbf{r}}) + B_{lm}(\mathbf{k})\dot{u}_l Y_{lm}(\hat{\mathbf{r}})) \right\rangle \right. \\ & \left. - \left\langle u_{l_c}(r)Y_{l_c m_c}(\hat{\mathbf{r}}) \left| \frac{1}{r}(\mathbf{e}_r \times \mathbf{L}).\mathbf{e}_\lambda \right| (A_{lm}(\mathbf{k})u_l(r)Y_{lm}(\hat{\mathbf{r}}) + B_{lm}(\mathbf{k})\dot{u}_l Y_{lm}(\hat{\mathbf{r}})) \right\rangle \right). \end{aligned} \tag{6.42}$$

Both of the terms inside the parenthesis can be separated into radial and angular part as

$$\left\langle u_{l_c}(r)Y_{l_cm_c}(\hat{\mathbf{r}})\left|\frac{\mathbf{e}_r.\mathbf{e}_\lambda}{i}\frac{\partial}{\partial r}\right|(A_{lm}(\mathbf{k})u_l(r)Y_{lm}(\hat{\mathbf{r}})+B_{lm}(\mathbf{k})\dot{u}_lY_{lm}(\hat{\mathbf{r}}))\right\rangle =$$
$$\left(A_{lm}(\mathbf{k})\left\langle u_{l_c}(r)\left|\frac{1}{i}\frac{\partial u_l(r)}{\partial r}\right.\right\rangle+B_{lm}(\mathbf{k})\left\langle u_{l_c}(r)\left|\frac{1}{i}\frac{\partial\dot{u}_l(r)}{\partial r}\right.\right\rangle\right)\langle Y_{l_cm_c}|\mathbf{e}_r.\mathbf{e}_\lambda|Y_{lm}\rangle\,, \quad (6.43)$$

and

$$\left\langle u_{l_c}(r)Y_{l_cm_c}(\hat{\mathbf{r}})\left|\frac{1}{r}(\mathbf{e}_r\times\mathbf{L}).\mathbf{e}_\lambda\right|(A_{lm}(\mathbf{k})u_l(r)Y_{lm}(\hat{\mathbf{r}})+B_{lm}(\mathbf{k})\dot{u}_lY_{lm}(\hat{\mathbf{r}}))\right\rangle =$$
$$\left(A_{lm}(\mathbf{k})\left\langle u_{l_c}(r)\left|\frac{1}{r}u_l(r)\right.\right\rangle+B_{lm}(\mathbf{k})\left\langle u_{l_c}(r)\left|\frac{1}{r}\dot{u}_l(r)\right.\right\rangle\right)\langle Y_{l_cm_c}|(\mathbf{e}_r\times\mathbf{L}).\mathbf{e}_\lambda|Y_{lm}\rangle\,. \quad (6.44)$$

It can be easily seen that the angular multiplicative factor of equation (6.43) involves the Gaunt coefficients $G_{l_c1l}^{m_c\lambda m}$. Using the spherical harmonic relations [125]:

$$cos(\theta)Y_{lm}=\sqrt{\frac{(l+m+1)(l-m+1)}{(2l+1)(2l+3)}}Y_{l+1m}+\sqrt{\frac{(l+m)(l-m)}{(2l+1)(2l-1)}}Y_{l-1m}, \quad (6.45)$$

and

$$[L_-,cos(\theta)]=\hbar e^{-i\phi}sin(\theta), \quad (6.46)$$

the angular multiplicative factor of equation (6.44) can be expressed as a function of spherical harmonics. Using the mentioned relations, after some algebraic manipulations the matrix transitions for different polarizations can be formulated as

$$\begin{aligned}M_{j\mu}^{\mathbf{q}+}(\mathbf{k})=\textstyle\sum_{m,m_s}C_{l_cm_c,\frac{1}{2}m_s}^{j\mu}\Big(&-\left(A_{lm}(\mathbf{k})\left\langle u_{l_c}(r)\left|\tfrac{1}{i}\tfrac{\partial u_l(r)}{\partial r}\right.\right\rangle+B_{lm}(\mathbf{k})\left\langle u_{l_c}(r)\left|\tfrac{1}{i}\tfrac{\partial\dot{u}_l(r)}{\partial r}\right.\right\rangle\right)\sqrt{\tfrac{4\pi}{3}}G_{l_c1l}^{m_c+1m}\\&+\left(A_{lm}(\mathbf{k})\left\langle u_{l_c}(r)\left|\tfrac{1}{r}u_l(r)\right.\right\rangle+B_{lm}(\mathbf{k})\left\langle u_{l_c}(r)\left|\tfrac{1}{r}\dot{u}_l(r)\right.\right\rangle\right)\tfrac{1}{\sqrt{2}}\delta_{mc,m+1}\\&.\left((l+1)\sqrt{\tfrac{(l-m)(l-m-1)}{(2l-1)(2l+1)}}\,\delta_{l_c,l-1}+l\sqrt{\tfrac{(l+m+2)(l+m+1)}{(2l+1)(2l+3)}}\delta_{l_c,l+1}\right)\Big)\,.\end{aligned} \quad (6.47)$$

$$\begin{aligned}M_{j\mu}^{\mathbf{q}-}(\mathbf{k})=\textstyle\sum_{m,m_s}C_{l_cm_c,\frac{1}{2}m_s}^{j\mu}\Big(&\left(A_{lm}(\mathbf{k})\left\langle u_{l_c}(r)\left|\tfrac{1}{i}\tfrac{\partial u_l(r)}{\partial r}\right.\right\rangle+B_{lm}(\mathbf{k})\left\langle u_{l_c}(r)\left|\tfrac{1}{i}\tfrac{\partial\dot{u}_l(r)}{\partial r}\right.\right\rangle\right)\sqrt{\tfrac{4\pi}{3}}G_{l_c1l}^{m_c-1m}\\&-\left(A_{lm}(\mathbf{k})\left\langle u_{l_c}(r)\left|\tfrac{1}{r}u_l(r)\right.\right\rangle+B_{lm}(\mathbf{k})\left\langle u_{l_c}(r)\left|\tfrac{1}{r}\dot{u}_l(r)\right.\right\rangle\right)\tfrac{1}{\sqrt{2}}\delta_{mc,m-1}\\&.\left((l+1)\sqrt{\tfrac{(l+m)(l+m-1)}{(2l-1)(2l+1)}}\,\delta_{l_c,l-1}+l\sqrt{\tfrac{(l-m+2)(l-m+1)}{(2l+1)(2l+3)}}\delta_{l_c,l+1}\right)\Big)\,.\end{aligned} \quad (6.48)$$

$$\begin{aligned}M_{j\mu}^{\mathbf{q}z}(\mathbf{k})=\textstyle\sum_{m,m_s}C_{l_cm_c,\frac{1}{2}m_s}^{j\mu}\Big(&\left(A_{lm}(\mathbf{k})\left\langle u_{l_c}(r)\left|\tfrac{1}{i}\tfrac{\partial u_l(r)}{\partial r}\right.\right\rangle+B_{lm}(\mathbf{k})\left\langle u_{l_c}(r)\left|\tfrac{1}{i}\tfrac{\partial\dot{u}_l(r)}{\partial r}\right.\right\rangle\right)\sqrt{\tfrac{4\pi}{3}}G_{l_c1l}^{m_c0m}\\&+\left(A_{lm}(\mathbf{k})\left\langle u_{l_c}(r)\left|\tfrac{1}{r}u_l(r)\right.\right\rangle+B_{lm}(\mathbf{k})\left\langle u_{l_c}(r)\left|\tfrac{1}{r}\dot{u}_l(r)\right.\right\rangle\right)\delta_{mc,m}\\&.\left((l+1)\sqrt{\tfrac{(l-m)(l+m)}{(2l-1)(2l+1)}}\,\delta_{l_c,l-1}-l\sqrt{\tfrac{(l-m+1)(l+m+1)}{(2l+1)(2l+3)}}\delta_{l_c,l+1}\right)\Big)\,.\end{aligned} \quad (6.49)$$

The brackets in (6.46) denote the commutator, and θ and ϕ are the spherical angles. Inserting equations (6.47),(6.48) and (6.49) in equation (6.29) and performing $\mathbf{k}$-integration (according to the Brillouin zone integration methods explained in section (4.4.4)) one can finally calculate the corresponding absorption coefficients $\mu^{\mathbf{q}+}(\omega)$, $\mu^{\mathbf{q}-}(\omega)$, and $\mu^{\mathbf{q}0}(\omega)$ for left, right, and z polarized light, and therefore calculate the *key* physical quantity:

$$\Delta\mu(\omega)=\mu^{\mathbf{q}+}(\omega)-\mu^{\mathbf{q}-}(\omega)\neq 0. \quad (6.50)$$

If x-rays are absorbed by a magnetic solid the absorption coefficients for left and right circularly polarized photons are in general different so that $\Delta\mu \neq 0$. This quantity can be measured experimentally [100] and is called x-ray magnetic circular dichroism (XMCD). As it can easily be seen from equations (6.47), (6.48), and (6.49) the corresponding matrix transitions elements $M_{j\mu}^{\mathbf{q}\lambda}(\mathbf{k})$ do not vanish only if

$$\left\{ \begin{array}{ccccc} \Delta l & = & l - l_c & = & \pm 1 \\ \Delta m & = & m - m_c & = & \lambda \\ \Delta m_s & = & m_s - m_{sc} & = & 0 \end{array} \right. \tag{6.51}$$

These conditions are used to select the allowed transitions within the dipolar approximation and they are known as the dipole selection rules.

6.3 The XMCD sum rules

Magnetic compounds and alloys characterization represent one of the outstanding problem in condensed matter physics. Recently, a considerable evolution of the spectroscopic techniques has been achieved and was helped by theoretical efforts. With the derivation of the sum rules by Thole and coworkers [26, 27] XMCD spectroscopy became the most used technique for studying magnetic materials. These sum rules supply a firm basis to estimate directly from XMCD spectra the orbital moment ($m_L = -\frac{\mu_B}{\hbar}\langle L_z\rangle$) and the magnetic moment ($m_S = -2\frac{\mu_B}{\hbar}\langle S_z\rangle$) contributions to the total magnetic moment associated with a specific state of given symmetry. Thus the magnetic spin and orbital moments of the absorber atom are related to the integrated absorption spectra for a specific core shell and polarization of the radiation as

$$\int_{j_+} \Delta\mu dE - \left[\frac{l_c+1}{l_c}\right] \int_{j_-} \Delta\mu dE = \frac{N}{n_h}\left[\frac{l(l+1)-2-l_c(l_c+1)}{3l_c}\langle S_z\rangle + \frac{l(l+1)\left[l(l+1)+2l_c(l_c+1)+4\right]-3(l_c-1)^2(l_c+2)^2}{6ll_c(l+1)}\langle T_z\rangle\right], \tag{6.52}$$

and

$$\int_{j_++j_-} \Delta\mu dE = \frac{N}{2n_h}\left[\frac{l(l+1)+2-l_c(l_c+1)}{l(l+1)}\right]\langle L_z\rangle, \tag{6.53}$$

where N is the total integrated spectrum corresponding to the unpolarized radiation (known also as the isotropic absorption contribution)

$$N = \int_{j_++j_-} \left(\sum_{\lambda=+,-,0} \mu^\lambda\right) dE, \tag{6.54}$$

$$\Delta\mu = \mu^+ - \mu^-,$$

and T_z is the magnetic dipole operator

$$T_z = \frac{1}{2}\left[\boldsymbol{\sigma} - 3\hat{\mathbf{r}}(\hat{\mathbf{r}}.\boldsymbol{\sigma})\right]_z. \tag{6.55}$$

$\int_{j_++j_-}$ means that the integral is performed over both of the $j_+ = l+1/2$ and $j_- = l-1/2$ edge spectra, e.g., $j_+ = 3/2$ and $j_- = 1/2$ for the $L_{2,3}$ edges of transition metals, n_h denotes the number of holes or the number of unoccupied final states, and $\langle S_z\rangle$, $\langle L_z\rangle$, and

$\langle T_z \rangle$ are respectively, the expectation values of the magnetic moment, the orbital moment, and the magnetic dipole operator.
The expectation value of the magnetic dipole operator accounts for the asphericity of the spin magnetization. This asphericity can be considered as a magnetic anisotropy resulting from the spin-orbit coupling or crystal-field effects. Appendix (C) is devoted to the implementation of T_z within the FLAPW method.
The application of these sum rules provide as with the magnetic spin and orbital moments since the expectation value of the T_z operator is determined. In order to extract these moments from the absorption spectra we have implemented (see paper I) the sum rules for the different edges:
K

$$\int_{E_F}^{E_{cut}} \Delta\mu dE = \frac{N}{n_h} \langle L_z \rangle , \tag{6.56}$$

where

$$N = \sum_{\lambda=+,-,0} \int_{E_F}^{E_{cut}} \Delta\mu^{\lambda}, \tag{6.57}$$

$L_{2,3}$

$$\int_{E_F}^{E_{cut}} \left[(\mu^{+}_{L_3} - \mu^{-}_{L_3}) - 2(\mu^{+}_{L_2} - \mu^{-}_{L_2}) \right] dE = \frac{N}{3n_h} \left[\langle S_z \rangle + 7 \langle T_z \rangle \right] , \tag{6.58}$$

$$\int_{E_F}^{E_{cut}} \left[(\mu^{+}_{L_3} - \mu^{-}_{L_3}) + (\mu^{+}_{L_2} - \mu^{-}_{L_2}) \right] dE = \frac{N}{2n_h} \langle L_z \rangle , \tag{6.59}$$

where

$$N = \sum_{\lambda=+,-,0} \int_{E_F}^{E_{cut}} (\Delta\mu^{\lambda}_{L_3} + \Delta\mu^{\lambda}_{L_2}), \tag{6.60}$$

and $M_{4,5}$

$$\int_{E_F}^{E_{cut}} \left[(\mu^{+}_{M_5} - \mu^{-}_{M_5}) - \frac{3}{2}(\mu^{+}_{M_4} - \mu^{-}_{M_4}) \right] dE = \frac{N}{3n_h} \left[\langle S_z \rangle + 6 \langle T_z \rangle \right] , \tag{6.61}$$

$$\int_{E_F}^{E_{cut}} \left[(\mu^{+}_{M_5} - \mu^{-}_{M_5}) + (\mu^{+}_{M_4} - \mu^{-}_{M_4}) \right] dE = \frac{N}{3n_h} \langle L_z \rangle , \tag{6.62}$$

where

$$N = \sum_{\lambda=+,-,0} \int_{E_F}^{E_{cut}} (\Delta\mu^{\lambda}_{M_5} + \Delta\mu^{\lambda}_{M_4}). \tag{6.63}$$

The integrations are carried out from the Fermi-energy E_F up to an energy cutoff E_{cut}. This energy represents the energy of the top of the final magnetic states. The number of holes n_h are also calculated from the density of states, and they are determined from the integration of the unoccupied part of the involved density of final states.
In order to make a useful and relevant applications of these sum rules one should know their limitations by knowing the assumptions made during the derivation. To derive the XMCD sum rules, the authors have adopted the single ion model combined with a scalar relativistic approach. The principle assumption of these sum-rules derivation is that of the two-step model [100]. Depending on the photon polarization, the XMCD transitions will be achieved in two steps. Firstly, the core electron will choose one of the spin directions

according to the core spin-orbit splitting, that is to say, depending on the encountered spin-orbit interaction and because of the conservation of the angular momentum during the absorption process the angular momentum carried out by the photon is completely or partially transferred to the photo-electron , in a second step the exchange spin-splitting of the final state is different whether the spin of the incoming electron is up or down. this could simulate the eventual change of the exchange splitting resulting from the spin dependence of the incoming photo-electron. The others assumptions of the underlying physics of the XMCD sum rules are to ignore the following [126]:

1. the exchange splitting of the core states,
2. the asphericity of the core states,
3. the difference between the radial relativistic part of the final wave functions, i.e., the radial parts $u_l(r)$ of $p_{1/2}$ and $p_{3/2}$ or $d_{3/2}$ and $d_{5/2}$ are the same, and
4. the energy dependence of the wave function.

Despite such limiting approximations, the validity of the sum rules appears to be now rather well established, at least in the cases of the $L_{2,3}$ absorption edges of $3d$ [127, 128, 129], $4d$ [130] and $5d$ [131] transition metals. However, one should keep in mind that there are some problems when applying the sum rules to XMCD spectra. The most severe one is the separation of the L_2- and L_3-spectra, e.g., because of the strong hybridization between the $2p$ N orbitals and the $4d$ Gd orbitals in GdN compound ([132] and references therein). The $5d$-Gd magnetic moment extracted from the application of the sum rules to $L_{2,3}$ edges of Gd could not account for the realistic $5d$ magnetic moment since a part of that moment is supposed transferred or transformed to $2p$ magnetic moment.
Apart from this weak point of the XMCD sum-rules, the successful use we have made of the XMCD sum-rules to calculate the magnetic moment of Gd atoms in gadolinium bulk have shown the validity and the usefulness of these sum rules for strongly localized $4f$ materials (see paper I). This is not surprising since $4f$ rare-earth orbitals are so localized that the hybridization with others orbital will be marginal and f states will carry the whole magnetic moment of $4f$ electrons. Therefore we expect that $4f$ magnetic materials such as rare-earth metals are well studied by XMCD investigations.

Chapter 7

Results

Each article will be referred to by its Roman numeral. In the preamble of this chapter we would like to draw some comments on the results presented in these papers. All the calculations presented in these papers are made by means of the FLAPW method [25], which makes no shape approximation to either the potential or the charge density, and is acknowledged to be the state-of-the-art in electronic calculations accuracy. In paper I, a detailed study of the electronic structure of gadolinium bulk is provided. In the first section, the controversial long debate concerning the manner in which the Gd f orbitals should be treated is presented. This is supported by a quite rich bibliographical work. Then the Gd electronic structure is reviewed within the LDA(GGA)+U method. The results obtained within this method concerning the the photoemission, inverse photoemission, the ground-state magnetic structures, as well as the x-ray absorption (XAS) and x-ray magnetic circular dichroism (XMCD) of strongly localized $4f$ electrons are found to be in good agreement with experiment.
Paper II is aimed at studying the GdN compound electronic structure. Within this paper emphasis is put on structural properties. In this respect, it was shown that the GdN ground state is that of a typical half-metal for the experimental lattice constant. Under hydrostatic pressure the rocksalt GdN lattice prefers the wurtzite crystal lattice.
In paper III, we present the results concerning the magnetocrystalline anisotropy energy (MAE) study of Gd and some of it's compounds (GdN and $GdFe_2$). Once more, the GGA+U is found to be the most adequate to explain the observed magnetic anisotropy. That is to say the GGA+U is not only the most appropriate method for electronic and structural properties of strongly localized $4f$ electrons systems but also their magnetic properties. The force-theorem calculated MAE showed that for Gd the easy axis of magnetization lies along the c axis of the hcp structure, and for GdN and $GdFe_2$, the three symmetry equivalent axes (100), (010), and (001) are those of the easy axes of magnetization. The energy position of the $4f$ states is shown to be the responsible of the strength of the MAE of Gd and Gd compounds.

Paper I

[*Signalement bibliographique ajouté par* :
SICD Strasbourg - Département de la Documentation électronique
Service des thèses électroniques]

Electronic structure and x-ray magnetic circular dichroism of gadolinium beyond the local spin density approximation

Samir ABDELOUAHED, N. BAADJI, and M. ALOUANI

Physical Review B, 2007, Vol. 75, Pages 094428(1-11)

Pages 71-82 :
La publication présentée ici dans la thèse est soumise à des droits détenus par un éditeur commercial.

Les utilisateurs de l'ULP peuvent consulter cette publication sur le site de l'éditeur :
http://dx.doi.org/10.1103/PhysRevB.75.094428

La version imprimée de cette thèse peut être consultée à la bibliothèque ou dans un autre établissement via une demande de prêt entre bibliothèques (PEB) auprès de nos services :
http://www-sicd.u-strasbg.fr/services/peb/

Paper II

[*Signalement bibliographique ajouté par* :
SICD Strasbourg - Département de la Documentation électronique
Service des thèses électroniques]

Calculated electronic properties and structural phase transitions of GdN pnictide under hydrostatic pressure

Samir ABDELOUAHED and M. ALOUANI

Physical Review B, 2007, Vol. 76, Pages 214409(1-7)

Pages 85-92 :
La publication présentée ici dans la thèse est soumise à des droits détenus par un éditeur commercial.

Les utilisateurs de l'ULP peuvent consulter cette publication sur le site de l'éditeur :
http://dx.doi.org/10.1103/PhysRevB.76.214409

La version imprimée de cette thèse peut être consultée à la bibliothèque ou dans un autre établissement via une demande de prêt entre bibliothèques (PEB) auprès de nos services :
http://www-sicd.u-strasbg.fr/services/peb/

Paper III

Calculated magnetic anisotropy of Gd, GdN and $GdFe_2$

Samir Abdelouahed and M. Alouani[1]

[1]*Institut de Physique et de Chimie des Matériaux de Strasbourg (IPCMS), UMR 7504 CNRS-ULP, 23 rue du Loess, BP 43, 67034 Strasbourg Cedex 2, France.*

Abstract

The tiny magnetocrystalline anisotropy energies (MAEs) of bulk Gd, GdN and $GaFe_2$ have been calculated by means of the the force theorem in conjunction with the full-potential linear augmented plane-waves (FLAPW) method. The generalized gradient correction including the Hubbard interaction U (GGA+U) produced the best possible agreement with the experimental MAE compared to the GGA or the GGA where the $4f$ states are treated as core electrons (GGA-core). However, it showed that the magnetization is along c axis in disagreement with experiment and a recent calculation which showed that the easy axis of magnetization makes an angle of about 20° with the c axis. The GGA+U results are found in good agreement with Bruno's model. Therefore, the disagreement with experiment is attributed to possible presence of imperfection in the hcp structure of Gd, like defect states or dislocations. Because the $4f$ states of Gd are half-filled, their orbital moment and spin-orbit coupling are zero, making the Gd MAE tuned by the spin-orbit coupling of $5d$ states rather than the $4f$ like in the case of other rare earth elements, such as Tb or Dy. The strength of MAE is found to be related to the energy position of the $4f$ states. This suggests that the MAE of Gd is much similar to that of a transition metal rather than that of a typical rare-earth metal such as Tb or Dy. It is not surprising therefore that Gd shows an easy axis along the (0001) direction like hcp cobalt. However, the MAEs of GdN and $GdFe_2$ compounds crystallizing, respectively, in cubic rocksalt and Laves phase structures, are more complex than that of Gd. It is found that the magnetization is along one of the symmetry equivalent (100), (010), or (001) direction, rather than the (111) direction of fcc nickel, and their respective MAEs are much smaller than that of Gd.

PACS numbers:

I. INTRODUCTION

The magnetocrystalline anisotropy energy (MAE) is the energy required to rotate the magnetization from its ground state direction called the easy direction to the hardest direction. This rotation influences the magnetic properties of a films, low-dimensional magnetic nanostructures or atomic chains. Its application field is growing fast, e.g., permanent magnetic materials anisotropy [1–4], perpendicular magnetic anisotropy of ultra-thin films and surfaces [5–8] or the parallel interfacial magnetic anisotropy of a ferromagnetic (FM) and antiferromagnetic (AFN) bilayer [9–11] known to be at the origin of the exchange-bias phenomena, are promising for high-density magneto-optical storage media or for spin valve devices, low-dimensional nanostructures [12]. Atomic chains or nanowires [13] magnetic anisotropy is a challenging candidate for new high-density magnetic storage materials because of the peculiar physical properties of the nano-scale materials. The growing interest of the scientific community working on magnetic anisotropy is therefore not surprising.

The intrinsic coupling between the magnetization and the crystal lattice in ferromagnets is insured by the strength of the spin-orbit coupling (SOC). For example, for the $3d$ ferromagnets the crystal lattice variation under pressure, doping, alloying or compositional disorder gives rise to a significant change of the magnetic properties, like the evolution of the MAE with respect to the pressure in bulk or thin films cobalt (Co) [7, 14], which is known as the magnetostrictive effect, and was investigated by means of element-specific x-ray magnetic circular dichroism (XMCD) spectroscopy. In particular, the cubic magnetic anisotropy of (Ga,Mn)As ferromagnetic semiconductor is observed to survive under doping [15], while it changes due to the substrate- or layer-induced strain [8, 16]. It has also been found that the compositional modulations of $Co_{0.5}Pt_{0.5}$ alloy have a significantly enhanced MAE compared to that of the intrinsic $L1_0$ structure (3 times larger than that of the $L1_0$ structure) based on calculations within the spin-polarized relativistic Korringa-Kohn-Rostoker coherent-potential approximation (SPR-KKR-CPA) [1]. The same approach applied, some years later, to bcc-iron (Fe) based materials showed that the MAE of bcc-Fe bulk or bcc-$Fe_{1-c}V_c$ disordered bulk alloys is altered by volume or concentration variation [2].

In the previously mentioned investigations for $3d$ based magnetic materials, the MAE ranges from a few tenths of μeV for bulk material, e.g., Co bulk [14], to some meV for

surfaces or alloys, eg., $Co_{0.5}Pt_{0.5}$ thin film [17] or Fe on W(110) [8]. According to Bruno's [5] and van der Laan's [18] models, this tiny MAE stems mainly from orbital moment anisotropy due to the small spin-orbit interaction in $3d$ magnetic materials. However, despite the so small SOC strength, the corresponding MAE is the result of a complex interplay of the crystal and the magnetic degrees of freedom. In this respect, the magnetostriction phenomena is still far from being fully understood. To put it in other words, the understanding of the complexity of magnetic anisotropy phenomenon is a challenging task not only from the point of view of practical interests but also from that of fundamental physics.

Despite the applications of MAE for many industrial needs, it is surprising to notice that while it is intensively investigated for $3d$ based magnetic materials, only a little attention is paid to that of rare earth materials, such as the gadolinium metal [19–21]. In this respect, our paper is mainly devoted to the investigation of the magnetic anisotropy of hcp Gd metal which is known to be the strongest magnetic material of the rare-earth elements, whereas those of terbium and dysprosium are only invoked for comparison. To get insight into the MAE of Gd-compounds, the behavior of the Gd MAE in the presence of other elements GdN and $GdFe_2$ MAE are also calculated and discussed.

To the best of our knowledge, apart from the early MAE Gd investigations of Franse *et al.* [20] and that of the recent calculations of Colarieti-Tosti *et al.* [21], the magnetic anisotropy of $4f$ rare earth metals is lacking. Therefore studying the MAE of such materials or their compounds is enriching. Our MAE calculations for Gd are motivated by its interesting magnetic properties. Indeed, despite its room temperature Curie temperature, this metal is found to preserve a considerable spin magnetic moment up to an ultrahigh hydrostatic pressure of about ~ 110 GPa [22, 23]. This magnetic moment, of about $7\mu_B$, is much higher than that of $3d$ transition metal because it stems mostly from the half-filled $4f$ shell.

In the present work, we made use of the force theorem [24] to study the magnetic anisotropy of Gd (Tb and Dy), GdN, and $GdFe_2$ within the first-principles FLAPW method. We have firstly shown that, like for the electronic and structural properties of Gd [25] and GdN [26] that the GGA+U is also superior to the GGA method in calculating the MAE. This shows indirectly that the MAE strength is related to the position of the $4f$ states with respect to the Fermi level.

This paper is organized as follows. In Sec. II we provide some details of the computational method and discuss the parameters used in the calculations, such as the values of Hubbard

U and exchange J used for calculations of the MAE. Sec. III is devoted to the MAE of Gd, i.e., we show the adequacy and the accuracy of the GGA+U method for force theorem calculations, as well as the Bruno's model calculation applied for the first time to study the MAE of a rare earth Gd. In Sec. IV the magnetic anisotropies of the GdN and GdFe2 compounds are studied, and the manner in which the $4f$ magnetization might affect the MAE of Gd compounds is discussed.

II. COMPUTATIONAL DETAILS

The calculations in the present work were made using the FLAPW method [27, 28] as implemented in the FLEUR code [29]. The lattice parameter constants used for the calculations are a=6.858 a.u. with a c/a ratio of 1.597 for hcp bulk Gd [30], a=6.858 a.u. for cubic rocksalt GdN [31], and a=13.96 a.u. for the cubic Laves structure of $GdFe_2$ [32]. In order to calculate the MAE using the force theorem, the SOC is calculated in a second-variational scheme [25]. For the exchange and correlation potential, we used the generalized-gradient approximation (GGA) of Perdew-Burke-Ernzerhof [33]. The rotationally invariant GGA+U method used in this study is similar to the implementation of Shick *et al.* [34]. For the U and J parameters of the Gd sites required for GGA+U calculations we have used: U = 7.7 eV, J = 0.7 eV [25], and U = 9.9 eV, J = 1.2 eV [26] for Gd bulk and GdN, respectively. For $GdFe_2$ we have used those of bulk Gd [35]. The muffin-tin radii $\mathbf{R}_{mt}$ is set to 2.8 a.u. for Gd, 2.19 a.u. for Fe, and 1.5 a.u. for N. The plane wave cutoff for the basis functions is set to K_{max} = 3.0 a.u.$^{-1}$ for Gd bulk, K_{max} = 4.4 a.u.$^{-1}$ for GdN, and K_{max} = 3.5 a.u.$^{-1}$ for $GdFe_2$, the charge density and potential cutoff to G_{max} = 9.0 a.u.$^{-1}$ for bulk Gd and GdN, to G_{max} = 11.4 a.u.$^{-1}$ for $GdFe_2$. The wave functions as well as the charge density and the potential inside the muffin-tin spheres were expanded on angular momentum up to l_{max} = 8 for Gd bulk and GdN, and up to l_{max} = 10 for $GdFe_2$. For the Brillouin zone (BZ) integration, we have used the standard Gaussian broadening method [36] for the force theorem calculated MAE. The convergence of the MAE is obtained using about 16, 7 and 10 thousand $\mathbf{k}$ points in the full BZ, for the case of Gd, GdN, and $GdFe_2$, respectively.

III. FORCE THEOREM DETERMINATION OF THE MAE FOR GD METAL

The calculations carried out within the GGA+U method [25, 26]) have provided a good description of the the electronic properties of the $4f$ Gd and GdN materials. These results have motivated our present force theorem calculations of the MAE. At a first stage, we show that the GGA+U approach is much better than the GGA and GGA-core for the description of MAE. The force theorem GGA+U calculations explain the observed MAE. Then we use the same method to predict the rotation that the magnetization might undergo in the case of GdN and $GdFe_2$ compounds.

A. GGA+U adequacy for magnetic anisotropy calculations

In the last two decades, the force theorem [24] has been an important and efficient tool for computing the MAE [37–39]. As originally proposed by Van Vleck [40], the magnetocrystalline anisotropy originates mainly from the SOC. Its variation might lead to interesting tuning of the orbital magnetic moments and MAE of complex materials and may lead to the violation of Hund's third rule [41]. Indeed, the force theorem based calculations save an appreciable computational effort and computer CPU time. This is because the simulation of the magnetization direction changes via the SOC requires only one single iteration of the Kohn-Sham equations. The basic idea of the force theorem is to introduce the spin-orbit interaction as a perturbation to the scalar relativistic Hamiltonian. It is shown that the rotation of the spins is such a tiny perturbation that the electron-electron interaction hardly changes. We expect therefore that most of the contributions to the total energy remain unchanged, and subsequently the total energy difference between two spin configurations with the magnetization along two different polarization directions is given approximately by the difference between the sums of the eigenvalues up to the Fermi energy. Because this change of the total energy using a frozen potential approximation is given by the sum of one-electron energy difference [24], one can calculate this difference, with less computational effort, by *switching on* the SOC to diagonalize the relativistic Hamiltonian. This is the way in which we proceeded during our evaluations of the MAE, i.e., we first make a self-consistent calculation with a scalar relativistic potential without spin-orbit interaction, then we calculated the eigenvalues including the spin-orbit interaction for a given spin axis

without allowing the self-consistent potential to change. Notice that one has to make sure that the scalar relativistic calculations are converged with the same number of **k** points as these used to determine the MAE (see Fig 1 b).

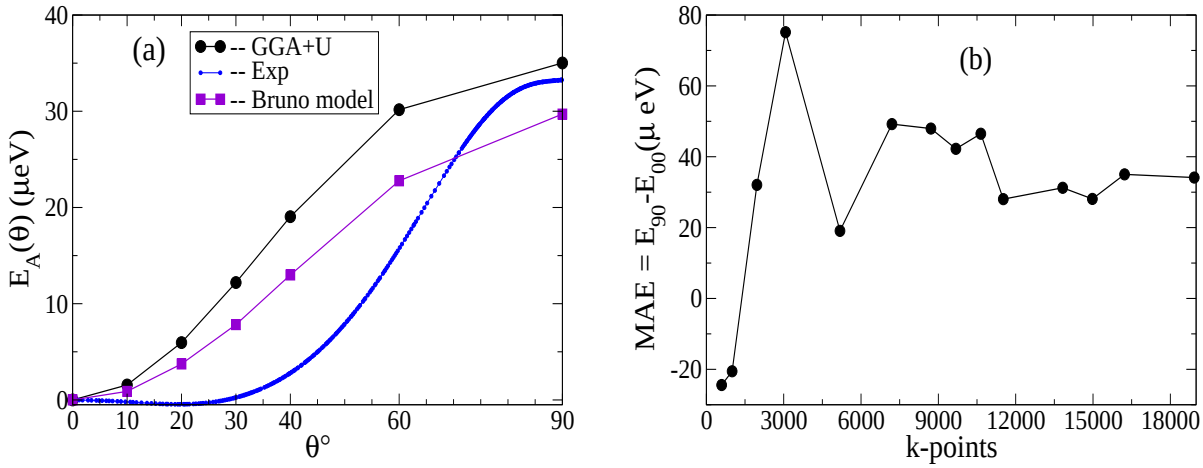

FIG. 1: (a) The GGA+U calculated MAE of Gd as a function of the angle θ from the c axis (black circles) and the Bruno model MAE (equation 1) (violet squares) compared to the experimental one (blue curve) [20]. (b) Difference in the sums of eigenvalues where the magnetization is along the hard ($\theta = 90°$) and easy ($\theta = 0°$) axis, respectively, as a function of the number of **k** points in the whole Brillouin zone. The continuous curves are guides for the eye.

B. The Gd (0001) magnetization easy axis

In this section, we discuss the Gd MAE within the GGA+U method. Figure 1(a) shows the MAE calculations for different angles θ, i.e., the difference of the eigenvalue sums as a function of the angle θ between the c axis and the magnetization axis. The reference energy is at $\theta = 0°$. The GGA+U MAE calculations are in black circles and those calculated according to the Bruno's model are in violet squares (equation (1)). As it can be easily seen from this figure, the minimum of the difference of the eigenvalue sums is obtained for 0° and the maximum for 90°. These results show clearly that the easy axis of magnetization is lying at $\theta = 0°$ and the hard one at $\theta = 90°$. These calculations were carried out using a sampling

of around 16000 **k**-points in the whole Brillouin zone. In order to justify the convergence of this Gaussian broadening sampling [36], we have performed MAE calculations up to 18000 **k** points in the BZ. Figure 1(b) represents the MAE convergence according to the set of **k** points. This MAE is defined as the difference energy between the hard and easy axis of magnetization. The overall shape of the MAE presented in figure 1(b) shows that this latter is sensitive to the **k**-points number up to the set of 16224 **k** points. The largest number considered is 18928 **k** points and it yields a MAE that deviates by less than 2% from the MAE using 16224 **k** points. We have checked the force theorem MAE by directly calculating the total energy including the spin-orbit coupling in a self-consistent manner. The results of the calculations showed that the MAE is about 32.14 μeV using 16224 **k** points, in good agreement with the converged force theorem calculation (see Fig. 1(b)). We note here that though the force theorem allows a saving of considerable computational effort, it still requires a considerable computational time because of the fine grid of **k** points one should use to assess the tiny MAE.

Figure 2 summarizes the MAE calculations for the different ways in which the 4f electrons are treated. In order to compare the GGA+U (figure 1(a)) MAE to the other methods this latter is represented with the GGA, and the GGA-core. It is worth mentioning here the controversial debate concerning whether the Gd $4f$ states should be considered as localized core states or whether it should be allowed to hybridize as band states (Ref. [25] and references therein). As it can be easily seen from figure 2, the Gd MAE calculated within the GGA+U scheme is in much better agreement with experiment (figure 1(a)). The value of 520 μeV of our MAE, calculated using the standard GGA potential, is in good agreement with the FP-LMTO calculation of 571 μeV by Colarieti-Tosti *et al.* [21]. However, within our FLAPW framework, the core treatment of the $4f$ electrons leads to a MAE of 87 μeV, while within the FP-LMTO one [21] it is of about only 24 μeV in disagreement with our calculation. In order to understand the SOC magnetic-anisotropy in more details, we have applied Bruno's model [5] to calculate the Gd MAE. According to this model the MAE stems completely from the spin-orbit contribution and the anisotropy of orbital magnetic moments and is given by:

$$E_A(\theta) = \Delta E(\theta, 0^\circ) = -\frac{\xi}{4\mu_B}\left([\mu^{\uparrow}_{orb}(\theta) - \mu^{\downarrow}_{orb}(\theta)] - [\mu^{\uparrow}_{orb}(0^\circ) - \mu^{\downarrow}_{orb}(0^\circ)]\right), \qquad (1)$$

where ξ is the spin-orbit parameter for $5d$ Gd orbitals and μ^{σ}_{orb} the orbital moment of the

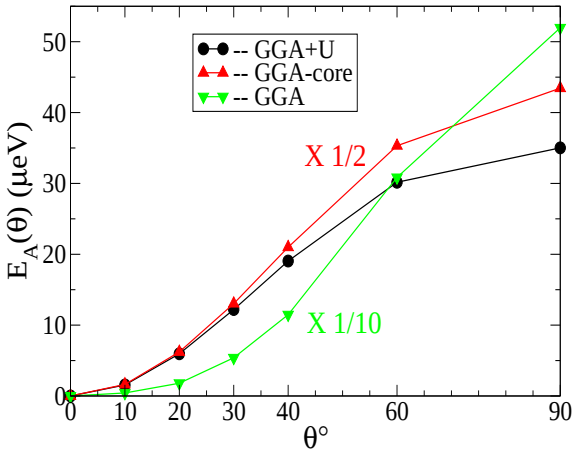

FIG. 2: (Color on line) Calculated Gd MAE for the different treatments of the $4f$ states. The calculation within the GGA+U method is shown in black circles and is the same as that of figure 1. The GGA-core, where the $4f$ states are considered as core electrons, is shown in red up triangles, while the standard GGA, where the $4f$ electrons are allowed to relax as valence bands is shown in green down triangles. Notice that the GGA and GGA-core curves are scaled, respectively, by a factor of 1/10 and 1/2 to fit into the graph. The continuous curves are guides for the eye.

spin σ. We have presented in figure 1(a) (violet curve) the corresponding calculations. The spin-orbit coupling parameter we have used to calculate the MAE according to the Bruno model is that of the $5d$ orbitals and is found to be of $\xi = \xi_d = 71.15$ meV. As it can be seen from this figure the overall behavior of the estimated MAE of the model is too similar to that of the GGA+U. The MAE calculated according to Bruno's model is somewhat situated between our GGA+U calculations and the experimental one. Bruno's model predicts a MAE maximum of 30 μ eV. Given the fact that the spin-orbit parameter ξ and the orbital moment μ^{σ}_{orb} used in equation (1) are those of the GGA+U calculations, the agreement of the full calculation with the model is not surprising. However, this implies that the MAE is essentially due to the orbital moment anisotropy. Gd is such a complex metal, and we have seen that the energy position of the $4f$ states is crucial for the strength of the MAE. We can only conclude here, that once the $4f$ levels are well positioned, the MAE is mainly due to the orbital moment anisotropy as suggested by Bruno's model.

Bruno's model validity for describing the spin-orbit magnetic anisotropy of Gd should reflect the fact that the magnetic anisotropy of Gd is too similar to that of a typical $3d$ transition metal such as hcp Co. However, there are additional terms which are related to the magnetic dipole operator due to the anisotropy of the field of the spin. This additional contribution was derived by van dar Laan [18]. The strong magnetic moment of the $4f$ electrons might give rise to this latter contribution. The resulting exchange field of that $4f$ spin is large enough to be sufficient to polarize significantly the remaining conduction electrons. In others words, the $4f$ magnetic field makes, in particular, the Gd $5d$ magnetic moment parallel to that of the $4f$. Despite this high magnetic field, the van dar Laan contribution for Gd is found to be negligible compared to that expected from Bruno's model. In fact, this contribution is only considerable for non half-filled systems where spin flips among the $4f$ electrons occur.

However, though the GGA+U calculations using the force theorem have reproduced the experimental magnitude of MAE of 34 μeV, they did not show that the easy axis of the magnetization makes 20° away from the c axis as experimentally observed, instead they show that it is along the c direction. If we believe our calculation, which is in agreement with Bruno's model and in disagreement with the FP-LMTO calculation using $4f$ states as core states [21], then the deviation of the magnetization from the c axis could be only explained if one invokes symmetry breaking lattice imperfections of the hcp structure of Gd, like presence of intrinsic defects, impurities, or dislocations. We suspect the erroneous GGA energy positions of the 4f minority states [25] to be at the origin of the corresponding predicted large MAE. The presence of these states near the Fermi level leads to the erroneous MAE. The integration of the one-electron energies includes an *extra*-contribution coming from a strong mixing of the $4f$ states with the others states at the Fermi level. Using the GGA+U method these $4f$ states are moved away from the Fermi level (U effect) resulting in a more realistic assessment of the MAE. The MAE is therefore sensitive to the electronic structure around the Fermi level and a better representation of the electronic structure could lead to a precise evaluation of the MAE. Compared to the GGA and GGA-core, the GGA+U method is once more the best one for the MAE calculations. Given the adequacy of the GGA+U, we have proceeded in the same way to calculate the MAEs of GdN and $GdFe_2$.

IV. GdN AND $GdFe_2$ MAGNETIC ANISOTROPY

In order to get insight into the magnetic anisotropy of Gd compound, we have applied the force theorem to calculate the MAE of the GdN pnictide and the metallic compound $GdFe_2$. Using the GGA+U method, we have recently shown that the GdN compound is a half-metal for the experimental lattice constant [26]. A better understanding of the magnetic anisotropy of this compound would be useful for future spin-injection applications.

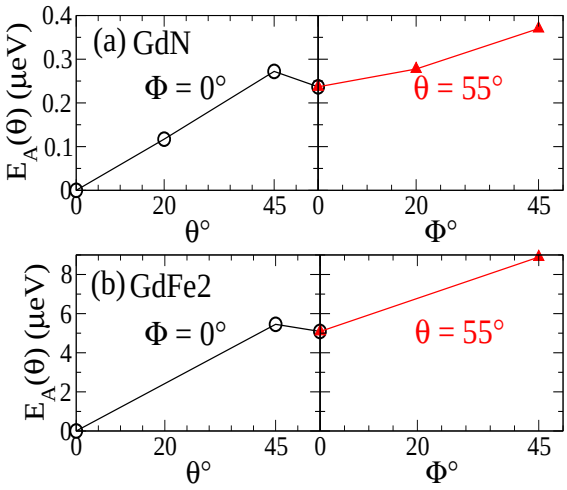

FIG. 3: GGA+U calculations of the GdN and $GdFe_2$ MAE; (a) Calculated MAE of GdN as a function of the angles θ, ϕ for: varying ϕ while keeping $\theta = 55°$ in red triangles and varying θ while keeping $\phi = 0°$ in black circles, (b) The $GdFe_2$ MAE for the same magnetization directions. The continuous curves are guides for the eye.

In this section the MAE, $E_A(\theta)$, is defined as in the previous section: $E_A(\theta) = E_{\theta,\phi} - E_{0°,0°}$. Unlike Gd, the GdN compound crystallizes in the cubic rocksalt structure and its magnetic anisotropy will depend not only on θ but also on ϕ. In order to determine the easy and the hard axes of magnetization, we have calculated the MAE as a function of spherical coordinates angles θ or ϕ by keeping one of them fixed and varying the other one.

Figures 3(a,b) show the MAEs of GdN and $GdFe_2$ as a function of the spherical coordinates angles θ or ϕ. The black circles curve in figure 3(a) represents the GdN MAE versus θ for $\phi = 0°$, the red up triangles curve in the same figure represents the GdN MAE versus

ϕ for $\theta = 55°$. According to the black circle curve, the easy axis of magnetization is along the direction (001) defined by ($\theta = 0°, \phi = 0°$), and according to the red up triangles curve the hard axis of magnetization is along the direction (111) defined by ($\theta = 55°, \phi = 45°$).

The $GdFe_2$ MAE (see figure 3(b)) is found to exhibit a similar behavior to that of GdN MAE with the same axis of easy and hard magnetization, but with a higher MAE. The GdN MAE is only of 0.38 μeV while that of the $GdFe_2$ is of about 9 μeV. It is worth mentioning here that although Gd monocrystal MAE is very similar to that of a $3d$ transition metal, the MAEs of its GdN and $GdFe_2$ compounds seem to be different from that of a cubic transition metal, like Ni. It is well known that in a fcc transition metal like Ni, the (111) direction is that of the easy axis of magnetization and the hard axis is found to lie along one of the symmetry equivalent (001), (010), or the (100) directions. Our results suggest the opposite for GdN and $GdFe_2$ compounds. This peculiar behavior of the magnetic anisotropy of the Gd compounds show that even in the presence of another non-magnetic (N) or magnetic (Fe) atoms is the Gd strong magnetism which manages indirectly the magnetic anisotropy in these compounds. Indeed, because of the zero spin-orbit coupling of the $4f$ half filled shell, the $4f$ magnetic moment should not be involved directly in the MAE but only through hybridization and polarization of the other valence orbitals. One could therefore easily notice that the $4f$ strong magnetic moment is to some extent *decoupled* from the crystal structure. However, due to the strongly localized character of these orbitals, the $4f$ states carry a strong magnetic moment that polarizes strongly the remaining valence electron bands. Therefore, despite their strong localized character and zero orbital moment, their energy positions in the band structure is directly related to the strength of MAE. As it was discussed in the previous section, there is a big difference between the GGA+U MAE and the GGA or the GGA-core MAEs, i.e., one is left with a wrong magnetic anisotropy of 3 times that of the GGA+U if the $4f$ orbitals are *prevented* to hybridize correctly with the other orbitals, and one order of magnitude if they hybridize too much, like in the GGA calculation. In the case of the GdN compound not only the $5d$ Gd orbital would be affected by the $4f$ exchange magnetic field but also the $3p$ N orbitals. This happens because of the hybridization effect of the $5d$-Gd orbitals with $2p$-N orbitals [26]. For the $GdFe_2$ compound the same scenario happens to the $3d$ Fe orbitals. This interesting property would make of Gd a good candidate for high performance ferromagnets. Indeed, if we could make materials with different $4f$ energy positions in order to change the hybridization and induce large spin polarization in

other orbitals, we will be able to tune the MAE of Gd magnetic materials.

V. CONCLUSION

In conclusion, we have carried out first principles calculations of the MAE within the GGA, GGA-core and GGA+U methods for the purpose of representing accurately the $4f$ electrons of Gd. It is shown that the MAE is very sensitive to the electronic structure details at the Fermi level, i.e., the failure of the GGA method to account for the correct $4f$ energy position results in an overestimation of the Gd MAE. To the contrary, the GGA+U, which produced the best position of the $4f$ states of Gd, reproduced the best MAE of Gd. Indeed, the force-theorem MAE results of the GGA+U produced the best agreement with the experimental MAE magnitude. The results of GGA+U are also in good agreement with Bruno's model, where the MAE is obtained from the anisotropy of the orbital magnetic moments. Our calculation did not, however, find any deviation of the easy axis from the crystal c direction as shown in experiment and in the calculation of Colarieti-Tosti and coworkers [21]. Based in our GGA+U calculations, Bruno's model, and the symmetry of the hcp lattice, we did not find any good argument for the deviation of the easy axis from the hcp crystal c direction. We can only speculate that this deviation might be the results of symmetry breaking imperfections in the hcp structure.

The comparison of the GGA-core MAE and the GGA+U MAE with experiment have indirectly demonstrated that the $4f$ hybridization with the rest of the valence orbitals and the corresponding induced polarizations are key mechanisms for the tuning of the MAE of Gd or Gd based compounds. These mechanisms are tuned by the energy position of the $4f$ states in each compound. Indeed, within the GGA+U scheme we have shown that for both GdN and $GdFe_2$ compounds, the Gd $4f$ states through hybridization and induced strong polarization of, respectively, the nitrogen p and Fe $3d$ states change drastically the MAE. Unlike $3d$ transition metals fcc structure like Ni, GdN and $GdFe_2$ magnetizations are found to lie along one of the symmetry equivalent (100), (010), or (001) direction. It will be of great interest to perform experimental measurements of MAE for GdN or $GdFe_2$ to check our theoretical predictions.

Acknowledgments

The calculations were performed using the SGI Intel supercomputer, the intel HPC cluster of the Université Louis Pasteur de Strasbourg, and the IBM SP4 supercomputer of the CINES under computer Grant No. gem1100. This work is supported by an ANR grant No. ANR-06-NANO-053-01.

[1] S. S. A. Razee, J. B. Staunton, B. Ginatempo, F. J. Pinski, and E. Bruno, Phys. Rev. Lett. **82**, 5369 (1999).

[2] S. Ostanin, J. B. Staunton, S. S. A. Razee, C. Demangeat, B. Ginatempo, and E. Bruno, Phys. Rev. B **69**, 064425 (2004).

[3] S. Pascarelli, M. P. Ruffoni, A. Trapananti, O. Mathon, G. Aquilanti, S. Ostanin, J. B. Staunton, and R. F. Pettifer, Phys. Rev. Lett. **99**, 237204 (2007).

[4] I. Galanakis, M. Alouani, and H. Dreyssé, Phys. Rev. B **62**, 6475 (2000).

[5] P. Bruno, Phys. Rev. B **39**, 865 (1989).

[6] H. A. Dürr *et al.*, Scinece **277**, 213 (1997).

[7] A. B. Shick, D. L. Novikov, and A. J. Freeman, Phys. Rev. B **56**, 14259 (1997).

[8] I. Galanakis, M. Alouani, and H. Dreyssé, Phys. Rev. B **62**, 3923 (2000).

[9] H. Xi, R. M. White, S. M. Rezende, J. Appl. Phys. **87**, 4960 (2000).

[10] J. Geshev, Phys. Rev. B **62**, 5627 (2000).

[11] J. Åkerman, V. Ström, K. V. Rao, and E. D. Dahlberg, Phys. Rev. B **76**, 144416 (2007).

[12] S. Bornemann, J. Minár, J. B. Staunton, J. Honolka, A. Enders, K. Kern, and H. Ebert, Eur. Phys. J. D **45**, 529 (2007).

[13] J. Hong, Phys. Rev. B **76**, 092403 (2007).

[14] R. Wu and A. J. Freeman, J. App. Phys. **79**, 6209 (1996).

[15] K. W. Edmonds, G. van der Laan, A. A. Freeman, N. R. S. Farley, T. K. Johal, R. P. Campion, C. T. Foxon, B. L. Gallagher, and E. Arenholz, Phys. Rev. Lett. **96**, 117207 (2006).

[16] A. A. Freeman, K. W. Edmonds, G. van der Laan, R. P. Campion, A. W. Rushforth, N. R. S. Farley, T. K. Johal, C. T. Foxon, B. L. Gallagher, A. Rogalev, and F. Wilhelm, Phys. Rev. B **77**, 073304 (2008).

[17] W. Grange, I. Galanakis, M. Alouani, M. Maret, J.-P. Kappler, and A. Rogalev, Phys. Rev. B **62**, 1157 (2000).

[18] G. van der Laan, J. Phys.: Condens. Matter **10**, 3239 (1998).

[19] J. W. Cable and E. O. Wollan, Phys. Rev. **165**, 733 (1968).

[20] J. J. M. Franse and R. Gersdorf, Phys. Rev. Lett. **45**, 50 (1980).

[21] M. Colarieti-Tosti, S. I. Simak, R. Ahuja, L. Nordström, O. Eriksson, D. Aberg, S. Edvardsson, and M. S. S. Brooks, Phys. Rev. Lett. **91**, 157201 (2003).

[22] Z. P. Yin and W. E. Pickett, Phys. Rev. B **74**, 205106 (2006).

[23] B. R. Maddox, A. Lazicki, C. S. Yoo, V. Iota, A. K. McMahan, M. Y. Hu, P. Chow, R. T. Scalettar, and W. E. Pickett, Phys. Rev. Lett. **96**, 215701 (2006).

[24] A. R. Makintosh and O. K. Andersen, in *Electron at the Fermi Surface*, edited by M. Springford (Cambridge University Press, 1980).

[25] S. Abdelouahed, N. Baadji, and M. Alouani, Phys. Rev. B **75**, 094428 (2007).

[26] S. Abdelouahed and M. Alouani, Phys. Rev. B **76**, 214409 (2007).

[27] E. Wimmer, H. Krakauer, M. Weinert, and A. J. Freeman, Phys. Rev. B **24**, 864 (1981).

[28] M. Weinert, E. Wimmer, and A. J. Freeman, Phys. Rev. B **26**, 4571 (1982).

[29] http://www.flapw.de.

[30] J. R. Banister, S. Legvold, and F. H. Spedding, Phys. Rev. **94**, 1140 (1954).

[31] F. Leuenberger, A. Parge, W. Felsch, K. Fauth, and M. Hessler, Phys. Rev. B **72**, 014427 (2005).

[32] K. N. R. Taylor, Adv. Phys. **2**, 551 (1971).

[33] J. P. Perdew, K. Burke, and M. Ernzerhof, Phys. Rev. Lett. **77**, 3865 (1996).

[34] A. B. Shick, A. I. Liechtenstein, and W. E. Pickett, Phys. Rev. B **60**, 10763 (1999).

[35] To our best knowledge, the U and J are not yet determined for the $GdFe_2$ compound because of the lacking of the photoemission (XPS) and bremsstrahlung isochromat (BIS) spectra in the litterature.

[36] M. J. Gillan, J. Phys.: Condens. matter **1**, 689 (1989).

[37] G. H. O. Daalderop and P. J. Kelly and M. F. H. Schuurmans, Phys. Rev. B **41**, 11919 (1990).

[38] D.-S. Wang and R. Wu and A. J. Freeman, Phys. Rev. Lett. **70**, 869 (1993).

[39] X. Wang and R. Wu and D.-S. Wang and A. J. Freeman, Phys. Rev. B **54**, 61 (1996).

[40] J. H. Van Vleck, Phys. Rev. **52**, 1178 (1937).

[41] I. Galanakis,P. M. Oppneer, P. Ravindran, L. Nordström, P. James, M. Alouani, H. Dreyssé, and O. Eriksson, Phys. Rev. B **63**, 172405 (2001); I. Galanakis, M. Alouani, P. M. Oppneer, H. Dreyssé, and O. Eriksson, J. Phys: Condens. Matter **13**, 4553 (2001)..

Chapter 8

Conclusions and perspectives

In this work, a detailed first principles study of the strong ferromagnetic Gd material and Gd compounds were presented. The calculations were performed within the density functional theory, using the full potential linear augmented plane wave method (FLAPW) as implemented in the Fleur code.
In spite of the high Curie temperature of gadolinium (found to be of about 295° K), the importance of the electronic correlation on the stability of its magnetic state was the subject of a controversy during the last decade. Indeed, it is especially the strongly localized and correlated $4f$ electrons which confers complexity to the Gd materials and all $4f$ rare-earth magnetic materials. In order to elucidate the underlying physics of such electronic structure we have treated the $4f$ electrons according to the GGA+U scheme. Because of the growing progress of the XMCD techniques and its usefulness in characterizing magnetic materials we have implemented the calculation of the magnetic circular dichroism of the X-ray (XMCD), the corresponding sum rules, and the calculation of the magnetic dipole within the ab-initio code (Fleur) using the FLAPW method.
Due to its half filled f shell the gadolinium metal is the strongest ferromagnet of the rare earth materials class. One should, therefore, *properly* account for the peculiar strongly localized and correlated $4f$ conduction electrons. We have clearly shown that the GGA+U method is the most appropriate to describe the Gd electronic structure. The results we have obtained using the GGA+U method are found to be in good agreement with the experimental photoemission and inverse photoemission (XPS and BIS) results. Our calculated $L_{2,3}$ and $M_{4,5}$ XMCD spectra are also found in good agreement with experiment. The sum-rules spin and orbital magnetic moments calculated from the XMCD spectra are mostly close to those predicted by experiment. This agreement approves the XMCD dipolar approximation and shows the usefulness and the validity of these rules to probe the magnetic properties of the $4f$ electrons systems.
The half-metallic ferromagnets of the diluted magnetic semiconductor (DMS) class, materials which show a metallic behavior in the majority spin band and semiconducting behavior in the minority spin band, are very interesting for applications in the field of spintronics, since, due to the 100% spin polarization that they present at Fermi level, they can maximize the efficiency of spintronic devices. For this reason they are extensively studied. Surprisingly, only those based on $3d$ transition metal magnetism are concerned despite the strong $4f$ rare-earth magnetism. In this respect, we have approached the GdN compound and shown the half metallic character of its electronic structure at the experimental lattice parameter constant. We have also found that there is a considerable hybridization of the $3d$ Gd orbitals with those of the $2p$ N ones. The calculated $L_{2,3}$ XMCD spectra are found to be in agreement with the experiment indicating indirectly

that the GdN conduction bands are well described within our XMCD-FLAPW framework. The self-consistent total energy calculations have revealed the electronic and structural properties richness of GdN. Under hydrostatic pressure the rocksalt half-metal GdN becomes a wurtzite semiconductor.

Several applications in spintronic devises require anisotropic magnetic materials. The magnetic anisotropy is therefore a useful aspect for industrial magnetic applications. Due to the strong $4f$ magnetism, it is interesting to understand the magnetic anisotropy phenomena in rare-earth materials.

Within the FLAPW framework we have studied the magnetic anisotropy of Gd, GdN, and $GdFe_2$ materials. In order to simulate the magnetization rotation effect and calculate the magnetocrystalline anisotropy energy (MAE) we have performed force theorem calculations.

We have clearly shown that the $4f$ materials magnetic anisotropy stems from the band-structure spin-orbit coupling. The GGA+U MAE is found to be in best agreement with experiment compared to those obtained by means of the standard GGA and GGA-core model. Since the $4f$ sub-band structure is correctly represented by the GGA+U method, one would be left with the correct MAE. This achieved appreciable agreement of the GGA+U method with experiment compared to other methods should reflect the crucial role of the $4f$ orbitals in the magnetic anisotropy despite their too localized character.

More striking is the magnetic anisotropy of the cubic GdN and $GdFe_2$ compounds. Despite the similarity of the magnetic anisotropy of Gd to that of the $3d$ transition metal (found to be only of some μeV), the magnetic anisotropy of these cubic compounds is found to be different from that of the corresponding $3d$ cubic materials. The easy axis of magnetization for GdN and $GdFe_2$ is found to lie along the (001) direction, and that of the hard axis lies along the (111) direction. This means that it is the $4f$ magnetism which manages the magnetic anisotropy in pure rare-earth materials or rare-earth compounds even if the half filled $4f$ Gd shell has a nil spin-orbit coupling.

Though the good agreement of our Gd $M_{4,5}$ XMCD spectra with experiment, the experimental small structures appearing above and below the principal dipolar peak were not reproduced. These structures are ascribed to dynamical processes involved during the experimental probe, i.e., core-hole interaction or multiplet effect and can not be accounted for within a time-independent DFT scheme. The dynamical mean-field theory (DMFT) is believed to be a major step towards the reunion of two theoretical approaches, i.e., the DFT and many-body model Hamiltonian of condensed matter physics. This method should allow a reasonable understanding of the dynamical aspect of the XMCD. It is planed to implement the XMCD calculations within this methods to *follow* the time evolution of the electron-hole interaction during x-ray absorption.

Another interesting aspect of the magnetism is that of the non-collinearity. This phenomena, which is a direct consequence of the competition between the spin-orbit coupling and the exchange interactions, may take place under doping or hydrostatic pressure. Indeed, this appears as a change of the magnetic configuration and therefore of the Curie temperature. Understanding such phenomena and calculating the Curie temperature is of great interest. As a continuation of this work, we plane to study of the doping of GdN with hydrogen or manganese to raise its Curie temperature. Having shown the validity of the force theorem for the calculation of the $4f$ systems magnetic anisotropy within the GGA+U method, and given the fact that the majority of the non-colinear implementations are based on the force theorem, we expect a fruitful investigations of the Curie temperature of GdN.

Appendix A

Tetrahedron Fermi-surface integration

This part is aimed at calculating the Fermi-surface areas for different cases. Let as follow the same enumeration used in section (4.4.4). Assuming that the band structure energies are linear in $\mathbf{k}$ points [133], one can straightforwardly calculate the interpolated wave-vector $\mathbf{k}_F$ and, therefore the corresponding Fermi surface.

1. If $\varepsilon_1 < \varepsilon_F < \varepsilon_2 < \varepsilon_3 < \varepsilon_4$, the wave-vector $\mathbf{k}_F$ can be calculated as:

$$\mathbf{k}_{F1} = \mathbf{k}_2 + \frac{(\varepsilon_F - \varepsilon_1)}{(\varepsilon_2 - \varepsilon_1)}(\mathbf{k}_2 - \mathbf{k}_1), \tag{A.1}$$

$$\mathbf{k}_{F2} = \mathbf{k}_3 + \frac{(\varepsilon_F - \varepsilon_1)}{(\varepsilon_3 - \varepsilon_1)}(\mathbf{k}_3 - \mathbf{k}_1), \tag{A.2}$$

$$\mathbf{k}_{F3} = \mathbf{k}_4 + \frac{(\varepsilon_F - \varepsilon_1)}{(\varepsilon_4 - \varepsilon_1)}(\mathbf{k}_4 - \mathbf{k}_1), \tag{A.3}$$

   these three wave-vectors are those forming the corner 1 marked by (k_1,e_1) in figure (4.3). The Fermi surface area which crosses this corner is therefore

$$\mathbf{S}_1 = \frac{1}{2}(\mathbf{K}_1 \times \mathbf{K}_2), \tag{A.4}$$

   where $\mathbf{K}_1$ and $\mathbf{K}_2$ are the reciprocal vectors:

$$\mathbf{K}_1 = \mathbf{k}_{F2} - \mathbf{k}_{F1}, \mathbf{K}_2 = \mathbf{k}_{F3} - \mathbf{k}_{F1}. \tag{A.5}$$

2. If $\varepsilon_1 < \varepsilon_2 < \varepsilon_3 < \varepsilon_F < \varepsilon_4$, with the same manner, the wave-vector $\mathbf{k}_F$ is calculated as:

$$\mathbf{k}_{F1} = \mathbf{k}_2 + \frac{(\varepsilon_F - \varepsilon_4)}{(\varepsilon_3 - \varepsilon_4)}(\mathbf{k}_3 - \mathbf{k}_4), \tag{A.6}$$

$$\mathbf{k}_{F2} = \mathbf{k}_3 + \frac{(\varepsilon_F - \varepsilon_4)}{(\varepsilon_2 - \varepsilon_4)}(\mathbf{k}_2 - \mathbf{k}_4), \tag{A.7}$$

$$\mathbf{k}_{F3} = \mathbf{k}_4 + \frac{(\varepsilon_F - \varepsilon_4)}{(\varepsilon_1 - \varepsilon_4)}(\mathbf{k}_1 - \mathbf{k}_4), \tag{A.8}$$

   these three wave-vectors are those forming the corner 4 marked by (k_4,e_4) in figure (4.3). The corresponding Fermi surface is calculated as in (A.4) and (A.5).

3. If $\varepsilon_1 < \varepsilon_2 < \varepsilon_F < \varepsilon_3 < \varepsilon_4$, we will have two contributions $\mathbf{S}_3$ and $\mathbf{S}_4$. The calculation of these surfaces is too similar to that of the previous ones.

The surfaces $\mathbf{S}_1$, $\mathbf{S}_2$, $\mathbf{S}_3$, and $\mathbf{S}_4$ are the hatched areas of figure (4.3).

Appendix B

The spin-orbit coupling angular matrix derivation

In this appendix we would like to derive the angular part of the spin-orbit coupling $\mathbf{L}.\boldsymbol{\sigma}$. In order to account for the appropriate geometry of this spin-orbit operator we shall remind the reader that the quantization axis is conventionally the z-axis. Therefore, one should *rotate*[1] the SOC operator toward the z-axis to get insight onto the involved z-components of the spin orbital and magnetic moments. The rotation operation of the SOC is given by:

$$[\mathbf{L}.\boldsymbol{\sigma}]_z = R(\mathbf{L}.\boldsymbol{\sigma})R^{+}, \tag{B.1}$$

where R is the rotation matrix operator [134]:

$$R = \begin{pmatrix} cos(\frac{\theta}{2})e^{-i\frac{\phi}{2}} & sin(\frac{\theta}{2})e^{i\frac{\phi}{2}} \\ -sin(\frac{\theta}{2})e^{-i\frac{\phi}{2}} & cos(\frac{\theta}{2})e^{i\frac{\phi}{2}} \end{pmatrix}, \tag{B.2}$$

where θ and ϕ are the polar angles. Writing the spin operator $\boldsymbol{\sigma}$ in terms of the Pauli matrices σ_x, σ_y, and σ_z

$$\sigma_x = \begin{pmatrix} 0 & 1 \\ 1 & 0 \end{pmatrix}, \sigma_y = \begin{pmatrix} 0 & -i \\ i & 0 \end{pmatrix}, \sigma_z = \begin{pmatrix} 1 & 0 \\ 0 & -1 \end{pmatrix}, \tag{B.3}$$

the spin-orbit operator takes the form

$$\mathbf{L}.\boldsymbol{\sigma} = \begin{pmatrix} l_z & l^{-} \\ l^{+} & -l_z \end{pmatrix}, \tag{B.4}$$

where l^{-} and l^{+} are the angular momentum operator defined as

$$l^{-} = l_x - il_y, l^{+} = l_x + il_y. \tag{B.5}$$

Substituting equations (B.4) and (B.2) into equation (B.1) leads to

$$[\mathbf{L}.\boldsymbol{\sigma}]_z = \begin{pmatrix} \left[cos(\theta)l_z + \frac{1}{2}sin(\theta)(e^{-i\phi}l^{-} + e^{i\phi}l^{+})\right] & \left[cos^2(\frac{\theta}{2})e^{-i\phi}l^{-} - sin^2(\frac{\theta}{2})e^{i\phi}l^{+} - sin(\theta)l_z\right] \\ \left[-sin^2(\frac{\theta}{2})e^{-i\phi}l^{-} + cos^2(\frac{\theta}{2})e^{i\phi}l^{+} - sin(\theta)l_z\right] & -\left[cos(\theta)l_z + \frac{1}{2}sin(\theta)(e^{-i\phi}l^{-} + e^{i\phi}l^{+})\right] \end{pmatrix}. \tag{B.6}$$

This is the formula we have adopted during our XMCD and magnetic anisotropy investigations.

[1] Rotating the SOC operator from the local frame to the global frame is equivalent to rotating the system of reference from the global frame to the local frame.

Appendix C

The magnetic dipole calculation within the FLAPW method

This part is devoted to the derivation of the T_z magnetic dipole within the FLAPW method. As it is implemented by Baadji *et al.* (see paper I) within the Fleur code [25]. The magnetic dipole operator is given by:

$$T_z = \frac{1}{2}\left[\boldsymbol{\sigma} - 3\hat{\mathbf{r}}(\hat{\mathbf{r}}.\boldsymbol{\sigma})\right]_z . \tag{C.1}$$

Using the Pauli matrices (equation (B.3)) of the previous appendix the T_z operator can be written as:

$$T_z = \begin{pmatrix} 1-3cos^2(\theta) & -3cos(\theta)sin(\theta)e^{-i\phi} \\ -3cos(\theta)sin(\theta)e^{i\phi} & -1+3cos^2(\theta) \end{pmatrix} = \sqrt{\frac{2\pi}{5}} \begin{pmatrix} \sqrt{2}Y_{2,0} & -\sqrt{3}Y_{2,-1} \\ \sqrt{3}Y_{2,1} & -\sqrt{2}Y_{2,0} \end{pmatrix}, \tag{C.2}$$

if the magnetization is parallel to the z-axis the magnetic dipole operator takes the form

$$T_z = \sqrt{\frac{4\pi}{5}} \begin{pmatrix} Y_{2,0} & 0 \\ 0 & -Y_{2,0} \end{pmatrix}, \tag{C.3}$$

where $Y_{l,m}$ are the spherical harmonics.
In order to calculate the T_z expectation value

$$\langle T_z \rangle = \langle \phi_\nu(\mathbf{k},\mathbf{r}) \left| T_z \right| \phi_{\nu'}(\mathbf{k},\mathbf{r}) \rangle , \tag{C.4}$$

inside the muffin-tin spheres, one needs the corresponding FLAPW wave function (equation (4.55)):

$$\psi_\nu^\sigma(\mathbf{k},\mathbf{r}) = \sum_{lm} (A_{lm}^{\mu,\sigma}(\mathbf{k}) u_l^\sigma(|\mathbf{r}-\mathbf{R}_\mu|) + B_{lm}^{\mu,\sigma}(\mathbf{k}) \dot{u}_l{}^\sigma(|\mathbf{r}-\mathbf{R}_\mu|)) Y_{lm}(\widehat{\mathbf{r}-\mathbf{R}_\mu}). \tag{C.5}$$

For simplicity we consider the case of one atom per cell. The expectation value of the T_z operator is finally calculated as:

$$\begin{aligned} \langle T_z \rangle = \frac{1}{V_{BZ}} \int \sum_{lm,l'm'} \big(& A_{lm}^{*\mu,\sigma}(\mathbf{k}) A_{l'm'}^{\mu,\sigma}(\mathbf{k}) C_{lm,l'm'}^{1,\sigma} + B_{lm}^{*\mu,\sigma}(\mathbf{k}) A_{l'm'}^{\mu,\sigma}(\mathbf{k}) C_{lm,l'm'}^{2,\sigma} \\ & + A_{lm}^{*\mu,\sigma}(\mathbf{k}) B_{l'm'}^{\mu,\sigma}(\mathbf{k}) C_{lm,l'm'}^{3,\sigma} + B_{lm}^{*\mu,\sigma}(\mathbf{k}) B_{l'm'}^{\mu,\sigma}(\mathbf{k}) C_{lm,l'm'}^{4,\sigma} \big)\, d^3k, \end{aligned} \tag{C.6}$$

where

$$C^{1,\sigma}_{lm,l'm'} = \sigma G^{m,2,m'}_{l,2,l'} \int r^2 dr u^{\sigma}_{l}(r) u^{\sigma}_{l'}(r), \tag{C.7}$$

$$C^{2,\sigma}_{lm,l'm'} = \sigma G^{m,2,m'}_{l,2,l'} \int r^2 dr u^{\sigma}_{l}(r) \dot{u}^{\sigma}_{l'}(r), \tag{C.8}$$

$$C^{3,\sigma}_{lm,l'm'} = \sigma G^{m,2,m'}_{l,2,l'} \int r^2 dr \dot{u}^{\sigma}_{l}(r) u^{\sigma}_{l'}(r), \tag{C.9}$$

$$C^{4,\sigma}_{lm,l'm'} = \sigma G^{m,2,m'}_{l,2,l'} \int r^2 dr \dot{u}^{\sigma}_{l}(r) \dot{u}^{\sigma}_{l'}(r), \tag{C.10}$$

where the integration is that of the Brillouin zone (section (4.4.4)) and $G^{m,2,m'}_{l,2,l'}$ is the Gaunt coefficient.

Bibliography

[1] J. P. Perdew and M. Levy, Phys. Rev. Lett. **51**, 1884 (1983).

[2] C. Amador, W. R. L. Lambrecht, and B. Segall, Phys. Rev. B **46**, 1870 (1992).

[3] J. Hubbard, Proc. R. Soc. London **276**, 238 (1963).

[4] J. Hubbard, Proc. R. Soc. London **277** (1964).

[5] J. Hubbard, Proc. R. Soc. London **281**, 401 (1964).

[6] J. Hubbard, Proc. R. Soc. London **285**, 442 (1965).

[7] A. B. Shick, A. I. Liechtenstein, and W. E. Pickett, Phys. Rev. B **60**, 10763 (1999).

[8] Z. Szotek, W. M. Temmerman, and H. Winter, Phys. Rev. B **47**, 4029 (1993).

[9] V. I. Anisomov, I. V. Solovyev, M. A. Korotin, M. T. Czyzyk, and G. A. Sawatzky, Phys. Rev. B **48**, 16929 (1993).

[10] O. Bengone, M. Alouani, P. Blöchl, and J. Hugel, Phys. Rev. B **62**, 16392 (2000).

[11] A. G. Petukhov, I. I. Mazin, L. Chioncel, and A. I. Lichtenstein, Phys. Rev. B **67**, 153106 (2003).

[12] J. P. Perdew and A. Zunger, Phys. Rev. B **23**, 5048 (1981).

[13] E. C. Stoner, Proc. R. Soc. London A **154**, 565 (1936).

[14] D. J. Singh, *Planewaves, Pseudopotentials and the LAPW Method* (Kluwer Academic Publishers, Boston/Dordrecht/LONDON, 1994).

[15] B. Kim, A. B. Andrews, J. L. Erskine, K. J. Kim, and B. N. Harmon, Phys. Rev. Lett. **68**, 1931 (1992).

[16] D. Li, J. Pearson, S. D. Bader, D. N. Mcllory, C. Waldfried, and P. A. Dowben, Phys. Rev. B **51**, 13895 (1995).

[17] K. Maiti, M. C. Malagoli, A. Dallmeyer, and C. Carbone, Phys. Rev. Lett. **88**, 167205 (2002).

[18] D. R. Hamann, Phys. Rev. Lett. **42**, 662 (1979).

[19] E. Wimmer, H. Krakauer, M. Weinert, and A. J. Freeman, Phys. Rev. B **24**, 864 (1981).

[20] C.-G. Duan, R. F. Sabirianov, W. N. Mei, P. A. Dowben, S. S. Jaswal, and E. Y. Tsymbal, J. Phys.: Condens Matter **19**, 315220 (2007).

[21] S. A. Wolf, D. D. Awschalom, R. A. Buhrman, J. M. Daughton, S. von Molnar, M. L. Roukes, A. Y. Chtchelkanova, and D. M. Treger, Science **294**, 1488 (2001).

[22] J. O. de Dimmock and A. J. Freeman, Phys. Rev. Lett. **13**, 750 (1964).

[23] J. Sticht and J. Kübler, Solid State Commun. **53**, 529 (1985).

[24] W. Temmerman and P. A. Sterne, J. Phys.: Condens Matter **2**, 5529 (1990).

[25] See http://www.fleur.de.

[26] B. Thole, P. Carra, F. Sette, and G. van der Laan, Phys. Rev. Lett. **68**, 1943 (1992).

[27] P. Carra, B. Thole, M. Altarelli, and X. Wang, Phys. Rev. Lett. **70**, 694 (1993).

[28] M. Born and J. R. Oppenheimer, Ann. Phys. **87**, 457 (1927).

[29] D. R. Hartree, Proc. Cambridge Phyl. Soc. **24**, 89 (1928).

[30] V.Fock, Z. Phys. **61**, 126 (1930).

[31] V.Fock, Z. Phys. **62**, 795 (1930).

[32] L. H. Thomas, Proc. Cambridge Phyl. Soc. **23**, 542 (1927).

[33] E. Fermi, Rend. Naz.Linzei **6**, 602 (1927).

[34] J. C. Slater, *The Self-Consistent Field of Molecules and solids*, vol. 4 (McGraw-Hill, New-York, 1974).

[35] P. Hohenberg and W. Kohn, Phys. Rev. **136**, 864 (1964).

[36] W. Kohn and L. J. Sham, Phys. Rev. **140**, 1133 (1965).

[37] D. M. Ceperly and B. J. Alder, Phys. Rev. Lett. **45**, 566 (1980).

[38] U. von Barth and L. Hedin, J. Phys. C **5**, 1629 (1972).

[39] V. L. Moruzzi, J. F. Janak, and A. R. Williams, *Calculated Electronic Properties of Metals* (PERGAMON, New-York, 1978).

[40] Y. Wang and J. P. Perdew, Phys. Rev. B **44**, 13298 (1991).

[41] J. P. Perdew, K. Burke, and M. Ernzerhof, Phys. Rev. B **77**, 3865 (1996).

[42] J. P. Perdew, K. Burke, and Y. Wang, Phys. Rev. B **54**, 16533 (1996).

[43] O. Gunnarsson and B. I. Lundqvist, Phys. Rev. B **13**, 4274 (1976).

[44] V. Anisimov, F. Aryasetiawan, and A. I. Lichtenstein, J. Phys.: Condens Matter **9**, 767 (1997).

[45] A. I. Liechtenstein, V. I. Anisomov, and J. Zaanen, Phys. Rev. B **52**, 5467 (1995).

[46] B. N. Harmon, V. P. Antropov, A. I. Liechtenstein, I. V. Solovyev, and V. I. Anisomov, J. Phys. Chem. Solids **56**, 1521 (1995).

[47] A. I. Liechtenstein, V. I. Anisomov, and J. Zaanen, Phys. Rev. B **52**, 5467 (1995).

[48] V. Anisomov and O. Gunnarsson, Phys. Rev. B **43**, 5770 (1991).

[49] J. C. Slater, Phys. Rev. **51**, 846 (1937).

[50] J. C. Slater, Phys. Rev. **92**, 603 (1953).

[51] M. M. Saffren and J. C. Slater, Phys. Rev. **92**, 1126 (1953).

[52] J. Korringa, Physica **13**, 392 (1947).

[53] W. Kohn and N. Rostoker, Phys. Rev. **94**, 1111 (1954).

[54] J. callaway, *Energy Band Theory* (Academic Press, New-York, 1964).

[55] J. C. Slater and G. F. Koster, Phys. Rev. **94**, 1498 (1954).

[56] J. H. Terrell, Phys. Rev. Lett. **8**, 149 (1964).

[57] O. K. Andersen, Phys. Rev. B **12**, 3060 (1975).

[58] T. L. Loucks, *Augmented Plane Wave Method* (Benjamin, New-York, 1967).

[59] D. Singh, Phys. Rev. B **43**, 6388 (1991).

[60] P. K. de Boer and R. A. de Groot, J. Phys.: Condens Matter **10**, 10241 (1998).

[61] M. Weinert, J. Math. Phys. **22**, 2433 (1981).

[62] P. Kurz, *Non-Collinear magnetism of Ultrathin Magnetic Films* (Institut für Festkörperforschung, 1997).

[63] D. J. Chadi and M. L. Cohen, Phys. Rev. B **12**, 5747 (1973).

[64] P. E. Blöchl, O. Jepsen, and O. K. Andersen, Phys. Rev. B **49**, 16223 (1994).

[65] J. D. Jackson, *Classical electrodynamics* (Wiley, New York, 1975).

[66] M. Brooks and D. Goodings, J. Phys. C **5**, 1279 (1968).

[67] J. Jenson and A. Mackintosh, *Rare Earth Magnetism* (Oxford University Press, Oxford, 1991).

[68] J. H. van Vleck, Phys. Rev. **52**, 1178 (1937).

[69] A. B. Shick, V. Drchal, J. Kudrnovský, and P. Weinberger, Phys. Rev. B **54**, 1610 (1996).

[70] A. R. Makintosh and O. K. Andersen, in *Electron at the Fermi Surface*, edited by M. Springford (Cambridge University Press, 1980).

[71] D. Koelling and B. Harmon, J. Phys. C **10**, 3107 (1977).

[72] E. M. Rose, *Relativistic Electron Theory* (Wiley, New York, 1961).

[73] R. Wu and A. J. Freeman, J. App. Phys. **79**, 6209 (1996).

[74] S. Ostanin, J. B. Staunton, S. S. A. Razee, C. Demangeat, B. Ginatempo, and E. Bruno, Phys. Rev. B **69**, O64425 (2004).

[75] P. Bruno, Phys. Rev. B **39**, 865 (1989).

[76] A. B. Shick, D. L. Novikov, and A. J. Freeman, Phys. Rev. B **56**, 14259 (1997).

[77] G. van der Laan, J. Phys.: Condens Matter **10**, 3239 (1998).

[78] G. H. O. Daalderop, P. J. Kelly, and M. F. H. Schuurmans, Phys. Rev. B **41**, 11919 (1990).

[79] D.-S. Wang, R. Wu, and A. J. Freeman, Phys. Rev. Lett. **70**, 869 (1993).

[80] X. Wang, R. Wu, D.-S. Wang, and A. J. Freeman, Phys. Rev. B **54**, 61 (1996).

[81] A. Hubert, W. Unger, and J. Kranz, Z. Phys. **148**, 1969 (224).

[82] P. Escudier, Ann. Phys. **9**, 125 (1975).

[83] H. L. Skriver, Phys. Rev. B **31**, 1909 (1985).

[84] A. I. Lichtenstein, M. I. Katsnelson, V. P. Antropov, and V. A. Gubanov, J. Magn. Magn. Mater. **67**, 65 (1987).

[85] O. L. Bacq, O. Eriksson, B. Johansson, P. James, and A. Delin, Phys. Rev. B **65**, 134430 (2002).

[86] J. J. M. Franse and R. Gersdorf, Phys. Rev. Lett. **45**, 50 (1980).

[87] M. Colarieti-Tosti, S. I. Simak, R. Ahuja, L. Nordström, O. Eriksson, D. Aberg, S. Edvardsson, and M. S. S. Brooks, Phys. Rev. Lett. **91**, 157201 (2003).

[88] M. Colarieti-Tosti, T. Burkert, O. Eriksson, L. Nordström, and M. S. S. Brooks, Phys. Rev. B **72**, 094423 (2005).

[89] W. Röntgen, Physik. Med. Ges. **137**, 132 (1895).

[90] E. Basseler, nachgewiesen mittels Sekundärstrahlung: Annalen der Phydik **28**, 808 (1909).

[91] J. Chapman, Phil. Mag. **25**, 792 (1913).

[92] J. Becker, Phys. Rev. **20**, 134 (1922).

[93] W. Kartschagin and E. Tschetwerikova, für Physik **39**, 886 (1926).

[94] D. Froman, Phys. Rev. **41**, 693 (1932).

[95] C. Kurylenko, J. Phys. Rad. **1**, 133 (1940).

[96] D. Coster, Book Reviews **3**, 160 (1948).

[97] J. Hrdý, E. Krouský, and O. Renner, Phy. Stat. Sol. (a). **53**, 143 (1979).

[98] G. Schütz, E. Zech, E. Hagn, and P. Kienle, Hyperfine Interaction **16**, 1039 (1983).

[99] E. Keller and E. Stern, in *Proc. of the EXAFS and Near Edge Structure III Conference*, edited by K. Hodgson, B. Hedman, and J. Penner-Hahn (1984), p. 507.

[100] G. Shütz, W. Wagner, W. Wilhelm, P. Kienle, R. Zeller, R. Frahm, and G. Materlik, Phys. Rev. Lett. **58**, 737 (1987).

[101] G. Shütz, R. Frahm, P. Mautner, R. Wienke, W. Wagner, W. Wilhelm, and P. Kienle, Phys. Rev. Lett. **62**, 2620 (1989).

[102] A. Rogalev, F. Wilhelm, N. Jaouen, J. Goulon, and J.-P. Kappler, in *Magnetism: A Synchrotron Radiation Approach*, edited by E. Beaurepaire, H. Bulou, F. Scheurer, and J.-P. Kappler (Springer, 2006), chap. 4, pp. 71–89.

[103] J. Erskine and E. Stern, Phys. Rev. B **12**, 5016 (1975).

[104] B. T. Thole, G. van der Laan, and G. A. Sawatzky, Phys. Rev. Lett. **55**, 2086 (1985).

[105] R. D. Cowan, J. Opt. Soc. Am. **58**, 808 (1968).

[106] B. Thole, G. van der Laan, J. C. Fuggle, G. Sawatzky, R. Karnatak, and J.-M. Esteva, Phys. Rev. B **32**, 5107 (1985).

[107] C. T. Chen, F. Sette, Y. Ma, and S. Modesti, Phys. Rev. B **42**, 7262 (1990).

[108] C. T. Chen, N. V. Smith, and F. Sette, Phys. Rev. B **43**, 6785 (1991).

[109] N. V. Smith, T. C. Chen, F. Sette, and L. F. Mattheiss, Phys. Rev. B **46**, 1023 (1992).

[110] M. Faraday, Phil. Trans. R. Soc. **136**, 1 (1846).

[111] J. Kerr, Philos. Mag. **3**, 321 (1877).

[112] H. R. Hulme, Proc R. Soc. (London) Ser. A **135**, 237 (1932).

[113] J. D. Jackson, *Classical Electrodynamics* (J. Willey, New York, 1975).

[114] N. Bloembergen, *Nonlinear Optics* (Benjamin, New York, 1965).

[115] W. H. Kleiner, Phys. Rev. **142**, 318 (1966).

[116] A. K. Zvezdin and V. A. Kotov, *Modern Magnetooptics and Magnetooptical Materials* (Institute of Physics Publishing, Bristol and Philadelphia, 1997).

[117] W. Reim and J. Schoenes, in *Ferromagnetic Materials*, edited by E. P. Wohlfarth and K. H. J. Buschow (Springer, 1990), vol. 5, p. 133.

[118] A. Yaresko, A. Perlov, V. Antonov, and B. Harmon, in *Magnetism: A Synchrotron Radiation Approach*, edited by E. Beaurepaire, H. Bulou, F. Scheurer, and J.-P. Kappler (Springer, 2006), chap. 6, pp. 121–141.

[119] J. Callaway, *Quantum Theory of the Solid State* (Academic, New York, 1974).

[120] C. S. Wang and J. Callaway, Phys. Rev. B **9**, 4897 (1974).

[121] H. S. Bennett and E. A. Stern, Phys. Rev. **137**, A448 (1965).

[122] H. Ebert, Rep. Prog. Phys. **59**, 1665 (1996).

[123] V. Antonov, B. Harmon, and A. Yaresko, *Electronic structure and magneto-optical properties of solids* (Kluwer Academic Publishers, Dordrecht, Boston, London, 2004).

[124] E. Arola, P. Strange, and B. Gyorffy, Phys. Rev. B **55**, 472 (1997).

[125] C. Cohen-Tannoudji, B. Diu, and F. Laloë, *Mécanique quantique* (Hermann, Paris, 1996), vol. I, chap. VI, pp. 689,690.

[126] H. Ebert, in *Spin-Orbit-Influenced Spectroscopies of Magnetic Solids*, edited by H. Ebert and G. Schütz (Springer, 1995), chap. 9, pp. 159–177.

[127] R. Wu, D. Wang, and A. J. Freeman, Phys. Rev. Lett. **71**, 3581 (1993).

[128] C. T. Chen, Y. U. Idzerda, H.-J. Lin, N. V. Smith, G. Meigs, E. Chaban, G. H. Ho, E. Pellegrin, and F. Sette, Phys. Rev. Lett. **75**, 152 (1995).

[129] I. Galanakis, S. Ostanin, M. Alouani, H. Dreyssé, and J. M. Wills, Phys. Rev. B **61**, 4093 (2000).

[130] J. Vogel, A. Fontaine, V. Cros, F. Petroff, J.-P. Kappler, G. Krill, A. Rogalev, and J. Goulon, Phys. Rev. B **55**, 3663 (1997).

[131] W. Grange, M. Maret, J.-P. Kappler, J. Vogel, A. Fontaine, F. Petroff, G. Krill, A. Rogalev, J. Goulon, M. Finazzi, et al., Phys. Rev. B **58**, 6289 (1998).

[132] F. Leuenberger, A. Parge, W. Felsch, F. Baudelet, C. Giorgetti, E. Dartyge, and F. Wilhelm, Phys. Rev. B **73**, 214430 (2006).

[133] G. Lehmann and M. Taut, Phys. Status Solidi B **54**, 469 (1972).

[134] C. Cohen-Tannoudji, B. Diu, and F. Laloë, *Mécanique quantique* (Hermann, Paris, 1996), vol. I, chap. IV, complément B, pp. 418–422.